System Test Measurements with a DC-DC Conversion Powering Scheme for the CMS Tracker at SLHC

von

Jan Sammet

Diplomarbeit in Physik

vorgelegt der
Fakultät für Mathematik, Informatik und
Naturwissenschaften der Rheinisch-Westfälischen
Technischen Hochschule Aachen

im Oktober 2008

angefertigt im
I. Physikalischen Institut B der RWTH Aachen

Prof. Dr. Lutz Feld

Abstract

A potential luminosity upgrade of the LHC, the so-called SLHC implies challenging upgrades for the experiments at the LHC. Concerning the upgrade of the CMS silicon strip tracker, the delivery of power is considered to be one of the major challenges. The higher instantaneous luminosity makes an increase in granularity and complexity of the device inevitable. Both are expected to result in a power consumption comparable or even higher than the power consumption of today's strip tracker. However, the space available for cables will remain the same. In addition, a further increase of the tracker material budget due to cables and cooling is considered unacceptable, as the performance of the CMS detector must not be compromised for the upgrade. Novel powering schemes such as serial powering or the usage of DC-DC converters have been proposed to solve the problem. To test the second option, substructures of the current CMS silicon strip tracker have been operated for the first time with off-the-shelf DC-DC buck converters. This thesis describes the tests and discusses the results.

Contents

Chapter 1

Introduction

The Standard Model of particle physics has proven its correctness in many tests and through confirmation of many predictions. Still it raises numerous questions which could not be answered yet due to the high energies required to observe the related processes. Therefore a new particle accelerator has been built at the European Organisation for Nuclear Research (CERN), the Large Hadron Collider (LHC). This enormous machine has a circumference of about 27 km and is located close to Geneva, approximately 100 m beneath the ground at the border between Switzerland and France. It is intended to collide protons with a centre-of-mass energy of 14 TeV, seven times larger than the highest energy achieved by an accelerator so far. At the same time a high luminosity of $10^{34}\mathrm{cm}^{-2}\mathrm{s}^{-1}$ shall allow to identify even extremely rare processes.

The main physics goal of the LHC is the discovery of the Higgs boson, which is anticipated by the Standard Model. Due to a theoretical upper limit for the Higgs mass of about 1 TeV the LHC will either find the Higgs boson or prove its non-existence. Furthermore the LHC allows the search for new physics, such as Supersymmetry and Extra Dimensions. In addition, a better understanding of Standard Model phenomena such as the Charge-Parity violation will be obtained.

Even though the LHC is already an impressive machine, it is planed to improve its capabilities even further. A possible upgrade, the Super Large Hadron Collider (SLHC), forsees to increase the LHC's luminosity by a factor of about 10. This step would push the physics potential of the LHC to a new level. This, however implies demanding R&D work for the crews of the experiments and the accelerator. Due to the complexity of the related systems significant time is required to master the associated challenges.

One of the experiments at the LHC is the Compact Muon Solenoid (CMS), a multi purpose detector which covers almost all aspects of the physics accessible by the accelerator. An important subdetector of CMS is its silicon tracking system, which allows to measure the trajectories and momenta of charged particles. Furthermore it is used to reconstruct the precise proton-proton interaction point and the vertices of decays of long-lived particles.

With regard to an upgrade of the CMS silicon tracker for the SLHC, the delivery of power is considered to be one of the major challenges. Due to the increased luminosity of the SLHC the present CMS tracker will have to be replaced by a new design which must feature an improved radiation hardness and a finer granularity. Even though the power consumption per channel is hoped to be reduced, the total power consumption of the tracker will rather increase than decrease. In addition, the reduction of the power required per channel will be linked to lower supply voltages which for the same power lead to larger currents and thus to larger ohmic losses in cables. Adding more cables is no option since already the present services occupy the available space completely. In addition, more material would spoil the tracker's physics performance and prevent CMS from exploiting the full benefits of the SLHC. Therefore two novel powering schemes have been proposed: Serial Powering (SP) and powering with DC-DC converters. While in SP a number of modules are connected in series to a constant current source, DC-DC converters are used to convert a high DC input voltage to a lower DC output voltage. The major challenges concerning DC-DC conversion are the development of a radiation hard converter and a powering scheme with an acceptable and robust noise performance. So far, a radiation hard device is not available.

For the system tests presented in this work, a subsystem of the CMS silicon strip tracker has been operated with different commercial DC-DC converters. The intention was to gain experience with such devices and to learn how they affect the present system. On a midterm scale this shall allow to evaluate the feasibility of a

converter based powering concept and help to find the optimal scheme for the tracker. As soon as radiation hard devices are available, the acquired know-how and the set-up should allow to provide the developers with a fast feedback.

Chapter 2 gives an overview of the LHC and the CMS experiment and presents an extract of their specifications.

Chapter 3 describes the tracking system of CMS with an emphasis on the strip tracker and its end caps. In addition the working principle of silicon sensors is explained.

Chapter 4 is dedicated to the SLHC and how it will affect the CMS detector and its physics potential.

In Chapter 5 novel powering schemes based on DC-DC conversion and serial powering are introduced. Different converter types and their potential integration into the CMS strip tracker system are discussed.

Chapter 6 describes the set-up that was used for the tests to be presented here. In addition, the integration of the commercial converters into the CMS system is explained and the software used for data acquisition and analysis is introduced.

Chapter 7 presents the system test measurements performed with commercial DC-DC converters and discusses the results.

Chapter 2

The Compact Muon Solenoid Experiment at the LHC

2.1 The Large Hadron Collider

In 2008, the LHC (Fig. 2.1) has been put into operation. This storage ring, located close to Geneva, Switzerland, consists of two independent beam pipes, each with a circumference of 26.7 km. The LHC was designed to collide protons with a centre-of-mass energy of 14 TeV. This energy is reached with the help of a pre-accelerator complex, shown in Fig. 2.2. The main machines of this complex are the Proton Synchrotron Booster (PSB), followed by the Proton Synchrotron (PS) and the Super Proton Synchrotron (SPS). The latter injects the protons with an energy of 450 GeV into the LHC.

Four large experiments, ATLAS[1] , ALICE[2], CMS and LHC-b[3] will observe the collisions. In addition, two smaller experiments, LHCf[4] and TOTEM[5], share the interaction points with ATLAS and CMS, respectively.

The main purpose of the LHC-b experiment is to study CP violation in B meson decays. The heavy ion experiment ALICE searches among other things for the evidence of a new phase of matter, the quark gluon plasma. The two multipurpose detectors, ATLAS and CMS, are supposed to mutually confirm their results. They are both intended to improve measurements of Standard Model parameters. Their primary task however, will be the search for the Higgs boson and new physics, like Supersymmetry or Extra Dimensions. On average, the instantaneous design luminosity of ATLAS and CMS will be $10^{34}\,\mathrm{cm}^{-2}\,\mathrm{s}^{-1}$ and lead to 20 simultaneous proton-proton interactions every 25 ns.

2.2 The CMS Detector

Figure 2.3 shows the CMS detector [3], a 21.6 m long, cylindrical multipurpose detector with a diametre of 14.6 m. It is surrounded by muon chambers which are embedded into the iron return yoke. This yoke returns the magnetic field lines generated by a superconducting solenoid. In the centre of the detector the field is homogeneous and equals 3.8 T. It allows the silicon-based tracking system, consiting of a pixel and a strip detector, to measure the trajectories and momenta of charged particles. The tracker also provides the reconstruction of the precise proton-proton interaction point, as well as the vertices of decays of long-lived particles. The CMS detector is completed by an electromagnetic and a hadronic calorimeter, which occupy the space between tracker and solenoid. Their purpose is to measure the energies of electrons/photons and hadrons, respectively. The different detector layers of CMS and their interaction with different types of particles can be seen in Fig. 2.4.

Positions within the CMS detector are described by a right-handed coordinate system. In this system the x-axis points towards the centre of the LHC ring, the y-axis points upwards and the z-axis points along the beam axis towards the Jura Mountains. Accordingly the azimuthal angle ϕ is measured from the x-axis in the $x-y$ plane. The radial coordinate in this plane is denoted by r and the polar angle θ is measured from the z-axis. The pseudorapidity is defined as $\eta = -\ln\tan(\theta/2)$.

[1] A Toroidal LHC ApparatuS
[2] A Large Ion Collider Experiment - The focus of ALICE will be on heavy-ions, which will also be accelerated by the LHC.
[3] LHC-beauty
[4] LHC forward
[5] Total Cross Section, Elastic Scattering and Diffraction Dissociation

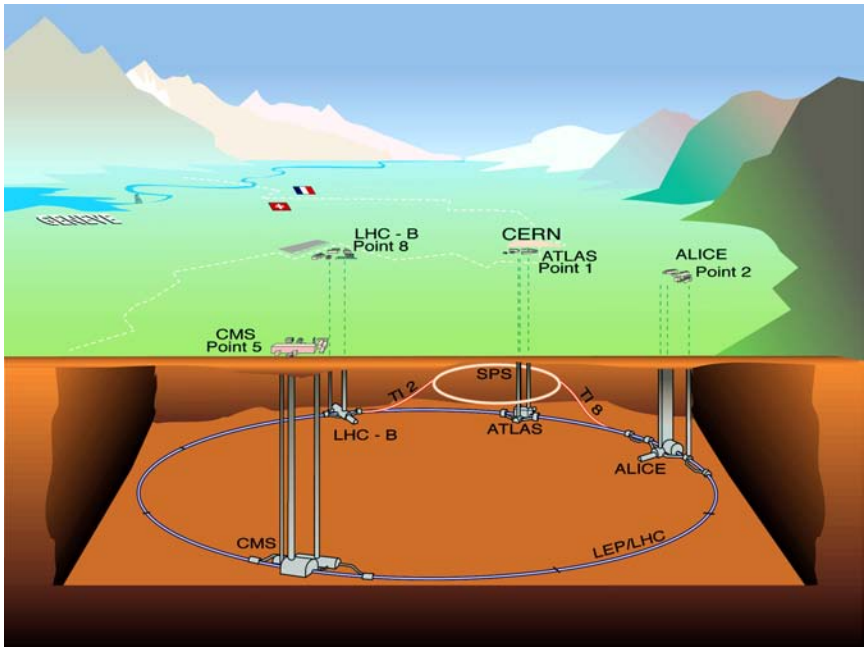

Figure 2.1: Schematic view of the LHC with its four main experiments [1].

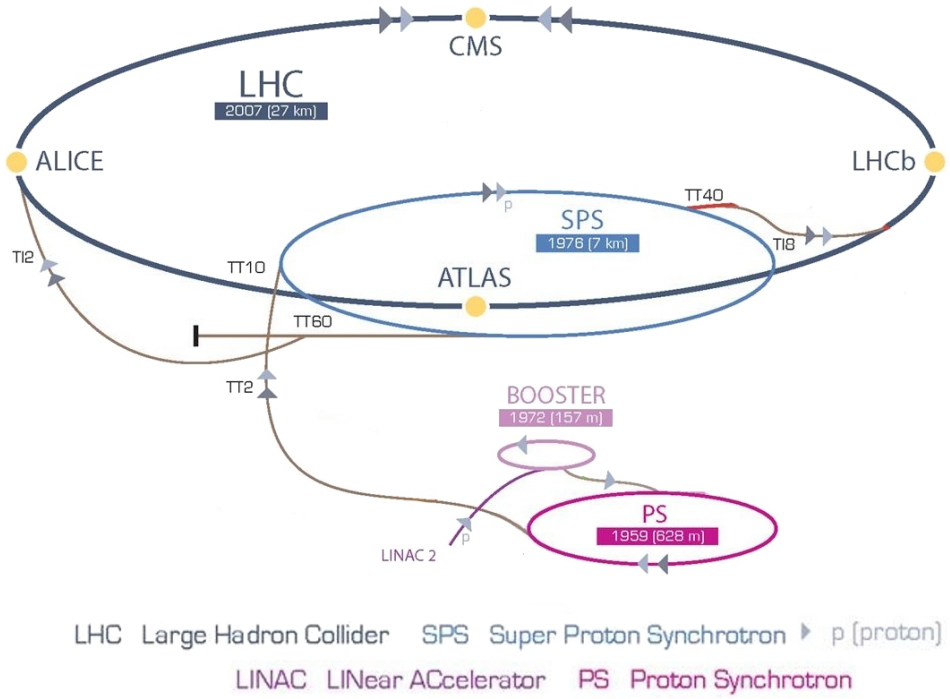

Figure 2.2: Schematic view of the LHC and its pre-accelerator complex. The accelerator chain starts with the Linac2, includes the booster, the PS and the SPS. The LHC is filled via two extraction lines: TI2 and TI8 [2].

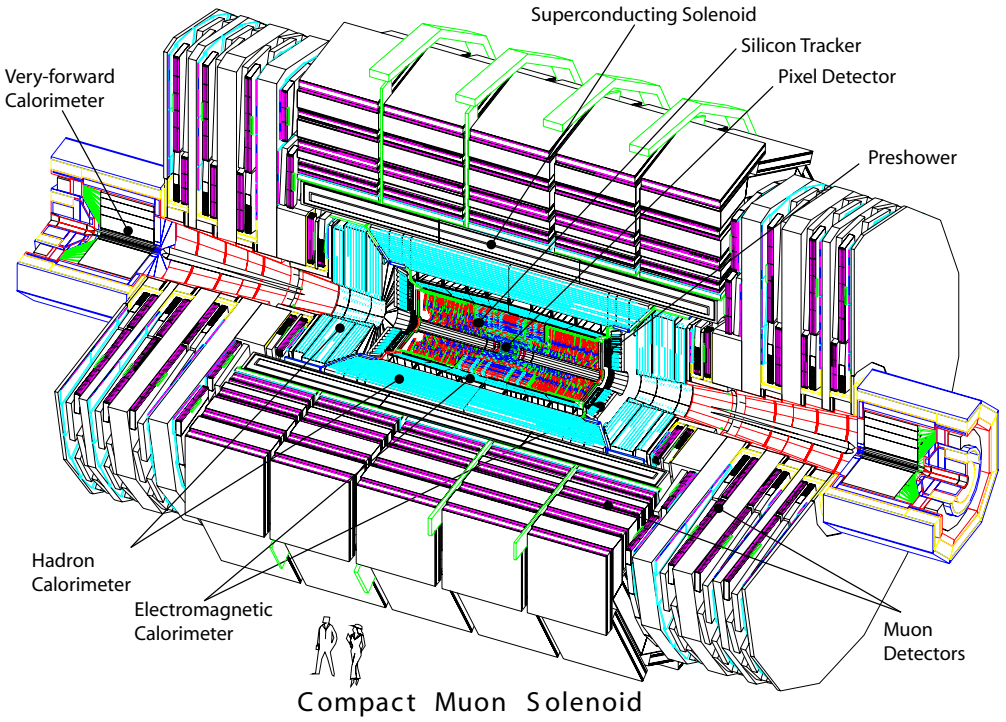

Figure 2.3: Schematic view of the CMS detector. In the figure one fourth is cut out, allowing an insight into the detector [3].

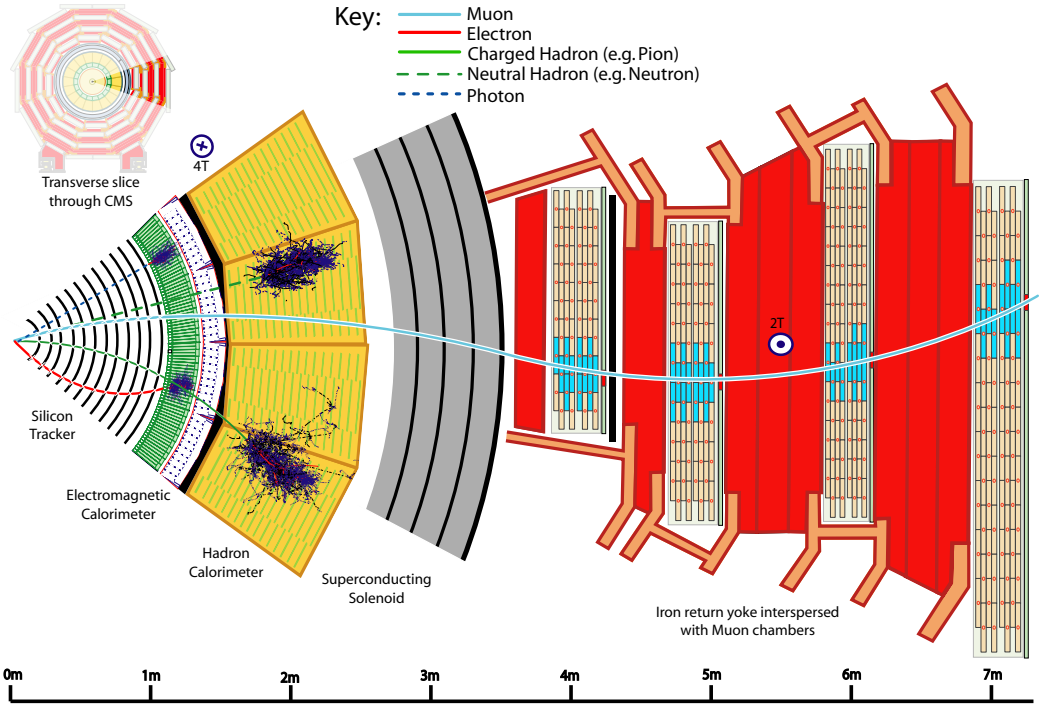

Figure 2.4: Transverse slice through the CMS detector. The interaction of different types of particles with the detector layers is illustrated [4].

Chapter 3

The Inner Tracking System of CMS

The CMS tracker [3] measures 5.8 m in length and 2.5 m in diameter, covering pseudorapidities from -2.5 up to 2.5. It is traversed by approximately 1000 particles every 25 ns, leading to an occupancy of up to 1%. To reduce reverse anealing and in particular thermal runaway effects due to the irradiation of the detector, the temperature of the tracking system is kept below $-10\,^{\circ}\mathrm{C}$. Thus a detector lifetime of at least 10 years is ensured. The tracker consists of a pixel detector in the inner part and a strip tracker in the outer region (Fig. 3.1).

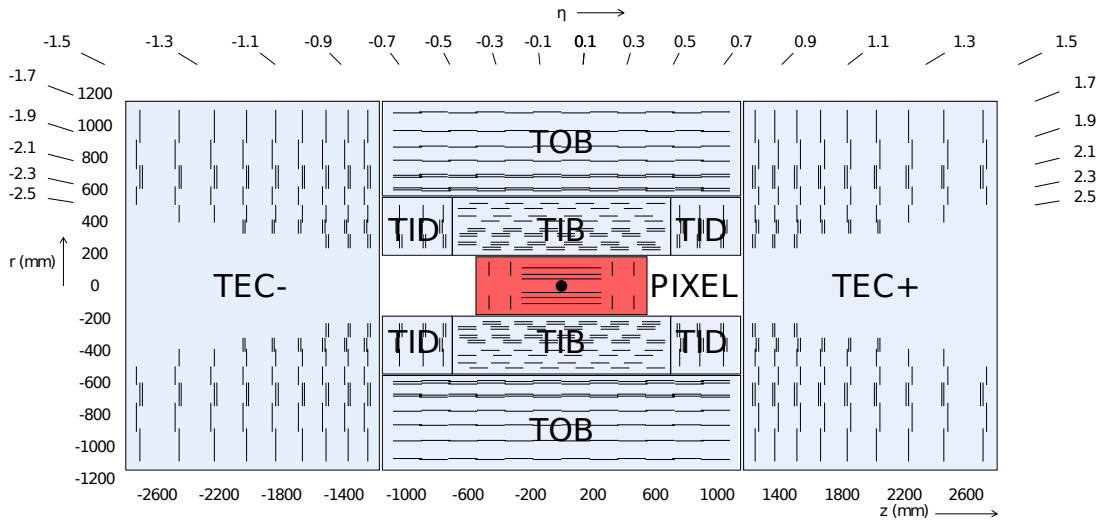

Figure 3.1: Schematic view of the inner tracking system. The pixel detector is coloured in red, the strip tracker is coloured in light grey [3].

The interaction point is surrounded by three cylindrical layers of hybrid pixel detector modules, which are complemented by two disks of pixel modules on each side. In total the pixel detector offers a sensitive area of about $1\,m^2$ containing 66 million pixels, with a cell size of 100×150 µm^2 each.

The silicon strip tracker occupies the radial region between 20 cm and 116 cm. It is composed of several subsystems. The innermost ones are the Tracker Inner Barrel (TIB) and Tracker Inner Disks (TID). They are surrounded by the Tracker Outer Barrel (TOB), which is complemented by a Tracker End Cap (TEC) on each side. Referring to their position along the z-axis, the tracker end caps are labelled TEC+ and TEC−. In total, the strip tracker provides 9.3 million sensor strips and an active silicon area of 198 m^2. Depending on the position withing the strip tracker, the microstrip pitch varies between 80 µm and 205 µm.

3.1 The CMS Silicon Strip Sensor Modules

All silicon sensors of the CMS strip tracker are integrated via so-called modules. In total there are 15 148 modules distributed throughout the strip tracker. Each module consists of a one or two sensors supported by a frame made of carbon fibre or graphite and is equipped with a hybrid PCB[1] containing the front-end readout electronics. The typical size of a single module is in the order of 100 cm^2, but depending on their position in the tracker the modules vary in size, shape, number of strips and support frame material. This leads to 29 different module, 15 different sensor and twelve different hybrid designs.

3.1.1 Charge Carrier Generation in Silicon Sensors

The silicon sensors [5] of the CMS tracker make use of the electron-hole pair production within reverse biased pn-junctions. The detectors are operated fully depleted. This is achieved by increasing the bias voltage until the so-called depletion voltage is reached and all free charge carriers are removed. An electron-hole pair is generated if an electron is lifted from the valence band into a free energy state of the conduction band. Direct transition from the valence band to the conduction band requires an energy of roughly 3.6 eV at room temperature. This value is significantly higher than the actual band gap of about 1.1 eV. The remaining energy is needed because silicon is an indirect semiconductor. An additional momentum transfer to the electron is needed because holes at the maximum valence band energy have a different momentum than electrons at the minimum conduction band energy. Thus the excitation with the minimal energy is a two-step process, which is mainly achieved by three phenomena: thermal excitation, irradiation with electromagnetic radiation and the passage of charged particles.

Thermal excitation is based on the phonon energy of the crystal lattice. Due to the Fermi-Dirac distribution it is not impossible but unlikely that an electron at room temperature ($E \approx k_B T = 0.025\,\mathrm{eV}$) is directly lifted into the conduction band. Still thermal excitation is not negligable. Intermediate energy levels in the band gap, caused by impurities of the detector material, allow a gradual accession of energy.

Excitation due to **electromagnetic radiation** is directly achieved if the energy of an absorbed photon exceeds the required 3.6 eV. In this case the electron is directly lifted into a state of higher energy in the conduction band. If the photon's energy is only slightly higher than the band gap of 1.1 eV, the transition can still be accomplished, if the additionally needed momentum is transferred to the electron through a phonon, or by another photon.

Charged particles can create electron-hole pairs due to ionisation. The mean ionisation energy loss per unit path length of a charged, massive particle in matter is described by the Bethe-Bloch formula, given in Equation 3.1:

$$-\frac{dE}{dx} = \frac{4\pi}{m_e c^2} \cdot \frac{nz^2}{\beta^2} \cdot \left(\frac{e^2}{4\pi\varepsilon_0}\right)^2 \cdot \left[\ln\left(\frac{2m_e c^2 \beta^2}{I \cdot (1-\beta^2)}\right) - \beta^2\right], \tag{3.1}$$

where $\beta = v/c$, v = velocity of the particle, E = energy of the particle, x = distance travelled by the particle, c = speed of light, ze = particle charge, e = charge of the electron, m_e = rest mass of the electron, n = electron density of the target, I = mean excitation potential of the target,
ϵ_0 = permittivity of free space.

The mean energy loss can be calculated by integrating Equation 3.1.

3.1.2 Layout of the CMS Silicon Strip Modules

Figure 3.2 shows an exploded view and a photograph of a TEC module. Like all tracker modules [3] it is assembled out of four main parts:

- A support frame made from carbon fibre or graphite.
- A flat Kapton foil delivering the bias voltage to the sensor back planes and insulating the sensor from the frame.
- A multi-layered PCB, also called Front-End Hybrid (FEH), hosting the front-end electronics.
- One or two silicon strip sensors.

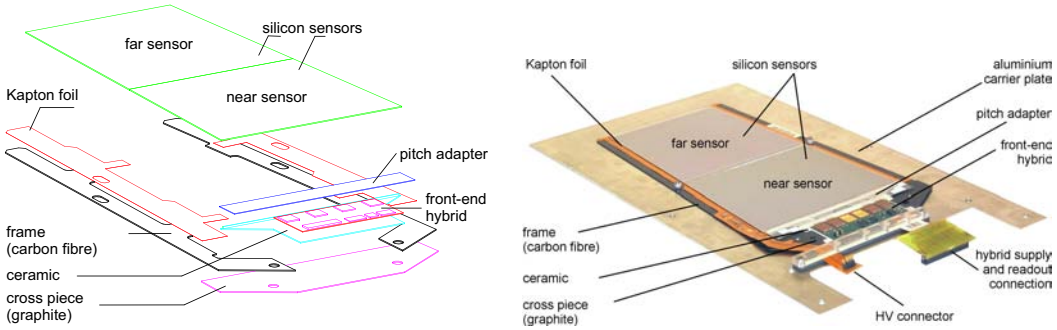

(a) Exploded view. (b) Photograph.

Figure 3.2: A CMS tracker silicon strip module with two daisy-chained sensors. The photograph shows a TEC ring 6 module, mounted on a carrier plate [3].

The module frame provides the mechanical support, as well as the thermal connection to the cooling system. The frame is connected with a conductive glue spot to the ground trace of the bias Kapton.

At radii of up to 55 cm from the centre of the beam pipe, modules contain a single 320 µm thick sensor. Modules at larger radii consist of two daisy chained sensors with a thickness of 500 µm [3]. Figure 3.3 shows the cross-section of a sensor edge. All silicon sensors [5] used in the tracker are fabricated of n-doped bulk material with p^+ strip implants on the front surface. The p^+ implants are AC coupled to aluminium strips, with an insulating multilayer of silicon oxide and silicon nitrate in between. The ends of the aluminium strips are completed by bond pads for the connection to a pitch adapter, or to the second sensor in two-sensor modules. The pitch adapter adapts the sensor strip pitch to the one of the readout chips.

The sensor back side, a n^+ implantation covered by an aluminium layer, is connected to the positive bias voltage of up to 500 V. The active surface of the sensor is surrounded by a p^+ bias ring which is at ground potential. All strip implants are DC coupled to this bias ring via an 1.5 MΩ polysilicon bias resistor. A p^+ implant guard ring, on a floating potential, surrounds the bias ring in order to gradually degrade the electric field between the n^+ implant at the cut edge of the sensor and the bias ring, which are at backplane potential (bias voltage) and ground, respectively. Except for the AC and DC pads, as well as parts of the bias and guard rings, the sensor surface is covered by a passivation layer to protect the active area.

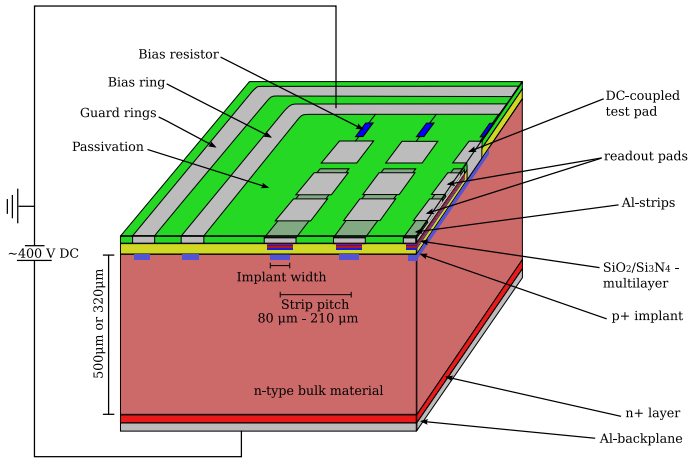

Figure 3.3: Cross-section of an edge of a CMS tracker sensor [6].

3.2 The Readout System

Two link systems are used to operate the CMS tracker [7]. Trigger, clock and control signals are transmitted digitally, while the actual data of the silicon modules are transmitted via an analogue link. Data of both

[1]Printed Circuit Board

systems are transmitted optically, allowing the use of optical fibres to bridge the distance of approximately 100 m between the detector and its service cavern. Fig 3.4 shows a block diagram of the CMS tracker readout scheme.

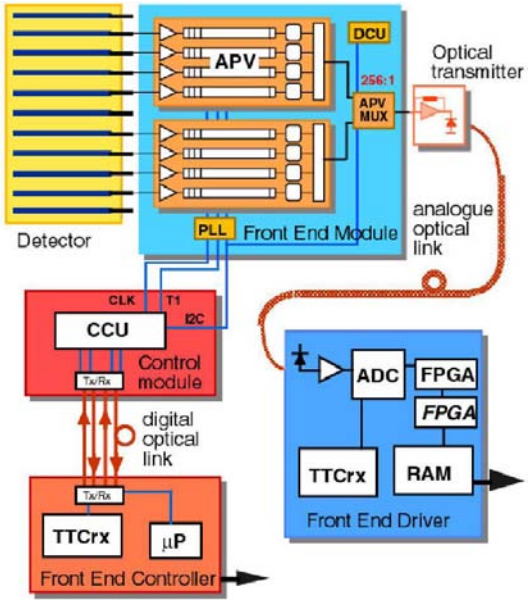

Figure 3.4: Block diagram of the CMS tracker readout scheme [3].

3.2.1 Control and Monitoring

The control signals are sent to the tracker by dedicated and programmable VME cards named front-end controllers (FEC) [8]. In the final design, a FEC is a 9U-size VME board that contains 8 mezzanine boards (mFEC). For smaller set-ups, an mFEC board can also be mounted on a PCI carrier plate (FEC-PMC). The digital data of the FEC are distributed through a digital optical link to the detector. Inside of the tracker volume, the data are received by Digital Opto-Hybrid Modules (DOHM) and converted into electrical Low Voltage Differential Signals (LVDS). The propagation of these signals to the detector modules is organised by chips called Communication and Control Units (CCU) [9]. Each CCU is mounted on a Communication and Control Unit Module (CCUM) and communicates with a set of modules (up to 16). Control data encoded in the I^2C standard [10] are sent to and received from the different front-end chips. Clock and trigger signals are combined in one single line and sent to a Phase Locked Loop (PLL) chip [11], located on the FEH [12]. This chip decodes the trigger signal and delivers a phase-adjustable clock to the module electronics. The aggregation of several CCUs into a token ring is also referred to as a control ring. The control rings are interfaced by one FEC per ring.

Each FEH is equipped with a Detector Control Unit (DCU) [13] chip, which allows to monitor the operating voltage of the front-end chips, the leakage currents drawn by the sensors and to read out several temperature sensors.

3.2.2 The Analogue Readout

The signals from the silicon strips receive a first treatment in the readout chips on the FEH, the APV25 [14, 15]. Upon arrival of a first level trigger signal, all 128 channels of each APV are multiplexed and output at a rate of 20 megasamples per second. The data of two APVs are multiplexed onto a single line in another front-end ASIC, the APVMUX [16]. The resulting stream of 40 megasamples per second is converted into optical signals by an Analogue Opto-Hybrid (AOH), which is located a few centimetres away from the module. The optical data are finally transmitted over a distance of about 100 m to the front-end drivers (FED) [17], located in the service cavern. Each FED processes the data of up to 96 optical channels in parallel. First the optical signals are converted into electrical signals and then digitised by a 10-bit analogue-digital converter (ADC).

3.2.3 The APV25 Readout Chip

The APV25 is manufactured in an intrinsically radiation tolerant 0.25 µm CMOS process. Each of its 128 readout channels provides a charge-sensitive preamplifier, an inverter stage, a CR-RC shaper and a 192 cells deep analogue pipeline. The different stages of the APV25 are displayed in Fig. 3.5.

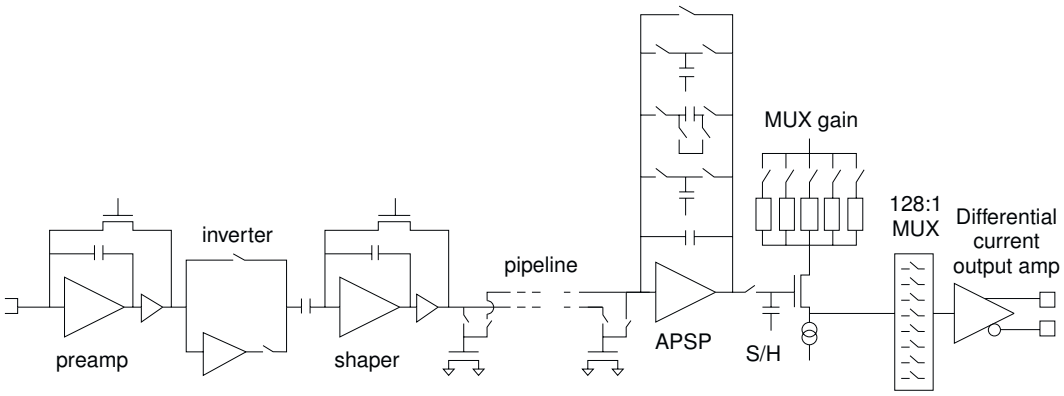

Figure 3.5: Block diagram of the APV25 readout chip [18].

The Preamplifier – The preamplifiers are wire-bonded to the pitch adapter. If a signal is initiated on a silicon strip of the module (i.e. by a traversing particle), the corresponding current is integrated and amplified by the preamplifier.

The Inverter – The unity gain inverter can be switched onto the preamplifier output. This function was integrated into a parent version of the APV25 and allowed to adapt to multistrip gas chambers with opposite signal polarities. Since all detectors within the CMS tracker have the same polarity, the inverter is always activated.

The Shaper – The CR-RC shaping filter forms a voltage pulse with a shaping time of 50 ns. The output voltage of this filter is proportional to the electrical charge generated by a particle traversing the silicon sensor. The level of the analogue data can be adjusted between two digital levels through the APV's VPSP register. The pulse, generated by the shaper, rises quickly to its maximum, but has a comparatively long falling edge (peak mode). This can lead to superimposed signal pulses during the high-luminosity operation at the LHC, if the same strip is being hit twice within a short time interval. In this case the pulse height would not be proportional to the input charge. To reduce this effect the APV can be operated in the so-called deconvolution mode [19]. In this case a weighted sum of three consecutive samplings is computed which effectively reduces the shaping time to 25 ns. Although the deconvolution mode increases the noise of the modules, it is used for standard operation of the CMS detector.

The Analogue Pipeline
Until a L1 decision is made data are stored for 4 µs in an analouge pipeline, which works as a ring buffer and is filled with the data sampled at the LHC clock frequency of 40 MHz.

The On-Chip Common Mode Subtraction
A notable feature of the APV is its ability to remove common mode (CM) noise[2] [20]. This is achieved within the inverter of the APV, by the subtraction of currents which are common for all channels of the APV. Figure 3.6 shows a simplified schematic of the preamplifier and the inverter of one APV channel (inverters of the other 127 channels are indicated). All inverters of an APV are powered from 2.5 V through an external resistor R, which is common for all channels. V_{in} represents a voltage induced by a signal on a single channel. V_{CM} is an unintended voltage seen by all channels of the APV at the same time, and V_{out} is the voltage at the inverter's output. With the current gain g_m of the transistor marked by the red oval,

[2]See Section 6.3.1 for more details about common mode noise.

the voltage drop V_R across R can be calculated from the current sum at the crossing marked by the blue rectangle:

$$\begin{aligned} V_R &= g_m R\left(V_{in} + V_{CM} - V_R\right) + 127 g_m R\left(V_{CM} - V_R\right) \\ &= \frac{g_m R\left(V_{in} + 128 V_{CM}\right)}{1 + 128 g_m R} \\ &\approx \frac{g_m R\left(V_{in} + 128 V_{CM}\right)}{128 g_m R} \\ &= \frac{V_{in}}{128} + V_{CM} \\ &\approx V_{CM}. \end{aligned}$$

The output current of the inverter channel which received the signal is given by:

$$g_m\left(-V_{out}\right) = g_m\left(V_{in} + V_{CM} - V_R\right), \tag{3.2}$$

thus

$$V_{out} = -V_{in}. \tag{3.3}$$

Hence the APV removes the unintended voltage V_{CM}. It has to be noted that this calculation assumes V_{CM} to be exactly the same for all channels. However measurements have shown signals which are common mode like, in the sense of being generated by a common source and not being intrinsic, but which are also non-uniformly spread through the APV. If such a non-uniform CM occurs, the V_{CM} in Equation 3.2 has to be replaced by the actual V_{CM} of that channel. This means, the APV removes only flat CM, regardless of the real CM distribution.

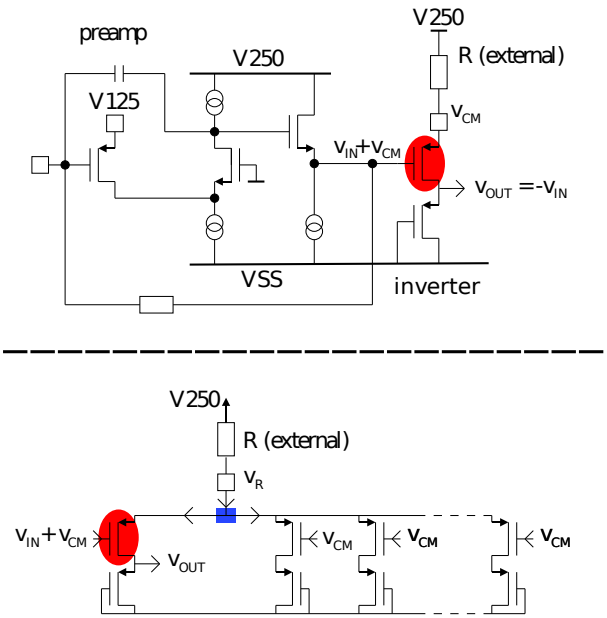

Figure 3.6: Implementation of the on-chip common mode subtraction of the APV. Top: Preamplifier and inverter stage of a single APV channel. The external resistor R is common for all channels. Bottom: Inverter stages of all 128 channels [20].

3.3 The Tracker End Caps

The set-up used for the system tests presented in this document is based on components of the TEC. Each TEC [3, 6] consists of 11 carbon fibre discs, of which disks 1-9 are instrumented with silicon modules. The strips are oriented radially. Starting with the disc closest to the interaction point, the discs are numbered serially. Two photographs of the TEC+ are shown in Fig. 3.7.

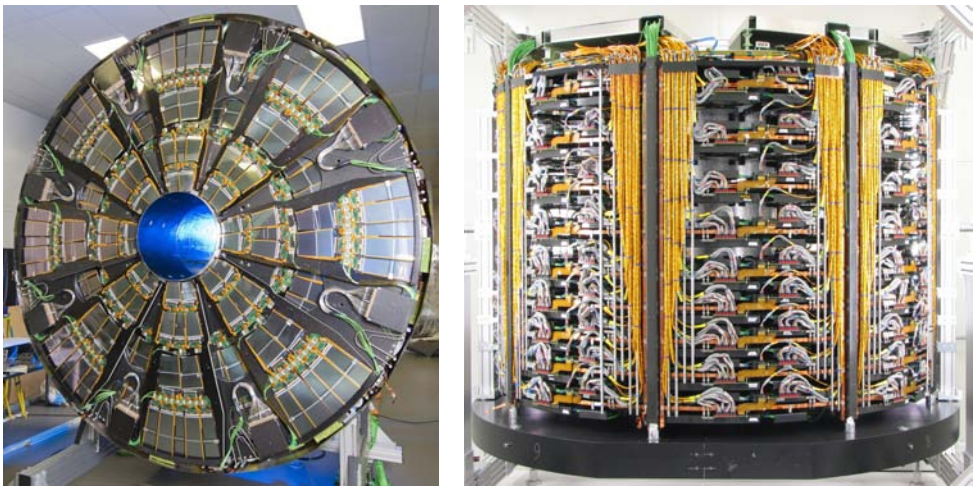

(a) Front view of disc 1. (b) Side view.

Figure 3.7: Photographs of the TEC+ without coverskins.

The modules of the TEC are not mounted directly on the support discs but on roughly trapezoidal sub assemblies called petals. Each disc hosts eight front petals and eight back petals mounted in alternating order on the disc sides facing the interaction point and the far end of the detector. Figures 3.8 and 3.9 show a pair of front and back petals. The side of a front petal oriented towards the interaction point is called side "A", the opposite side is labelled "B". The two sides of a back petal are referred to as "C" and "D".

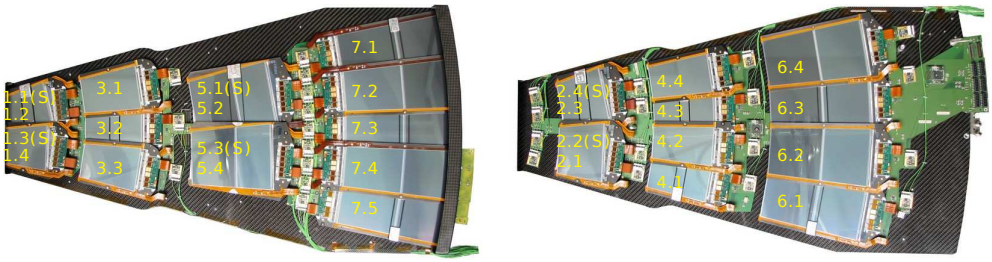

(a) Side A. (b) Side B.

Figure 3.8: Photographs of a front petal. Stereo modules are indicated by (S).

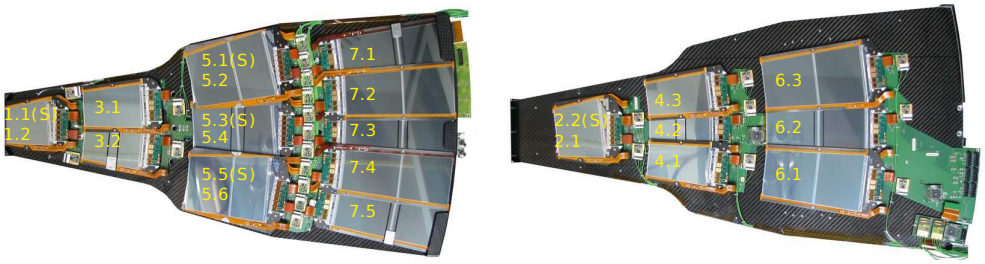

(a) Side C. (b) Side D.

Figure 3.9: Photographs of a back petal. Stereo modules are indicated by (S).

Petals provide mechanical support as well as the cooling and electronic infrastructure for the modules. A titanium cooling pipe is embedded into the body of the petal to ensure that the operating temperature of the modules remains below -10° C. A so-called InterConnect Board (ICB) is mounted onto the petal surface and establishes the electrical connections to the modules.

Within a petal, the modules are arranged in up to 7 rings, with odd ring numbers mounted on the petal side A/C, while even ring numbers are mounted on side B/D. The rings of each petal are numbered, starting with the ring nearest to the centre of the TEC. Due to geometrical constrains, layout and shape of the modules differ, depending on which ring they are mounted on. Rings 1, 2 and 5 carry double-sided modules, where two modules are mounted back-to-back with a stereo angle of 100 mrad which allows to measure r. Both modules of such a double-sided module have 768 strips. The modules of the rings 3, 4, 6 and 7 are single-sided and host sensors with 512 strips. Furthermore modules of the rings 1-4 contain only a single thin (320 µm) sensor, while modules of rings 5-7 are composed of two thicker (500 µm), daisy-chained sensors. Since the tracker was designed to cover the region within $\eta \leq 2.5$ the number of rings per petal has to decrease for higher values of |z|. Therefore only on the petals of discs 1-3 all seven rings are present. From disc 4 onwards, ring 1 is missing; beginning with disc 7, ring 2 is left out as well and on disc 9, only rings 4-7 are mounted.

3.3.1 The InterConnect Board

InterConnect Boards [6, 21] are multi-layered PCBs, mounted on the front and back side of each petal. They integrate the DOHMs, the DOHs, the CCUs and the AOHs into the TEC system, and are based on a modular design. Figure 3.10 shows the five individual boards. The main ICB, the ICB_46, is mounted on the B/D side of the petals. It carries the connectors for power and control cables and provides two sockets for CCUMs. On back petals, the ICB_46 furthermore carries a connector for the DOHM. The other ICBs are connected to the ICB_46. The numbers in the ICB names indicate the rings to which the connected modules belong.

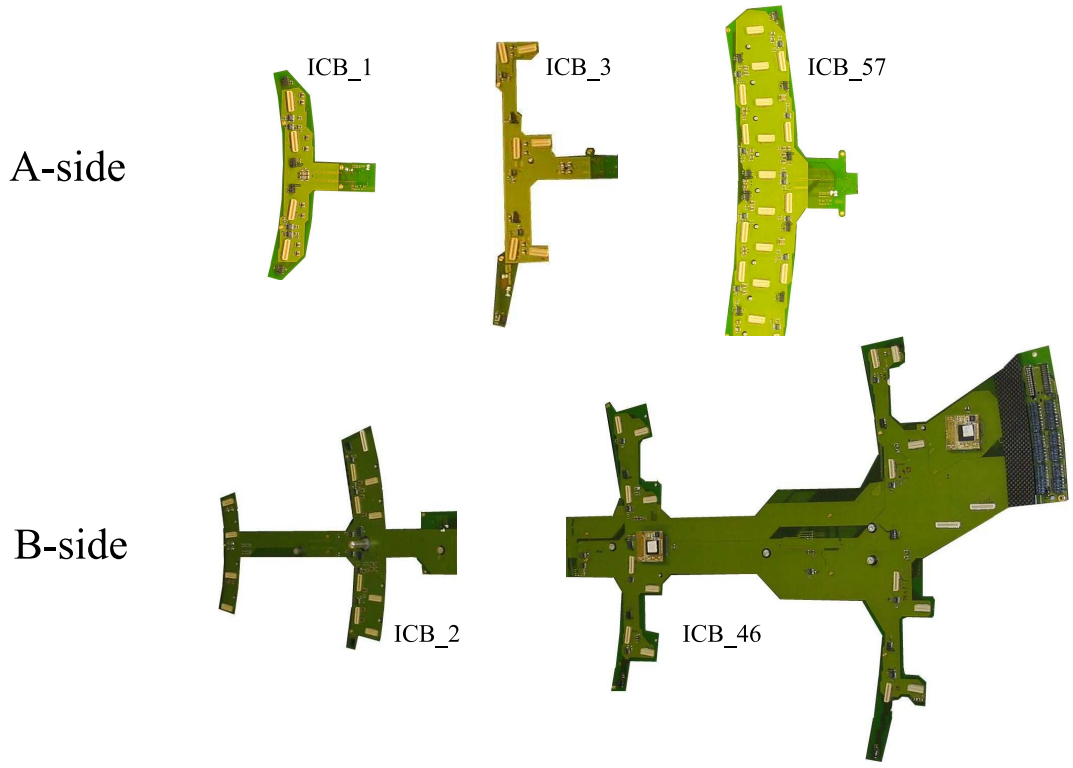

Figure 3.10: The five parts of a front petal ICB. In the top row the three boards for the A side of the petal are shown, in the bottom row the two boards for the B-side of the petal. The ICB 2 has all connectors for the ring 2 modules and the connectors for the AOHs of ring 1.

The connection between the FEH of the modules and the ICB is established through two short Kapton cables per module. One cable is required for the LV as well as for the readout and control data, the other one supplies the bias voltage. The modules are arranged in three power groups. Power group 1 consists of the modules of rings 1 and 2, power group 2 contains the modules of rings 3, 4 and 6. The modules of rings 5 and 7 form power group 3. Each group is connected to a multi-service power cable via two sixteen-pin Molex connectors. These connectors, shown in Fig. 3.11, are mounted on the outer radius of the main ICB. Per power group, two connectors are used: one for the bias voltage, the other one for the low voltages.

The ICB's ground is implemented by a 2 cm wide and 20 µm thick copper path along the centre of the ICB.

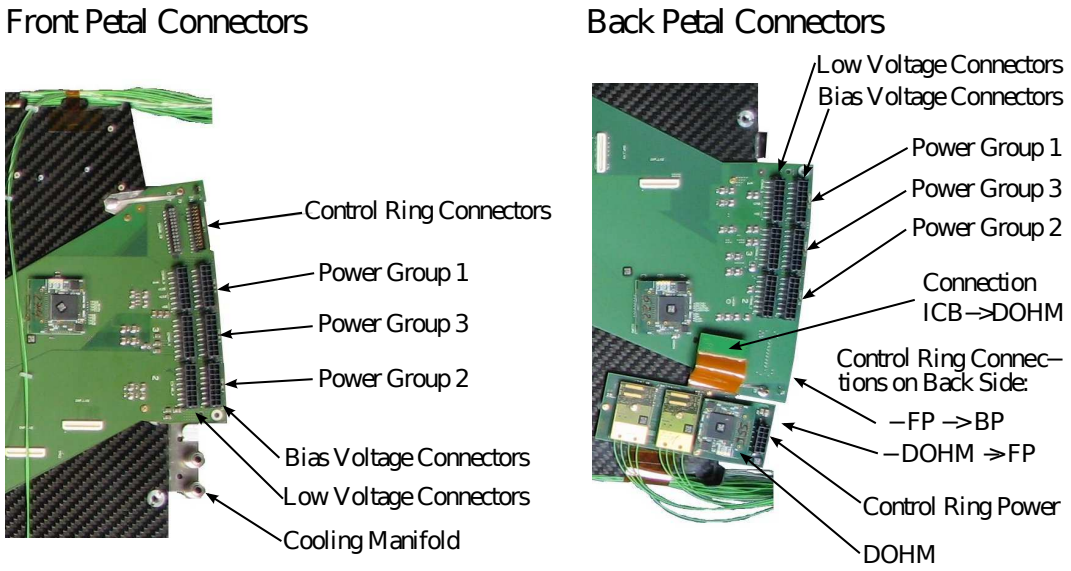

Figure 3.11: Connections of front and back petals to the tracker system [6].

3.4 Power Consumption and Distribution

Each tracker module requires three different voltages to be operated: two low voltages (LV) (1.25 V and 2.5 V) to power the front-end electronics and one high voltage (HV) (0-500 V) to bias the sensors of the detector [3, 22, 23]. Depending on the number of readout chips, the average power consumption per module varies between 1845 mW (4 APVs) and 2662 mW (6 APVs) [3]. About 80% of the power is supplied through 2.5 V and 20% through 1.25 V. After 10 years of service and irradiation, the power loss due to HV leakage currents is expected to remain below 0.6 W per module. Monitoring and control electronics are powered via an independent 2.5 V line.

Based on the mechanical structure of the tracker, its modules are subdivided into power groups, of about 10 modules. The modules of each power group are powered in parallel by a floating Power Supply Unit (PSU) [22], which is instrumented with two regulators for the HV and one regulator for each LV. In addition, a single regulator provides 2.5 V to power the control electronics. The 1.25 V regulators can provide up to 6 A, regulators for 2.5 V offer up to 13 A and the HV regulators are capable of providing up to 10 mA. All PSUs are programmable and can be controlled remotely by a CANBUS interface. Two PSUs of the same type form one power supply module (PSM).

The tracker power supplies are placed on balconies in the experimental cavern. Thus they have to be radiation tolerant. Approximately 40 m long low impedance cables (LIC) [24], based on copper conductors, are routed from the PSUs to a patch panel (PP1) close to the tracker. The connection from PP1 to the tracker is established by approximately 5 m long LICs with aluminium conductors [22]. An exceptions is the TEC, which is connected to PP1 via copper cables[3]. The PSUs monitor the voltage drops across the LICs via sense wires. Fluctuations of up to 4 V can be compensated.

The total power consumption of the strip tracker is about 68 kW of which approximately 50% are lost in the 45 m long cables. This is increased if higher currents are needed. The present tracker requires 15 kA.

[3]Only the connection between the TEC and PP1 is established via copper cables. Cables within the TEC are made of aluminium.

To provide a sufficient safety margin, the power supply system is capable to supply up to 25 kA via 50 m long cables.

3.5 Noise Sources within the Silicon Strip Modules

The total noise of a silicon module is a composition of intrinsic noise, generated within the module itself, and noise contributed by the surrounding system. Typical origins of the latter are for example power supply noise or electromagnetic emissions, generated by electronics close to the sensor modules. Common sources of intrinsic noise are [25] [26]:

- Thermal noise: this noise affects virtually all electronic components, as it is generated by thermal fluctuations of the electron distribution in conductors.
- Low-frequency voltage noise: this noise is seen in most electronic devices and has a noise spectrum which is approximately proportional to $1/f$. Its physical source is not unique, and differs widely for different types of electronic elements. In unipolar transistors, the physical origin of low-frequency voltage noise are crystal defects, which cause trapping of charge carriers. Movable charge carriers become bound and are released with some time delay. This induces additional charges in the channel and thus modulates the transistor current. In this case the low-frequency voltage noise is temperature dependend as well.
- Shot noise: the discrete nature of electric charge leads to statistical fluctuations in the number of charge carriers, making up a charge $Q = Nq$. These fluctuations cause shot noise. In contrast to the thermal noise, shot noise can only occur if an external power supply causes a current flow. An example is a reverse biased detector.
- Divider Noise: this type of noise is caused by current division. For example in a bipolar transistor the emitter current is divided between the base and the collector. An electron injected in the emitter can either reach the collector, or will be recombined in the base. The mechanism is a statistical process, which behaves like an independent noise source.
- Induced noise: moving charges in a conductor induce currents in conductors nearby. An example is an electron, moving from the source to the drain in a field effect transistor. The movement of this electron causes a small alternating current in the gate of the transistor.

Often, the noise of a silicon detector system is expressed in terms of equivalent noise charge (ENC) referred to the input [18]. The different noise sources are either connected in series or in parallel to the signal source and cause serial or parallel noise, respectively. In a simple approach, the noise of the environment is neglected and the contributions to the intrinsic module noise are assumed to be:

- Amplifier noise ENC_A, which is composed of series (ENC_S) and parallel noise (ENC_P). The series part scales with the load capacitance C appearing at the amplifier input. This capacitance is proportional to the length of the sensor strips. The amplifier's parallel noise is independent of C. Hence, the amplifier noise ENC_A can be expresses as:

$$ENC_A = ENC_S \cdot C + ENC_P. \tag{3.4}$$

- Series noise $ENC_{C,S}$ from the readout strip resistance R_S:

$$ENC_{R,S} \propto C \cdot \sqrt{R_S/\tau}, \tag{3.5}$$

  where τ is the peaking time of the readout chip.

- Parallel noise depending on the polysilicon resistors R_P:

$$ENC_{R,P} \propto \sqrt{\tau/R_p}. \tag{3.6}$$

- Parallel noise ENC_{leak} from the leakage current I_{leak} of the detector.

$$ENC_{leak} \propto \sqrt{I_{leak} \cdot \tau}. \tag{3.7}$$

Since the individual sources are uncorrelated, the total noise figure is the square sum of the individual contributions:

$$ENC^2 = \sum ENC_i^2. \tag{3.8}$$

The parallel noise contributions are decreased for shorter peaking times, while the series noise is increased.

In peak mode the average ENC of a strip tracker module is given by [3]:

$$ENC_{peak} = (36.6 \pm 1.9) L \, \frac{\mathrm{e}}{\mathrm{cm}} + (405 \pm 27)\,\mathrm{e}, \tag{3.9}$$

where L is the strip length. The average ENC in deconvolution mode is given by:

$$ENC_{dec} = (49.9 \pm 3.2) L \, \frac{\mathrm{e}}{\mathrm{cm}} + (590 \pm 47)\,\mathrm{e}. \tag{3.10}$$

Chapter 4

Super LHC

The Super Large Hadron Collider (SLHC) [27, 28] is a proposed upgrade of the LHC. It is intended to increase the instantaneous luminosity of the machine by a factor of 10 to $10^{35}\,\mathrm{cm}^{-2}\mathrm{s}^{-1}$. This would allow to improve statistically marginal measurements and extends the discovery reach in the high mass region.

The goal of the first SLHC phase is to double the instantaneous luminosity of the LHC by relatively small hardware changes. It is forseen to circulate more protons per bunch or to reduce the beam cross-section at the interaction points. Assuming phase I to be applied successfully, the LHC's integrated luminosity could reach $500\,\mathrm{fb}^{-1}$ in about ten years. At this point, parts of the detectors and the accelerator [29] will have to be replaced, due to radiation damages. Figure 4.1 shows a potential time map towards the SLHC.

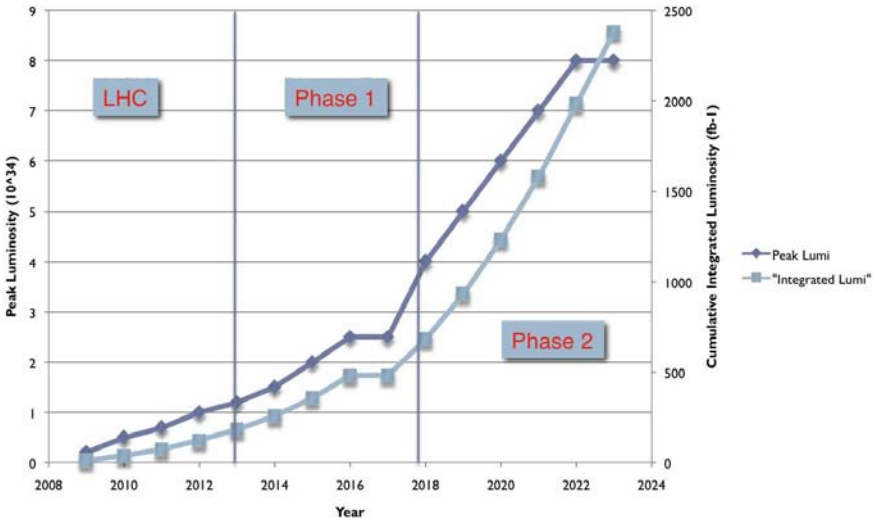

Figure 4.1: Potential LHC upgrade roadmap [30].

4.1 Physics Motivation

Since the LHC is just commencing operation it is yet impossible to predict for sure what the fields of interest will be after the first years of LHC data acquisition. Assuming the LHC to find the Higgs boson and Supersymmetry in the mass ranges that are expected today, the physics potential of the SLHC can be roughly divided into the following main topics:

1. Reduction of statistical errors; after 4–5 years of operation at $10^{34}\mathrm{cm}^{-2}\mathrm{s}^{-1}$, the time to halve the statistical error will exceed 5 years.
2. Improvements of precision measurements of Standard Model (SM) parameters (e.g. triple (TGC) and quartic (QGC) gauge boson couplings, Higgs couplings).

3. Improvements of measurements of New Physics parameters, possibly discovered at the LHC (e.g. sparticle spectroscopy in Supersymmetry, $tan\beta$ measurements).

4. Extension of the discovery reach in the high-mass region (e.g. quark compositeness, new heavy gauge bosons, multi-TeV squarks and gluinos, Extra-Dimensions).

5. Extension of the sensitivity to rare processes (e.g. FCNC top decays, Higgs-pair production, multi gauge boson production).

The different topics demand different abilities from the detectors. For example searches at the high-mass frontier, in most cases through the detection of multi-TeV objects, should not be impaired by the high luminosity environment. However, accurate measurements of objects in the few hundred GeV range could be significantly affected by the larger event pile-up.

To exploit the benefits of the increased luminosity completely, a good b-tagging efficiency and jet energy resolution are mandatory requirements. However, some topics will likely not benefit from the SLHC. For example B physics could suffer seriously from the difficulties to reconstruct low momentum particles.

4.2 Upgrade of the Accelerator

The instantaneous luminosity at the interaction points of ATLAS and CMS is proportional to:

$$L \propto \frac{n_b N_b \Delta Q_{bb} F_{profile} F_{hg}}{\beta^*}, \tag{4.1}$$

where n_b is the number of protons per bunch, β^* is linked to the beam diameter at the interaction point, N_b is the number of bunches per beam, ΔQ_{bb} denotes the total beam-beam tune shift, $F_{profile}$ is the form factor for the longitudinal beam profile and F_{hg} is the reduction factor due to the hourglass effect[1].

The LHC upgrade plans aim at the optimisation of these parameters. An overview of the main beam parameters in the different upgrade phases is given in Table 4.1.

The first phase of the accelerator upgrade is intended to double the instantaneous luminosity. To achieve this goal, two different upgrade scenarios have been proposed: to increase the number of protons per bunch, or to halve the beta function at the IP.

Concerning phase II, more protons per bunch would lead to the so-called "early separation" scenario (ES), while a smaller beta function would initiate the "large Piwinski angle" scenario (LPA)[2].

The early separation scenario [32] provides a very small β^* function of 8 cm and an effective beam-beam crossing angle equal to zero. To achieve such a small value, early beam separation dipoles would have to be installed approximately 3 m from the IP, within the detectors. Optionally, a quadrupole doublet could be included about 13 m from the IP. The ES scenario implies the use of new so-called crab cavities to ensure the extremely small crossing angle.

The major merit of this scenario is the negligible effect of most long range collisions, due to the early separation and the fact that the beam current would not have to be increased further.

Challenges implied by the ES scenario are the integration of the early separation dipoles into the detectors and the requirement of crab cavities. In addition, the increased number of protons per bunch in combination with a bunch spacing of 25 ns might exceed the heat load limit of the beam pipe. This problem could already occur in phase I.

The large Piwinski angle scenario [29] is based on a moderate reduction of β^* down to 25 cm during phase I . Additional accelerator components within the detectors would not be required. In the second phase longer and more intense bunches, separated by longer bunch spacings of 50 ns, would be provided. Due to its asymmetric design and the 50 ns bunch spacing, LHCb would see no collisions in the first instance, but the LPA scenario also allows to add low charge satellite bunches in between the main bunches and thus LHCb could continue operation.

An important merit of this scenario is the absence of any accelerator components inside the detectors. In addition, the desired luminosity can be achieved without the use of crab cavities, although they could be

[1] The beam size during a collision can change due to the hourglass effect, if the bunches are shorter than or as small as β^*.

[2] The Piwinski angle ϕ is directly linked to the horizontal crossing angle θ of the colliding beams. A common definition is $\phi = \frac{\sigma_z}{\sigma_x} tan\,(\theta)$ [31], where σ_x and σ_z are the r.m.s. bunch sizes.

implemented to boost the luminosity even further. However, the LPA scenario implies challenges as well. No other scenario leads to more pile-up events per bunch crossing. The high bunch charge will likely require major upgrades of the LHC's pre-accelerators. And no other hadron collider has been operated with a large Piwinski angle before.

	LHC	SLHC (ES)	SLHC (LPA)
Peak luminosity $[10^{34}\text{cm}^{-2}\text{s}^{-1}]$	1	15.5	10.6
Average luminosity (10h) $[10^{34}\text{cm}^{-2}\text{s}^{-1}]$	0.5	2.4	2.5
Number of bunches n_b	2808	2808	1404
Protons/bunch N_b $[10^{11}]$	1.15	1.7	4.9
Bunch spacing [ns]	25	25	50
Beta at IP β^* [m]	0.55	0.08	0.25
Effective crossing angle [μrad]	285	0	381
Average number of pile-up events	19	294	403
Form factor $F_{profile}$	1	1	$\sqrt{2}$
Hourglass reduction factor F_{hg}	1	0.86	0.99

Table 4.1: Main beam parameters of the different LHC upgrade stages [29].

4.3 Upgrade of the CMS Detector

The CMS detector will have to maintain its performance to exploit the full potential offered by the SLHC. At the same time the conditions will be more challenging [28]. Figure 4.2 shows a Higgs decay simulated within the CMS tracker, under different LHC conditions and for the ES SLHC scenario. The interesting decay ($H\rightarrow ZZ\rightarrow ee\mu\mu$) is superimposed by 300 pile-up events. If the LPA scenario is chosen, the number of pile-up events would be even higher, 400 on average. CMS will require major upgrades to cope with the extreme SLHC environment. In the following the changes required in the different subdetector systems are described.

The CMS tracking system will have to be replaced for the SLHC. After 10 years of LHC operation, the silicon sensors will have reached the end of their lifetime due to radiation damage. In addition, the radiation hardness of the current sensors is not sufficient for the harsh environment of the SLHC. The total ionising dose will be approximately 10 times higher than during LHC operation. The number of pile-up events will increase on average by a factor of 15 to 20. Hence the granularity has to be increased by a similar factor, to keep the occupancy at a reasonable level.

A complete new tracker system will be needed to provide the required granularity and radiation hardness. To preserve the present physics performance, the material budget will have to maintain at its present level. The performance of a new tracker would benefit from a reduction of the material. Figure 4.3 shows the material budget of the present CMS tracker as function of the pseudorapidity η. The main contributions are support structures, electronics, cables and cooling. To reduce the material budget of the tracker, a new tracker layout with less layers, as well as a decrease of the material needed per channel are under discussion.

The material needed per channel could be reduced by decreasing the power consumption per readout channel, as thinner cables and less cooling would be required. Finer sub-micron CMOS technologies and smaller sensor capacities of smaller pixels/strips are expected to reduce the power consumption per channel. However, the increase of channels per unit area may still result in an overall higher power consumption. The increased number of readout channels may furthermore lead to more data traffic which would also require additional power.

Another reason to reduce or at least maintain the present power consumption is the limited space available for the routing of cables and cooling pipes from the detector to the service balconies. Already the present tracker utilises this space completely.

To reduce the amount of power losses two novel powering schemes have been proposed: Serial Powering and DC to DC conversion. Both intend to save power by supplying the required amount of power at a higher voltage. In a scenario based on Serial Powering, several modules are daisy-chained and powered in series. The voltage drop across the chain equals the voltage drop per module times the number of modules powered in series. In a scheme with DC-DC converters, the modules are powered in parallel. A multiple

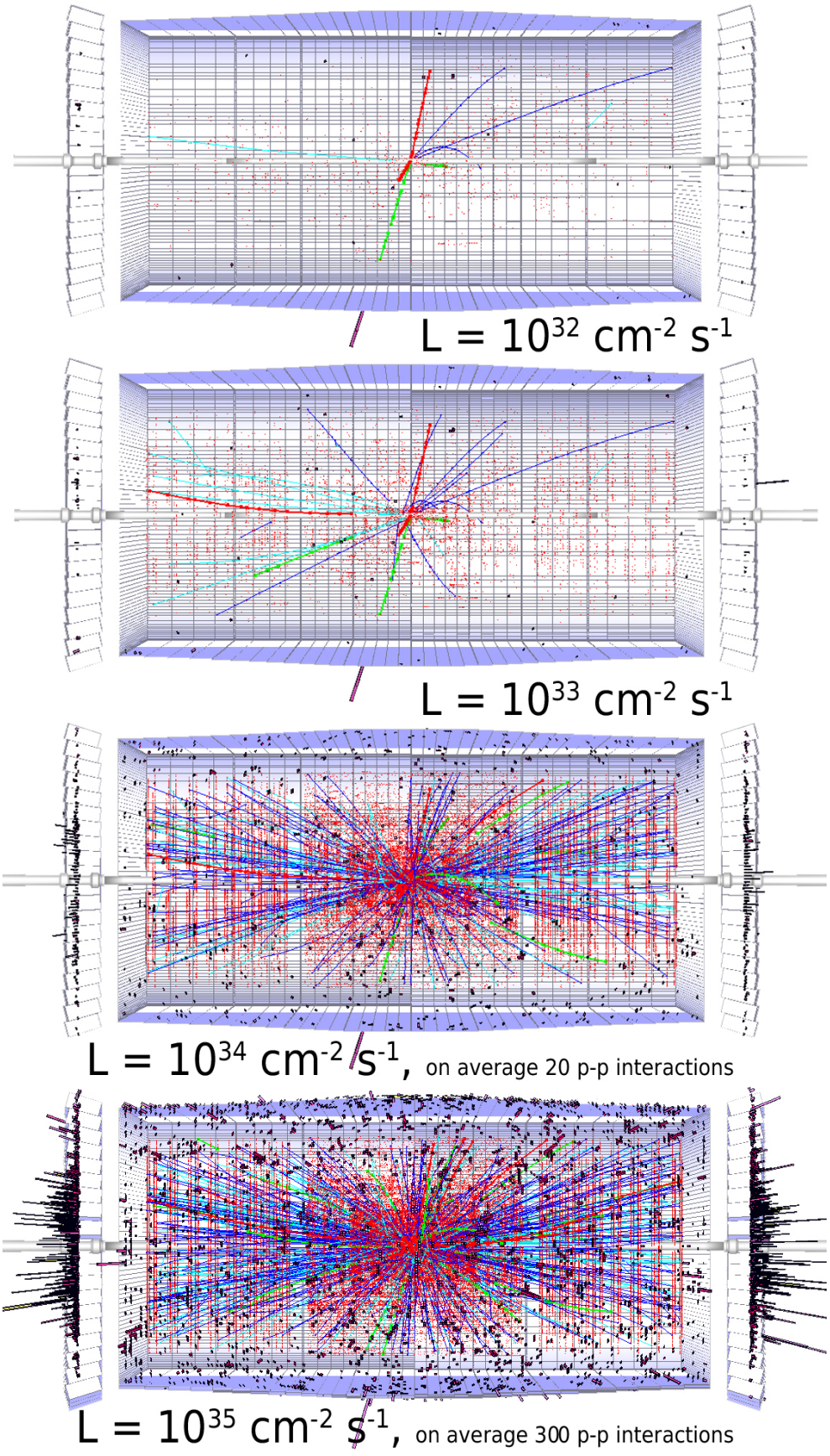

Figure 4.2: Simulated decay $H \rightarrow ZZ \rightarrow ee\mu\mu$ with backgrounds at different luminosities [30].

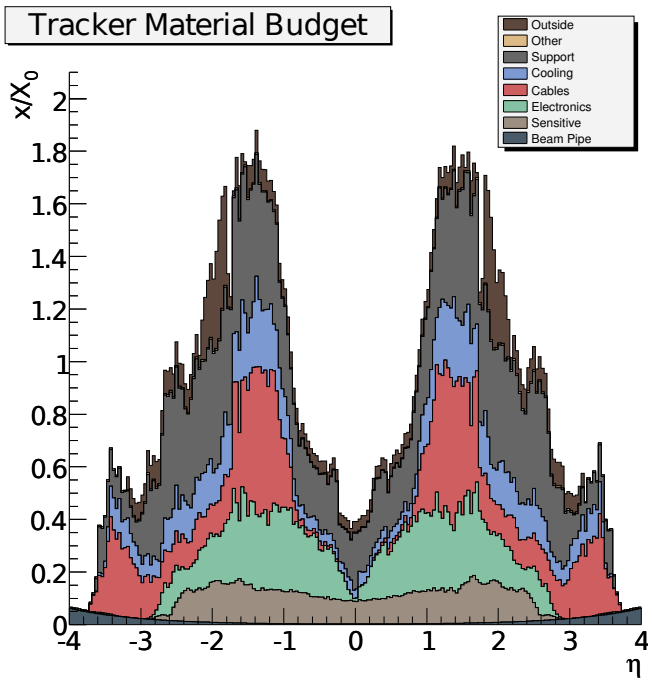

Figure 4.3: The material budget profile of the present CMS tracker as a function of the pseudorapidity η [33].

of the required voltage is supplied to the converters, which are placed closed to the modules and provide them with the low, required voltage. More details about DC-DC conversion and Serial Powering are given in Chapter 5.

The trigger and data acquisition systems (TRiDAS), which make use of cuts on the transvers momenta p_T of traversing particles, will need significant modifications to cope with the SLHC design luminosity. The present approach forsees to maintain the level 1 trigger rate at 100 kHz. However, since a further increase of the p_T thresholds is very inefficient, it is necessary to increase the p_T resolution of the trigger. This could be achieved by integrating data of the tracking system into the level 1 trigger. Due to the considerable amount of power required to transfer large data volumes at high speed it seems likely that some amount of data processing and correlation will already be implemented within the tracker. A promising concept proposes two dedicated module layers in close radial proximity to each other, allowing a measurement of transverse particle momenta inside the tracker.

The electromagnetic calorimeters' barrel region is designed to withstand the expected integrated luminosity of the SLHC. There should be no need to replace on-detector electronics. Changes may need to be made to off-detector electronics to accommodate a new trigger and DAQ system. The end cap calorimeters may suffer from reduced performance at high luminosities, but the on-detector electronics should continue to operate.

The hadronic calorimeters' barrel region should withstand the SLHC environment. Still, improvements in the particle recognition in the outer hadronic calorimeter are desirable, and the high η region of the hadronic end caps will have to be replaced. If the EA scenario is chosen to upgrade the accelerator, the forward hadronic calorimeter will be obstructed by elements of the machine placed inside CMS. The HCAL readout electronics may need to provide a higher readout bandwidth and a finer granularity for trigger primitive generation.

The muon chambers have been designed to tolerate hit rates a few times larger than those expected at the LHC. They seem still adequate for use at the SLHC, although more R&D work and LHC data is necessary to substantiate this prediction, in particular for the larger pseudorapidity regions. Upgrades will be needed for front-end electronics, trigger and readout electronics, in order to cope with the larger hit rate and to tolerate the SLHC radiation background. In addition, the digital electronics has to adapt to the SLHC bunch crossing frequency, if the LPA scenario will be chosen.

Chapter 5

Novel Powering Schemes

5.1 DC-DC Conversion

A DC to DC converter [34, 35] is an electronic circuit which converts the voltage of a direct current (DC) source into another DC potential. If the original level V_{in} is higher than the resulting one V_{out}, the according converter type is called step-down. Step-down converters are divided into linear regulators and switching devices. Switching step-down converters can again be divided into isolating and non-isolating devices. Isolating converters have no electrical path between source and load and are based on transformers. Non-isolating devices have a common ground between load and source. They combine a switch between source and load with an energy buffer to provide a constant output voltage.

Examples for non-isolating step-down converts are the "buck converter" and the "charge pump". These two particular topologies are described in the following, as they are promising candidates for future CMS powering schemes. All studies described in this work have been performed with buck converters.

5.1.1 The Buck Converter

Buck converters [34, 35] are relatively simple step-down switching devices. Due to their simplicity and potential of high efficiency, they are often used in commercial applications. Figure 5.1 illustrates the functional principal of a buck converter.

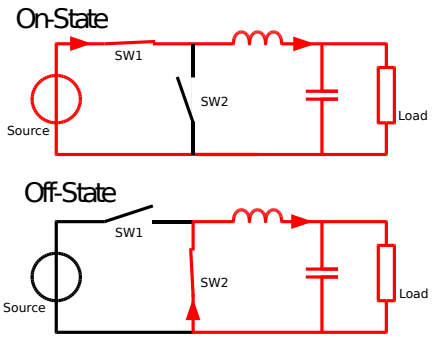

Figure 5.1: Sketch of DC-DC converter in on- and off-state. Top: in the on-state, energy is stored within the inductor. Bottom: during the off-state stored energy from the inductor is used to power the load.

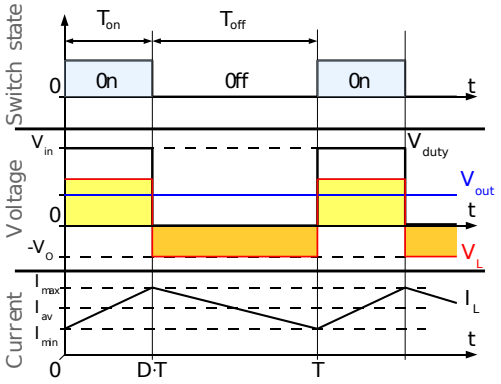

Figure 5.2: Evolution of voltage and current with time in a buck converter operated in continuous mode.

At a given point in time the switch SW1 is closed (On-State) and the voltage V_L across the inductor is given by:

$$V_L = V_{in} - V_{out}, \tag{5.1}$$

where V_{in} is the converter input voltage and V_{out} the voltage at the output of the converter. After a time T_{on}, SW1 is opened and SW2 is closed. This Off-State prevails during the time T_{off} (Fig. 5.2). Now the voltage drop across the inductor is:

$$V_L = -V_{out}. \tag{5.2}$$

The evolution of the inductor current I_L can be calculated with the inductance L and the law of induction:

$$V_L = -L\frac{dI_L}{dt}. \tag{5.3}$$

Including 5.1 and 5.2 this yields after integration over one period:

$$\frac{V_{in} - V_{out}}{L}T_{on} - \frac{V_{out}T_{off}}{L} = 0, \tag{5.4}$$

From this the output voltage can be calculated:

$$V_{out} = \frac{T_{on}}{T_{on} + T_{off}}V_{in} = \frac{T_{on}}{T}V_{in} = fT_{on}V_{in} = DV_{in}, \tag{5.5}$$

where the period T, the frequency f and the duty cycle D have been introduced.

It has to be noted that the step from 5.3 to 5.4 implies that the current I_L remains larger than zero. If this condition is fullfilled the converter is operated in the so-called continuous mode.

The in- and output voltages of DC-DC converters are usually flattened by capacitors (C_{in} and C_{out}). Due to the finite capacitance and the equivalent series resistance (ESR) of the capacitors, some fluctuations always remain [36]. The output noise $\delta_{out,C}$ due the finite capacitance is given by:

$$\delta_{out,C} = \frac{V_{in} - V_{out}}{8f^2LC_{out}}\frac{V_{out}}{V_{in}}, \tag{5.6}$$

while the input noise $\delta_{in,C}$ can be described by:

$$\delta_{in,C} = \begin{cases} \frac{I_{out}V_{out}(V_{in}-V_{out})}{fC_{in}V_{in}^2}, & ,A < 1 \\ \frac{1}{8L}\frac{V_{in}-V_{out}}{C_{in}V_{in}^2}\left(2LI_{out} + \frac{V_{out}}{f}\right)^2 & ,A > 1 \end{cases} \tag{5.7}$$

where A is:

$$A \equiv \frac{V_{out}^2}{2fLV_{in}I_{out} - \frac{V_{out}}{V_{in}}(V_{in} - V_{out})}. \tag{5.8}$$

The output noise due to the ESR $\delta_{out,ESR}$ is given by:

$$\delta_{out,ESR} = R_{C_{out}}^{ESR}\frac{V_{in} - V_{out}}{fL}\frac{V_{out}}{V_{in}}, \tag{5.9}$$

and the intput ESR noise $\delta_{in,ESR}$ is:

$$\delta_{in,ESR} = R_{C_{in}}^{ESR}\left(I_{out} + \frac{V_{in} - V_{out}}{2fL}\frac{V_{out}}{V_{in}}\right). \tag{5.10}$$

Since the different noise sources are not in phase, they cannot be directly added. Furthermore it has to be noted that all equations given here are based on the following assumptions:

- The converter is operated in continuous mode.
- The load on the output is a constant DC load.
- The converter is 100% efficient (no switching losses etc.).

A conclusion from 5.6-5.10 could be to increase the switching frequency as far as possible to reduce the noise, but higher frequency also imply more switching losses and hence decreases the efficiency.

Due to the harsh SLHC environment and the special requirements of CMS it will be necessary to develop a custom converter. This is challenging, since the final device will have to withstand more than 750 kGy [37] in the inner regions of the strip tracker. In addition, it should provide a high efficiency and a noise spectrum as quiet as possible. Due to the 4 T magnetic field of CMS, only air-core based inductors can be used. They require more space than inductors with ferrite-cores and tend to radiate electromagnetic noise.

5.1.2 Commercial Buck Converters

The studies described here have been performed with commercial buck converters from Enpirion and Micrel: the EN5312QI [38], the EQ5382D [39] and the MIC3385 [40]. These devices have been chosen becuase of their good noise performance and their high efficiencies. Furthermore they can provide the voltages and current required by the tracker modules. Still they cannot be used in the final CMS detector, since they are not radiation hard. In addition the EN5312QI and the MIC3385 make use of ferrite-core inductors.

The EN5312QI is operated at a switching frequency of 4 MHz, enabling the use of very small internal components. The device includes a planar, ferrite inductor and the switching logic. It measures 5 mm × 4 mm × 1.1 mm in size. Provided on-chip features are: under-voltage lock-out (UVLO), over-current protection, short circuit protection and thermal overload protection. Figure 5.3 shows the converter's layout as a block diagram. The only additionally required components, as recommended by Enpirion, are a 4.7 µF capacitor on the V_{in} line and a 10 µF capacitor on the output. A X-ray photograph of the converter chip can be seen in Fig. 5.5, while Fig. 5.4 shows a typical implementation of the converter chip.

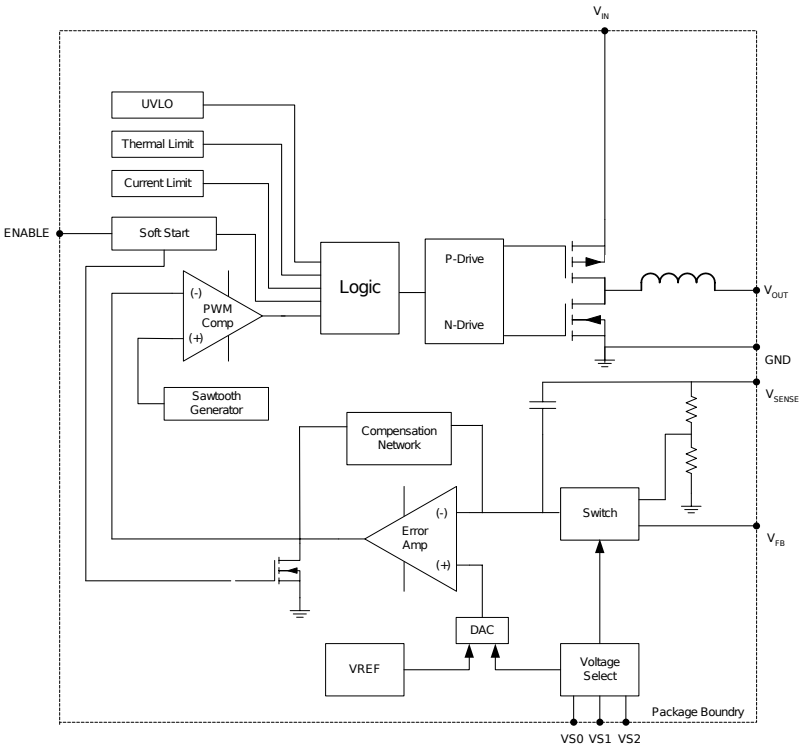

Figure 5.3: Functional block diagram of the EN5312QI [38].

Recommended input voltages range from 2.4 V up to 5.5 V (stress ratings: -0.3 V – 7.0 V). One of seven possible output voltages, including the 1.25 V and 2.5 V required by the CMS front-end electronics, can be chosen via a three pin voltage select scheme. In addition, an external divider option enables the selection of any voltage in the range from 0.6 V to (V_{in}-0.6 V). A continuous output current of up to 1000 mA is feasible.

Enpirion advertises the EN5312QI to be optimised for low noise and low EMI applications, with a ripple voltage of typically 5 mV peak to peak. The efficiency for three different input voltages and an output voltage of 2.5 V is plotted as a function of the load current in Fig. 5.6. The maximum achievable efficiency is quoted to be 95%.

The EQ5382D is basically the same converter chip as the EN5312QI. The main difference is the lack of an internal inductor. Therefore the EQ5382D is slightly smaller (2 mm × 3 mm × 0.9 mm) and requires an additional, external inductor. Enpirion recommends an inductance value of 1 µH. Lower values are also feasible. A typical implementation of the END5382D is show in Fig. 5.7.

For this study two different commercial, external inductors have been used: one inductor by muRata (LQH32CN1R0M23) [41] with a ferrite-core, providing 1.0 µH, and one by Coilcraft (132-20SM_L) [42] with an inductance of 538 nH. Both are shown in Fig. 5.8.

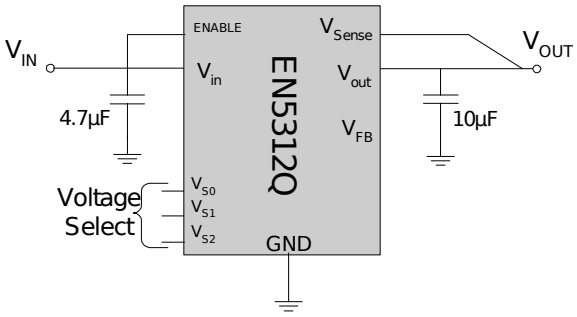

Figure 5.4: Typical application circuit featuring the EN5312QI [38].

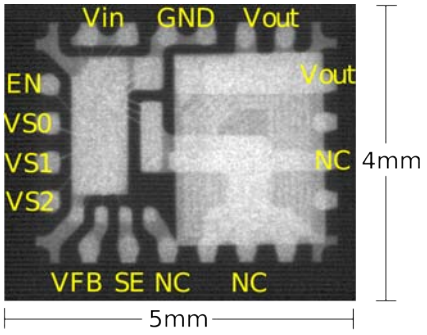

Figure 5.5: X-ray photograph of the EN5312QI.

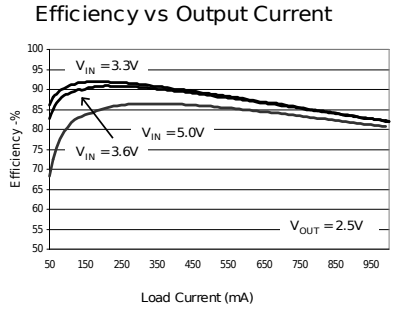

Figure 5.6: Efficiency of the EN5312QI as a function of the output current [38].

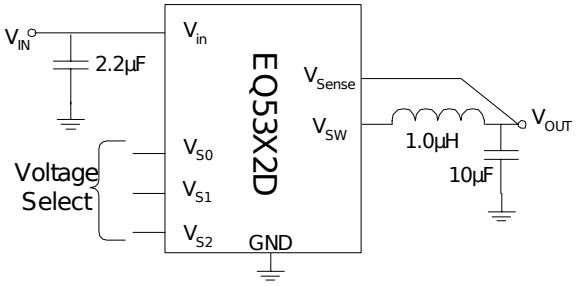

Figure 5.7: Typical application circuit featuring the EQ5382D [39].

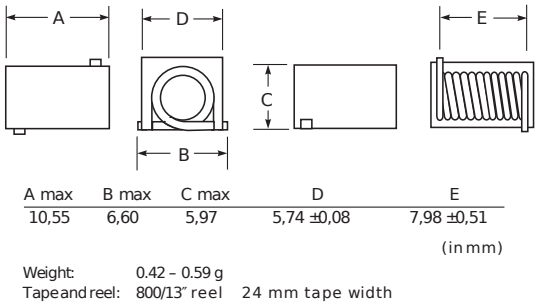

(a) The Coilcraft 132-20SM_L.

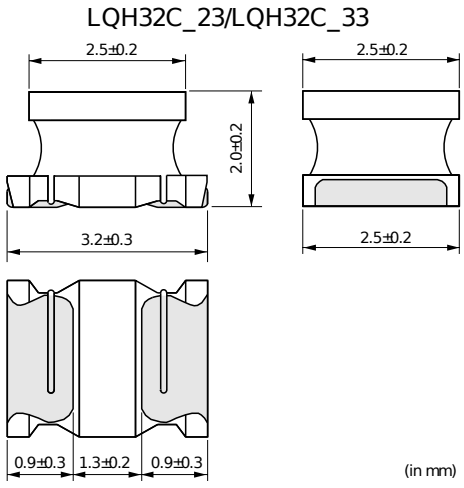

(b) The muRata LQH32CN1R0M23.

Figure 5.8: Mechanical drawings of the commercial inductors used for this study.

The MIC3385 is another converter chip with an internal ferrite-core inductor. Two important differences between this device and the EN5312QI are the switching frequency, which is 8 MHz in case of the MIC3385, and the smaller footprint of the MIC3385 of 3 mm × 3.5 mm × 0.9 mm. The remaining design parameters and integrated functionalities are similar to those of the EN5312QI. The block diagram of the MIC3385 is given in Fig. 5.9.

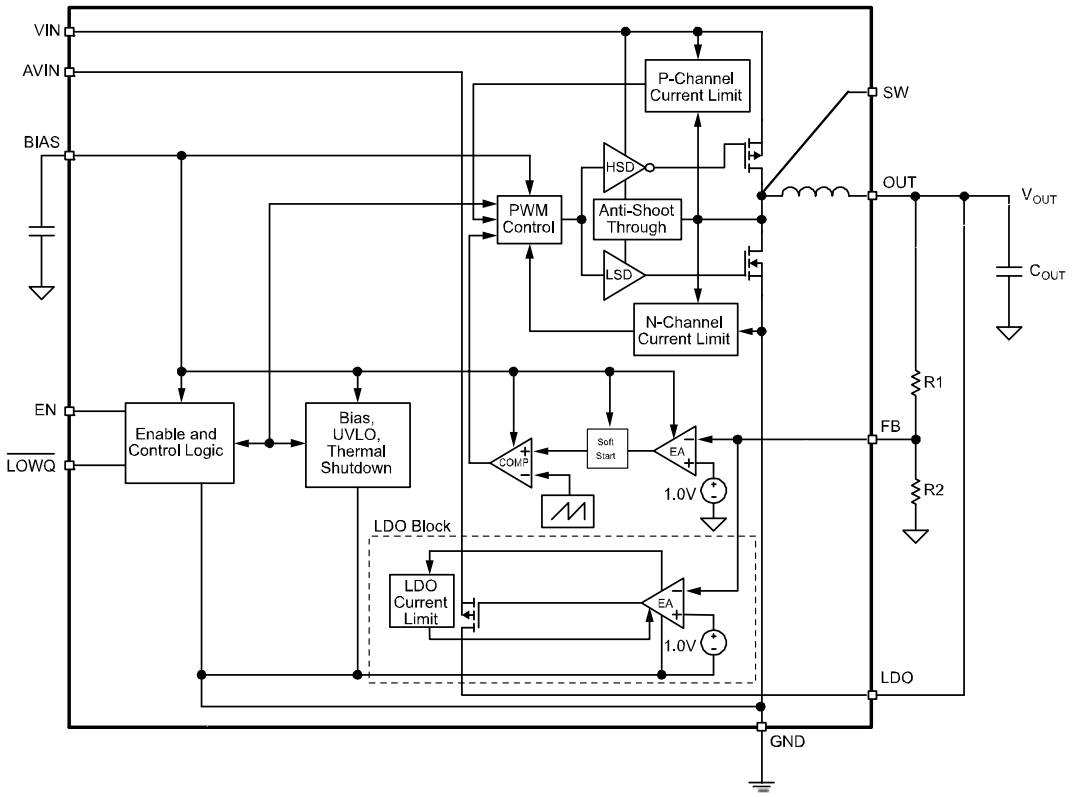

Figure 5.9: Functional block diagram of the MIC3385 [40].

A comparison of all three converters which have been used in this work, is given in Table 5.1.

	EN5312QI	EQ5382D	MIC3385
Input voltage [V]	2.4 – 5.5	2.4 – 5.5	2.7 – 5.5
Max. current [mA]	1000	800	600
Operating frequency [MHz]	4	4	8
Max. efficiency [%]	95	96	90
Internal inductor [µH]	1	–	0.47
Size [mm×mm×mm]	5 × 4 × 1.1	2 × 3 × 0.9	3 × 3.5 × 0.9

Table 5.1: Comparison of the three commercial buck converters used for this work.

5.1.3 The Charge Pump

A charge pump [34, 35, 43] is a DC-DC converter which uses capacitors (instead of an inductor) as energy storage elements. In commercial applications, these switched capacitor circuits are mostly used to increase voltages at low currents (e.g. in displays). Step-down devices are rare, as they can cope only with rather small currents (e.g. compared to buck converters). Typically they do not provide conversion ratios larger than 4. A radiation hard commercial devices is not yet available.

Charge pumps are operated, like buck converters, in two phases. During the first phase the capacitors are charged. In the second phase the accumulated charges are transferred to the output of the converter. The

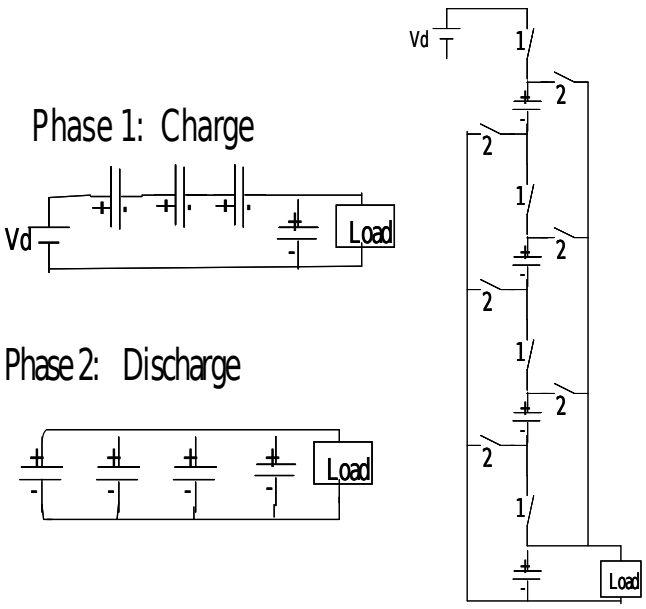

Figure 5.10: Left: The two phases of an operating charge pump. In phase 1 the capacitors are charged. In phase 2 the accumulated charges are transferred to the output. Right: Circuit diagram of a charge pump [43].

conversion ratio is related to the number of capacitors. Figure 5.10 shows both phases and the according circuit diagram.

The major advantage of charge pump converters, with regard to an implementation into CMS, is the fact that they require no inductor. Hence they radiate significantly less noise than inductor-based converters with air-core inductors. A radiation hard charge pump, providing low noise, a high efficiency and sufficiently high currents has still to be developed.

5.1.4 Low DropOut Regulators

Linear regulators are step down converters which convert a given voltage into a lower one by dissipating the difference between the input and the output voltage (dropout voltage) into heat. To provide a constant output, linear regulators are equipped with feedback circuits that re-adjust their resistance.

Due to their good noise performance, linear regulators are also used to assure a constant voltage level by dissipating fluctuations into heat. So-called Low DropOut regulators (LDO) allow to remove small fluctuations, while their low dropout ensures a rather good efficiency.

5.1.5 Potential integration into CMS

Figure 5.11 shows a possible layout of a converter-based powering scheme. It assumes future read-out electronics to be operated at 1.2 V and proposes a conversion in two stages. Within the TEC the first stage could e.g. be installed on petal level. A second converter could be mounted on each module together with the front-end electronics. The modules would be powered in parallel. This scheme allows to provide several different voltages via one cable. In addition, the converters could replace the present sensing system. The currents which have to be supplied depend on the number of modules per petal and the number of chips per module.

For the present system, without DC-DC converters, the power loss P_{cable} within these cables is given by:

$$P_{cable} = V_{cable} I_0 = R_{cable} I_0^2, \tag{5.11}$$

where V_{cable} is the voltage drop across the cables and R_{cable} their resistance. The current I_0 is determined by the power P_d and voltage V_d required by the detector:

$$I_0 = \frac{P_d}{V_d}. \tag{5.12}$$

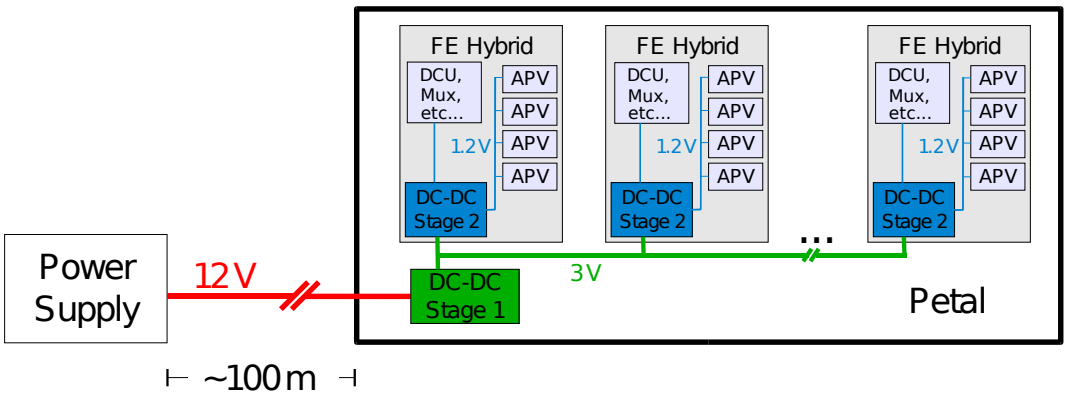

Figure 5.11: Potential tracker powering scheme, based on DC-DC conversion. The voltage is converted in two stages.

Hence for fixed detector Power P_d, P_{cable} is proportional to V_d^{-2}:

$$P_{cable} = R_{cable} \left(\frac{P_d}{V_d} \right)^2 . \tag{5.13}$$

The usage of DC-DC converters with a conversion ratio $r = V_{out}/V_{in}$ would allow to supply $V_{in} = V_d/r$, instead of V_d. Due to 5.13, this would reduce P_{cable} by a factor of $1/r^2$.

To compare the amount of power P_{con} which has to be supplied in a conventional scheme with the power P_{DC} that has to be delievered if DC-DC converters are used, one has to consider the converter's efficiency η as well. In a conventional scheme, P_{con} is given by:

$$P_{con} = P_d + P_{cable}, \tag{5.14}$$

while the usage of DC-DC converters would lead to:

$$P_{DC} = \frac{P_d}{\eta} + \left(\frac{r}{\eta} \right)^2 P_{cable}, \tag{5.15}$$

The present strip tracker has a power consumption of approximately 60 kW, of which about 50% are lost within cables [22]. If a convesion ratio of $r = 1/10$ and an efficiency of $\eta = 80\%$ is assumed, Equation 5.15 leads to a total power consumption of about 38 kW. The power losses are reduced by a factor of 3.75.

A major challenge towards a powering scheme based on DC-DC conversion is to build a converter which withstands the SLHC conditions and meets the requirements of CMS. One of the main advantages of DC-DC conversion is its flexibility.

5.2 Serial Powering of Silicon Modules

Powering sensor modules in series is an alternative approach to reduce power losses and the material budget of experiments like CMS [44]. Like DC-DC conversion, serial powering is based on the idea of increasing the voltage and thus decreasing the currents within the feed cables. This is achieved by powering several modules in series, since the voltage drop across n modules equals n-times the voltage drop of a single module. So a n-times higher voltage can be supplied. Each single module has its own ground potential. The number of serially powered modules corresponds to the conversion ratio of a DC-DC converter in the corresponding scheme. Figure 5.12 compares two possible schemes based on serial powering and DC-DC conversion. To avoid the loss of all connected modules in case of a defect of a single module a so-called shunt regulator is connected in parallel to each module[1]. These devices are comparable to Zener diodes and ensure a constant voltage drop across the module. In the case of a module failure, the corresponding current is routed through the regulator and converted into heat. In the same way current fluctuations are compensated. If needed, an additional linear regulator can be used to tune the output voltage of the shunt regulator, or to provide a second, lower voltage.

[1] Another possibility would be to integrate a shunt regulator into each readout chip.

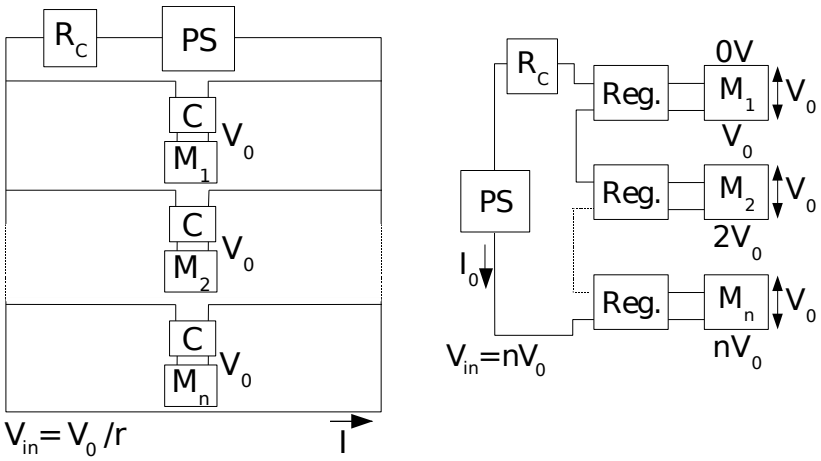

Figure 5.12: Comparison of DC-DC conversion and serial powering. Left: The modules are powered in parallel by DC-DC converters. The converters reduce the input voltage V_{in} down to $V_0 = rV_{in}$ required by the modules. Right: The power supply in the serial powering scheme has to deliver a constant current. The correct voltage drop through the modules is ensured by shunt and linear regulators. R_C is the resitance of the cables.

One of the advantages of serial powering is the fact that it does neither require an inductor, nor a switching network. This reduces the probability to inject additional noise into the system. Furthermore only one cable is needed to power n daisy-chained modules. However, serial powering rises challenges as well:

- The design of the front-end electronics is closely connected to the powering scheme.
- The effect of noise pick-up within a large system has to be studied. However, tests by the ATLAS collaboration with small systems have shown encouraging results [45].
- The modules must not be directly coupled to each other or to the outer world, due to their different ground potentials.
- The power supplies have to provide a constant current, which is converted into heat if it is not required by the electronics. Hence the power consumption is always higher than the max. required one. The cooling capacity has to be designed accordingly. This might become an issue for devices with significantly higher peak power consumptions, such as optical links.
- Supplying different voltages leads either to additional cables or higher thermal losses within the detector.

Chapter 6

The System Test Set-Up

The measurements presented in this document were performed in an air-conditioned clean room. The system test set-up, shown in Fig. 6.1, resembles a small-scale version of the CMS tracker data acquisition system. It is based on a TEC front petal instrumented with four prototype[1] ring 6 modules. For the measurements the official CMS DAQ software was used. The control and readout chains consist of CMS prototype components. A schematic block diagram of the set-up is shown in Fig. 6.2.

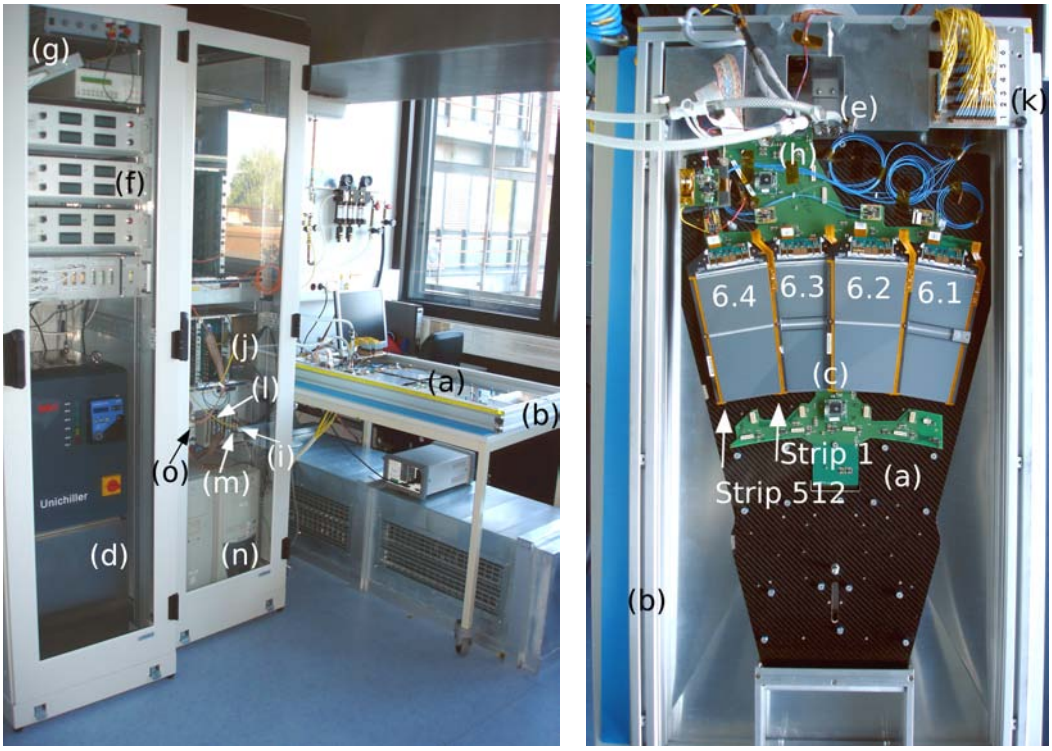

(a) Set-up in the clean room.

(b) The front petal.

Figure 6.1: Photograph of the test set-up in the clean room. The two racks in the foreground house the readout and service equipment. The petal box is opened. The photograph to the right shows the front petal with the four mounted ring 6 modules. The labels are explained in the text.

The front petal (a) is mounted in a closed and grounded metal box (b). Unavoidable openings in the patch-panel region have been covered by a dense curtain to achieve the required low light level. Active cooling for the silicon modules (c) is provided by a standard chiller of type ICO12 by Huber (d) [46]. It is connected to the cooling manifolds (e) of the petal via elastic hoses. The temperature of the coolant (C_6F_{14}) is kept constant around 15°C.

[1]The design of these prototypes is already final. The final modules are only improved in terms of reliability.

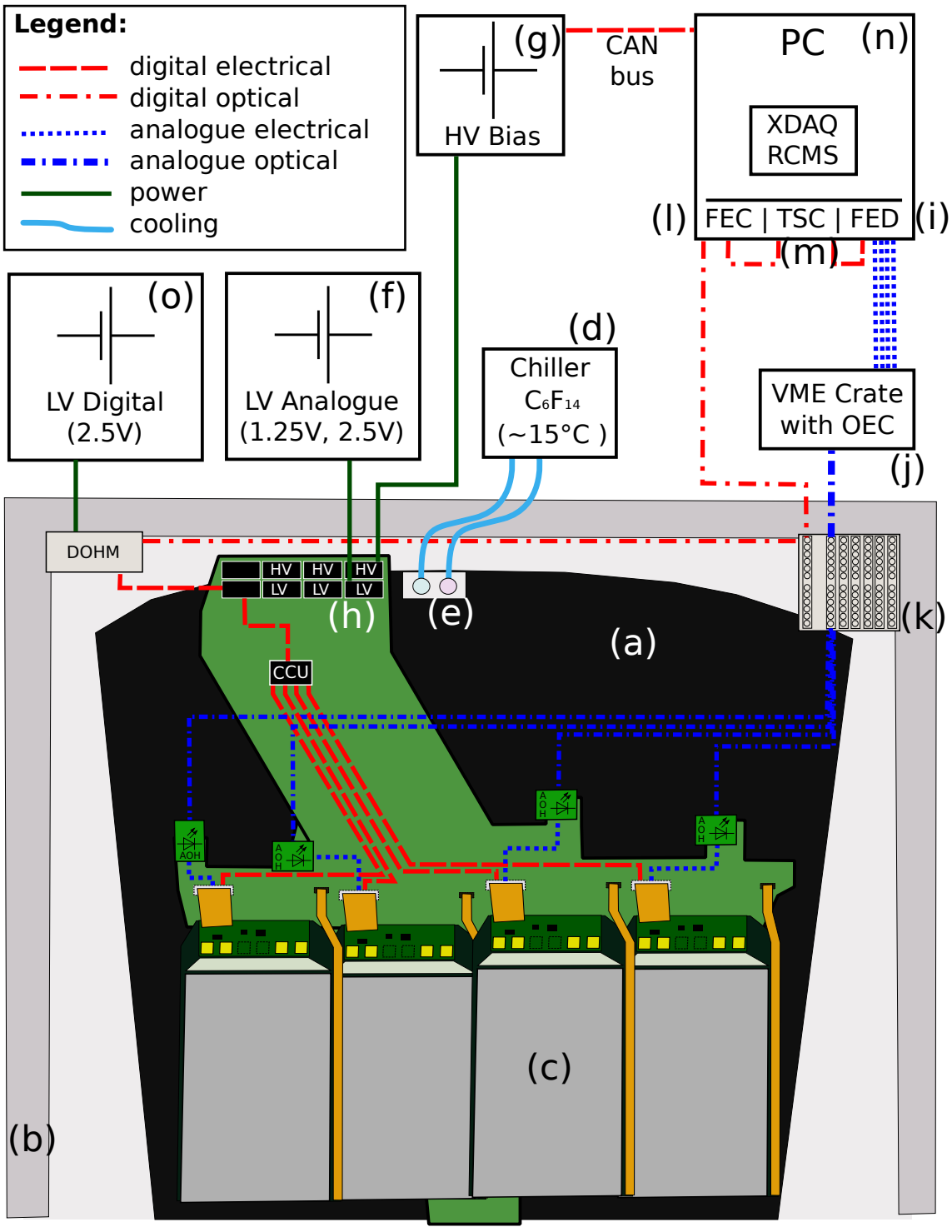

Figure 6.2: Schematic view of the system test set-up.

The operation voltage for the frontend devices is provided by a so-called "Delphi" power supply (f). This unit was assembled from parts recuperated from the LEP experiment DELPHI for use in CMS tracker test facilities (e.g. petal and rod long term tests). It is a floating power supply providing 1.25 V and 2.5 V DC and can correct the voltage drop occurring in the cables via sense wires that measure the voltage on the ICB.

The bias voltage (typically 250 V) for the modules is provided by an EHQ 8210p-F (g) [47] high voltage power supply from iseg, which is controlled via a CAN bus [48] interface. One of the eight independently programmable output channels of the EHQ 8210p-F is split into four lines, one per module. At the back of the Delphi power supply, all HV and LV lines of a power group are brought together to a prototype multi-service cable of 10 m length. This cable is used to connect the power supply to the petal. It has a FM36W4 D-sub connector at both ends and hence requires an additional transition cable for the connection to the Molex connectors on the ICB (h).

For the module readout, a PCI bus prototype version of the FED, a so-called FED-PMC (i), is used. Since this readout card only has electrical inputs, an opto-electrical converter (OEC) (j) is used to convert the signals coming from the AOHs into analogue electrical data. Another difference with respect to a standard FED is the 9-bit resolution of the ADC, compared to the 10-bit ADC of the VME FEDs.

The connection between the petal and the opto-electrical converters is established by a 10 m long rubber-coated ribbon, which contains 12 fibres. The ribbon has an MPO connector at the OEC-side and a MU-terminated fanout, which is plugged into a 12-way MU-MU adapter (k), at the petal side. A second ribbon is used for transmitting the digital link signals. The MU-MU adapters of both ribbons are combined into a patch panel which is fastened to the petal box.

The digital link is controlled via an optical FEC card (l) mounted on a PCI mezzanine board. A 40 MHz clock and the trigger signals are provided by a trigger sequencer card (TSC) (m) [49]. The TSC is a PCI card that has been constructed for the use in CMS test stations where it replaces the LHC clock and CMS trigger. The clock and trigger signals are distributed from the TSC to the FEDs and the FEC. One TSC has four electrical and one optical output which is sufficient for small systems with one FEC (connected optically) and up to four FED-PMCs.

The PMC FED, the PMC FEC, and the TSC are housed in a PCI extender connected to a standard PC (n). Furthermore, this PC contains a Kvaser PCIcan [50] CAN bus card to communicate with the HV power supply. All DAQ, run control and data analysis software is executed on this PC. Concerning noise studies, an important property of the given set-up is the absence of a direct electrical connection between the PC and the petal.

The 2.5 V, required by the front-end devices of the digital link (mainly CCUMs and the DOH), are provided by a dedicated floating power supply unit (o).

6.1 Integration of the Buck Converters

The commercial buck converters EN5312QI, EQ5382D and MIC3385 have been integrated via custom PCBs, designed by Waclaw Karpinski and Irfan Özen. Each PCB carries two identical converters to provide 1.25 V and 2.5 V, hence only one converter PCB per module is required. In addition every PCB carries two NAiS connectors, one on the top and one on the bottom side. Via these connectors the PCB is plugged between the ICB and the respective module.

Due to geometrical constrains and for test purposes, seven different PCB layouts have been design. In total 15 different PCB types, differing in layout and components, have been assembled. A photograph of the standard converter PCB, the so-called L type can be seen in Fig. 6.3. The according layout and the schematics are shown in Fig. 6.4 and Fig. 6.5, respectively. During the characterisation process, the PCB was connected to a constant load of 0.7 A per converter chip and a ripple voltage of about 10 mV peak to peak has been observed [51].

Geometrical constrains on position 6.1 of the petal led to the PCB layout shown in Fig. 6.6. It features a modular design, composed of a main PCB which is slightly smaller than the standard PCB, and an additional bridge PCB providing the NAiS connectors. The main PCB, which is plugged onto the bridge, is similar to the standard PCB. The differences can be seen in the schematics and the layout in Appendix A.1. Within this document the smaller and modular PCB is referred to as the S type.

The converters are powered by an Agilent E3634A power supply [52]. They are either directly connected to the power supply or via the 1.25 V plane of the ICB. The latter implies the use of a modified transition

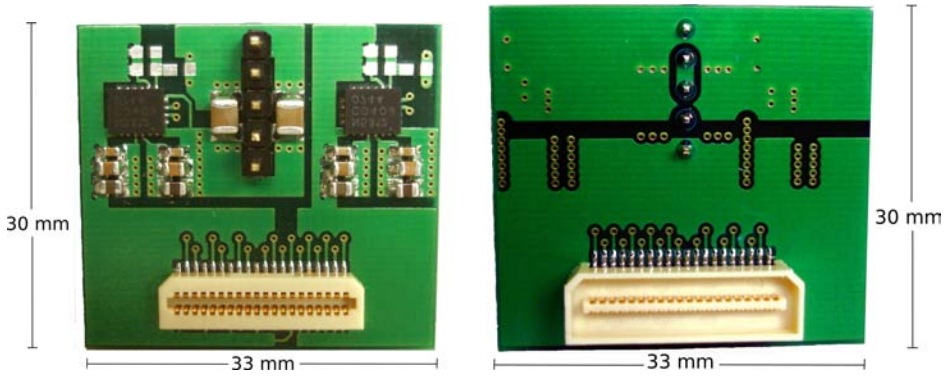

(a) Top side. (b) Bottom side.

Figure 6.3: Photograph of the L type converter PCB.

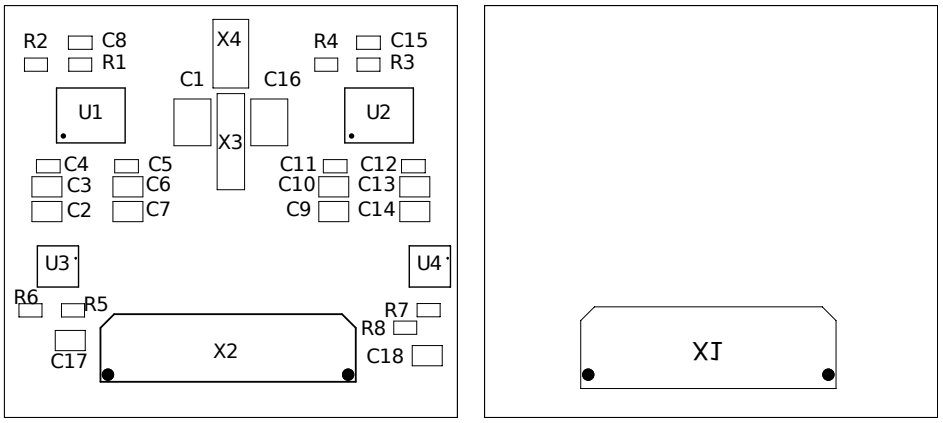

(a) Top side. (b) Bottom side.

Figure 6.4: Layout of the L type converter PCB.

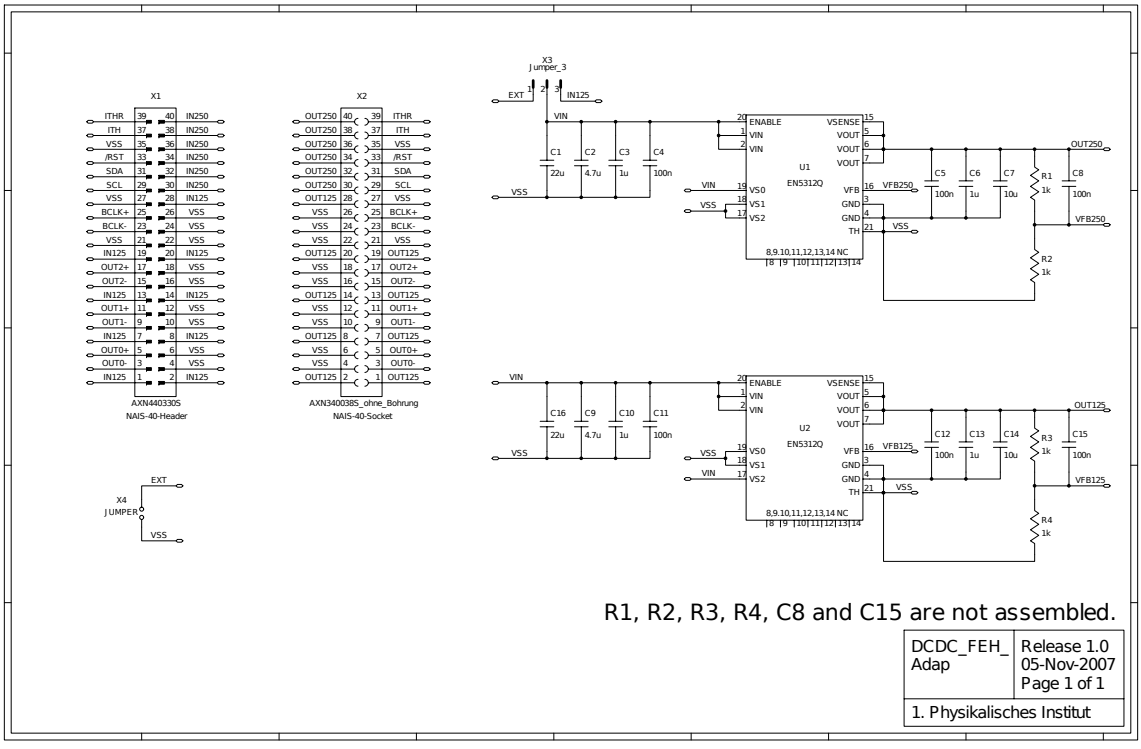

Figure 6.5: Schematics the L type converter PCB.

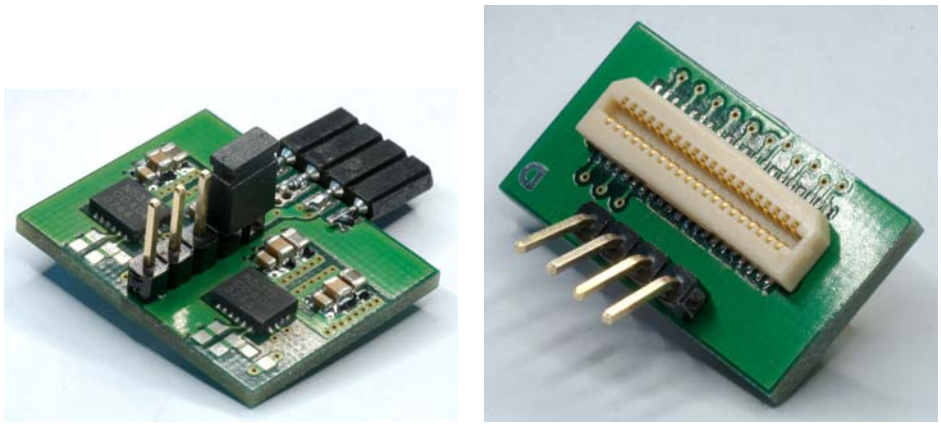

(a) Main PCB. (b) Bridge PCB.

Figure 6.6: Photograph of the S type converter PCB.

cable, which connects the Agilent power supply to the 1.25 V input connector of the ICB. This is possible since 1.25 V is used only by the APV, all other components on the petal are powered from 2.5 V. The ICB method avoids any additional cables crossing the petal and is more similar to the real tracker. On the other hand, the direct connection allows to power the modules independently with or without converter. This offers for example the possibility to study crosstalk effects. In which way the converters are powered is set by a jumper on their PCBs. Figure 6.7 shows how a converter PCB is integrated into the system, depending on the connection method. Unless stated otherwise, for measurements presented in this work, the power was provided directly to the converters. The supplied input voltage was 5.5 V.

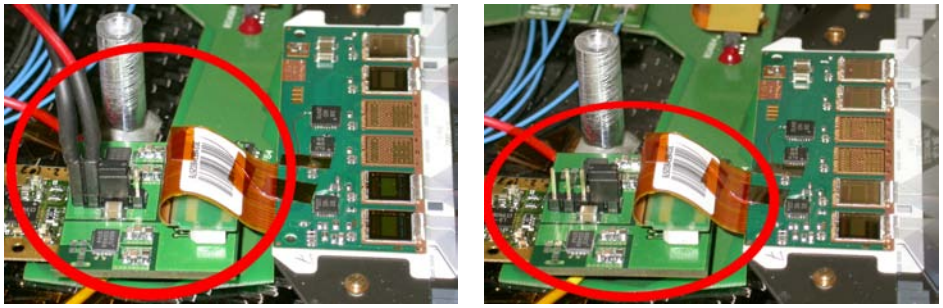

(a) Powered externally. (b) Powered via the ICB.

Figure 6.7: Photograph of a L board plugged onto the ICB.

6.2 The Data Acquisition Software

The data acquisition (DAQ) [53] system of the tracker is implemented by a set of applications, organised as plug-ins of an extendable server program, the so-called XDAQ (Cross-Platform Data Acquisition) framework [54]. The hardware of the set-up, namely the FED, the FEC and the TSC, is controlled by the dedicated supervisor applications.Within the used XDAQ version, these applications are configured via XML files. Additional applications implement trigger-related tasks (TriggerSupervisor), collect data from the FEDSupervisors (ReadoutUnits), build the events (EventBuilder), perform online analysis and write the data to disc (RootAnalyzer). The TrackerSupervisor application provides an overall control instance for the DAQ applications. The DAQ version (RC1205) used for the studies presented in this document grands access to the supervisor application through a web-based user interface utilising the so-called HyperDAQ [55].

To find the correct and optimal settings of the front-end devices and readout cards, the DAQ software offers several commissioning runs [53]:

The Connection Scan loops over all laserdrivers in the set-up and switches them on individually. One trigger is sent for each laser, while all FEDs are read out. Thus the FED input connected to the currently active laser is determined and a mapping of all connections is generated.

The Timing Run adjusts delays related to cables and fibres, to ensure that all FEDs sample the APV frames simultaneously. During this run, the FEDs simply digitises the signal arriving at their input. Simultaneously, the delay time of the arrival of the tick marks at the FEDs is increased in steps of 25/24 ns by changing the fine-delay in the register of the PLL. This allows to deduce the optimal sampling points of the FEDs, and to synchronise the system.

The Gain Scan adjusts the bias current and gain of the lasers of the AOH. To find the optimal current, the complete range of possible values is scanned while the signals corresponding to the logical low and logical high of the APV are recorded. Then the logical low signals received by the FED are subtracted from logical high ones. Plotting the resulting values with respect to the bias current leads to a curve that rises as long as only the locigal high signal causes an optical signal. Once the logical low causes a signal too, the curve starts to form a plateau which continues until the optical receiver of the FED starts to saturate. Since this happens first for the locigal high value, the curve falls until the signal of the low value equals the high one. The optimal bias is given by the current values forming the plateau because they allow to exploit the full dynamic range of the read-out system. To minimise the power consumption of the AOH, the value at the beginning of the plateau is used.

The VPSP Scan places the baseline level of the analogue signal at one third of distance between the digital low and digital high level of the APV. This is achieved by measuring the baseline level for all values of the VPSP register. The value at one third of the dynamic range is chosen, to ensure its optimal utilisation.

For this work, these commissioning runs were performed before the first data were recorded and after every major modification of the set-up. Unless stated otherwise, the actual data were recorded in so-called pedestal runs and in peak mode. In pedestal runs data are sampled as in physics runs, however the trigger is not synchronised with any particle signal.

6.3 The Analysis Software

The raw data recorded by the DAQ software need further treatment before meaningful results can be obtained. This task has been fulfilled by the analysis software "AC1Analysis" [6], which was also used during the TEC integration in Aachen. For the studies presented here, the code originally written by Richard Bremer has been changed slightly and was equipped with a few new methods.

6.3.1 Pedestal and Noise

In each event, the signals of two APVs are multiplexed onto a single data line and fed through an optical fibre into the FED, where they are digitised. The received data are saved in root [56] files by the DAQ software. These files contain one histogram per FED channel for each recorded event. The corresponding raw data consist of the two 12 bit digital headers of the APV data and the ADC values of the 256 strips that have been multiplexed into the data channel (3.2.2). Due to the multiplexing, the channel ordering is mixed up and has to be re-established by the analysis software. The physical strip number s is computed from the position n in the analogue data block according to Equation 6.1:

$$s = 32 \cdot ((n/2) mod 4) + 8 \cdot int\left(\frac{n/2}{4}\right) - 31 \cdot int\left(\frac{n/2}{16}\right) + 128\left(\frac{n}{2} mod 2\right), \tag{6.1}$$

where "int" denotes an integer division and n is an element of $1, 2, \ldots, 256$.

Determination of the Pedestal
The data of each detector strip fluctuates about a constant offset position, the so-called pedestal. The pedestal p_i of strip i is calculated from a large number N of events as the mean value of the raw data r_i of this channel:

$$p_i = \frac{1}{N}\sum_{e=1}^{N} r_{i,e} \tag{6.2}$$

For the measurements presented in this document, the pedestal has been adjusted once by the VPSP register of the APV25 chip to about the middle of the range of the FED's ADC.

Noise Calculation The raw noise σ_i^{raw} of a strip i is calculated as the standard deviation of the signal $r_{i,e}$ of the strip:

$$\sigma_i^{raw} = \sqrt{\frac{1}{N-1}\sum_{e=1}^{N}(r_{i,e} - p_i)^2}. \tag{6.3}$$

The raw noise contains the following contributions:

- Intrinsic noise of the detector and the readout electronics
- Noise generated during digitisation, depending on the dynamic range of the analogue digital converter
- Common mode noise

The common mode corresponds to a common deviation of a range of detector channels from their pedestal value in a single event e. A typical sources of common mode is e.g. the noise of power supplies, or external disturbances such as radiation from other electronic devices in the vicinity of the set-up. Within this work the chosen range corresponds to an APV (128 channels). If the common mode is assumed to be the same for all channels in this range it can be calculated as the mean deviation, averaged over the given channels, from the pedestal. The analysis software also offers the option to calculate the CM as the median deviation. Unless stated otherwise, the common within this work is calculated as the median. Thus the impact of noisy and open strips is minimised.

In a data sample the common mode CM_e is computed for each event and can be subtracted from the signal of all channels of an APV. The RMS of the resulting data is called **noise after common mode subtraction** or **common mode subtracted noise**. It is given by:

$$\sigma_i = \sqrt{\langle (r_i - p_i - CM)^2 \rangle - \langle r_i - p_i - CM \rangle^2} \tag{6.4}$$

where $\langle \dots \rangle$ indicates the average over the given event range.

The common mode subtracted noise can be regarded as a measure of the irreducible noise of the electronics. Physics studies of data recorded by the CMS tracker are based on common mode subtracted data. The RMS of the common mode of a channel is called common mode noise and indicates the influence of external devices on the detector module.

The common mode could also depend linearly on the strip number. In this case for each event a strait line is fitted to the pedestal subtracted raw data of all channels in the chosen range. The resulting linear function can be subtracted from the data.

Concerning a tracker upgrade for the SLHC, it is possible (or even likely) that a digital read-out scheme will be chosen and that such a common mode subtraction will be impossible.

6.3.2 Bad Strips

Silicon strip detectors can have defects affecting one or more channels. These defects arise e.g. from broken bonds, shortcuts between two neighbouring channels, or pinholes. Pinholes are small holes in the isolating SiO_2/Si_3N_4 layer between the p^+ implants and the aluminium strips of the sensor. They can cause the destruction of the capacitive coupling between the p^+ layer and the aluminium strips. Additionally, there may be defects in the front-end electronics leading to unusual behaviour of the detector module.

These defects will not be discussed in detail here, but it should be noted that they can affect the performance of single strips of a module significantly. Affected strips are called bad strips or bad channels. They can be recognised from their noise, which is either significantly higher ("noisy channel") or lower ("open channel") than the noise of the rest of the module.

Bad strips are ignored during the computation of the common mode, as they would adulterate the result. The analysis code identifies a strip as noisy, if the noise of the strip is greater than the mean noise σ_{APV} of the APV channels plus 5 times the RMS of the noise of the channels of the APV:

$$\sigma_i > \sigma_{APV} + 5RMS_{APV} \tag{6.5}$$

Accordingly a strip is flagged as open, if its noise is smaller than the mean noise of the APV channels minus 5 times the RMS of the noise of the channels of the APV:

$$\sigma_i < \sigma_{APV} - 5RMS_{APV} \tag{6.6}$$

To compute the mean and RMS of the noise of an APV, only strips that have not been flagged as bad strips are used. This allows for iteratively improving the strip flagging.

6.3.3 Strip & APV Correlations

For this work the analysis software has been instrumented with a method to calculate the correlations between single strips. The resulting correlation matrix ($corr_{ij}$) can be calculated for several modules. The correlation between the raw data r_i and r_j of two strips i, j is given by:

$$corr_{ij} = \frac{\langle r_i r_j \rangle - \langle r_i \rangle \langle r_j \rangle}{\sigma_i \sigma_j}, \tag{6.7}$$

where σ_i and σ_j are the noise values of the corresponding strips. The notation $\langle \dots \rangle$ indicates the average over a given number of events.

Furthermore it is possible to calculate the correlation between the CM of two APVs. The corresponding formula for the two APVs I and J is given by:

$$corr_{IJ} = \frac{\langle CM_I CM_J \rangle - \langle CM_I \rangle \langle CM_J \rangle}{\sigma_I \sigma_J} \tag{6.8}$$

where CM_I and CM_J are the mean CMs of the APVs (averaged over their strips) and σ_I, σ_J represent the common mode noise. Again, the notation $\langle \dots \rangle$ indicates the average over a given number of events.

For the implementation of 6.8, the averaging over the events has been decoupled from the averaging over the channels. This spares working memory and allows to calculate the correlation matrices of large structures such as a TEC sector.

Chapter 7

System Test Measurements with Commercial DC-DC Converters

7.1 General System Performance

The results of a typical measurement without DC-DC converters are shown in Figs. 7.1, 7.2 and 7.3. Data recorded in peak and deconvolution mode are compared. The amount of noise in deconvolution mode is increased, as expected. The results are comparable to data recorded during the integration of the TEC+ [6]. This applies also to the increased noise on the border between two adjacent APVs.

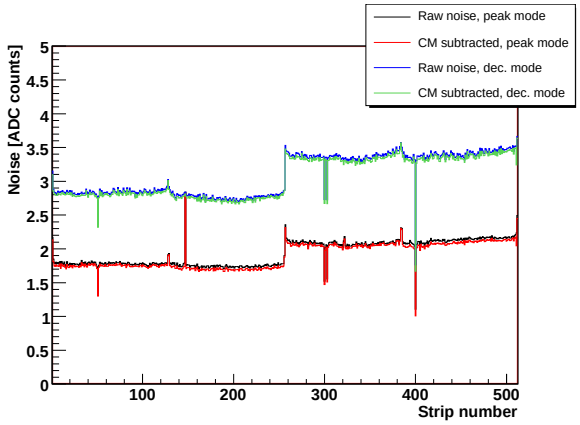

Figure 7.1: Noise of module 6.4, powered without converter. Shown are the raw noise recorded in peak (black) and deconvolution mode (blue), as well as the CM subtracted noise in peak (red) and deconvolution mode (green).

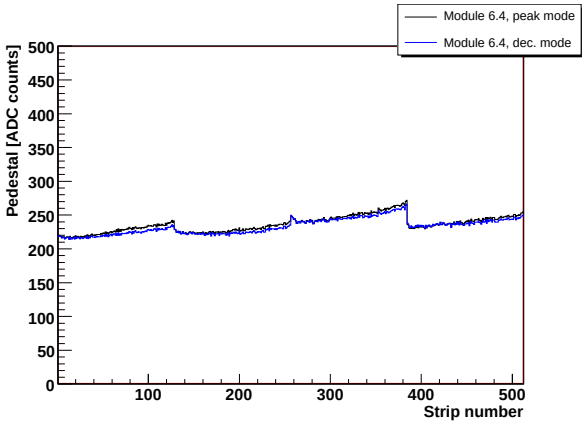

Figure 7.2: Pedestal of module 6.4 in peak (black) and deconvolution (blue) mode, powered without converter.

In order to exclude effects from thermal drifts in the system the noise, pedestals and correlations shown in this document are computed from 10 000 events, starting with the 90 000$^{\text{th}}$ event of each run. Fig. 7.4 shows the deviation from the pedestal for a single strip as a function of the event number. The system is at thermal equilibrium after approximately 80 000 events.

Figure 7.5 shows the correlation matrix of the raw data of module 6.4. In general the channels are only slightly correlated (below 10%). The channels of APV2 and APV 4 are stronger correlated among each other than with channels of the adjacent APVs. The channels of APV1 and APV3 are in general less correlated. Figure 7.6 zooms into the section of Fig. 7.5 which corresponds to the channels at the border between APV1 and APV2. The last strip of APV1 (strip 128) and the first strip of APV2 (strip 129) are anti-correlated by approximately -35%. This effect can be observed on all border channels of adjacent APVs. It is discussed in detail in Section 7.2.2. In addition, the secondary diagonal, corresponding to adjacent channels is anti-correlated by about -20%. The latter effect has already been observed in 2003 by C. Civinini [57] in tests with TIB modules.

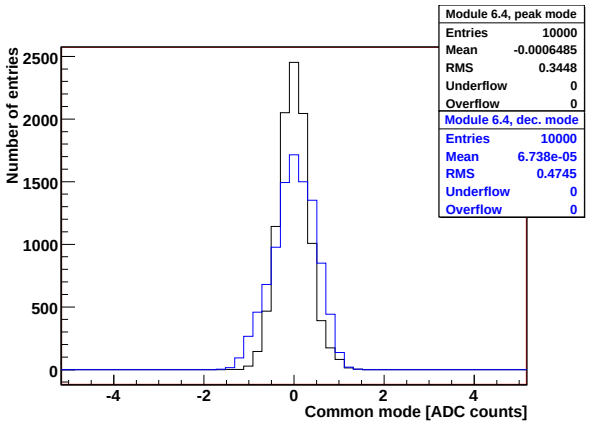

Figure 7.3: Common mode distribution of the second APV of module 6.4, recorded in peak (black) and deconvolution (blue) mode.

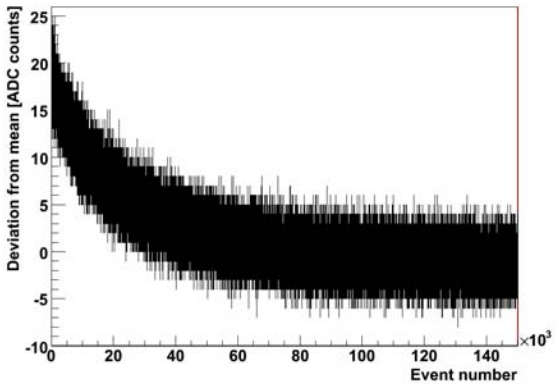

Figure 7.4: Deviation of the signal of a single strip from the pedestal as a function of the event number.

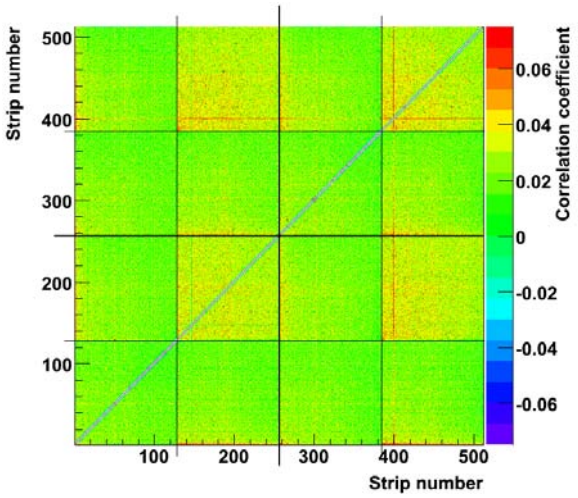

Figure 7.5: Correlation matrix of the raw data of module 6.4. The black lines separate the APVs, the thick lines the two optical channels of the module.

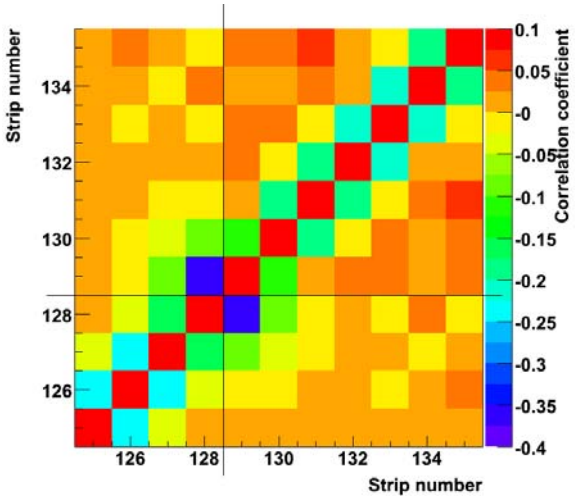

Figure 7.6: Correlation matrix of the raw data of module 6.4 for the channels at the border between APV1 and APV2.

To determine if an alternating pattern of the correlations of even and odd APVs is also visible in a larger system, data from the TEC+ integration [6] have been analysed. Figures 7.7 and 7.8 show the APV correlation matrix of TEC Sector 7 and the correlations between the APVs on ring 6 of a front petal, respectively. The alternating pattern is visible. It indicates that a part of the CM is generated after the multi-plexing step, because the APVMUXs process the even and odd channels at the same time, respectively.

The fact that the APVs are correlated throughout the sector by around 70% to 90% does not imply that the channels of the individual APVs are correlated on such a high level. Only the averaged APV data are correlated. In other words, the common mode which affects the APVs is a global phenomenon throughout the sector.

With regard to this work it is important to note that the test set-up behaves like the final CMS components during integration.

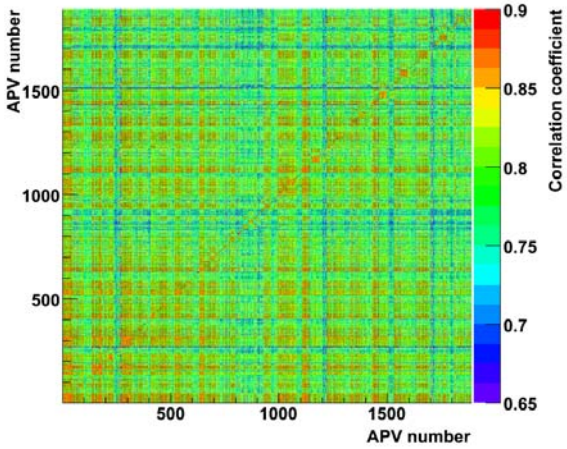

Figure 7.7: Correlation matrix of the APVs of Sector 7 from the TEC+.

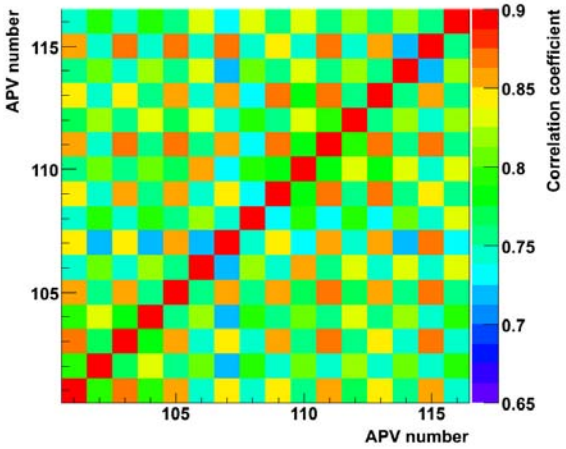

Figure 7.8: Correlations among the APVs of ring 6 on a front petal of TEC+ Sector 7. The chequerboard pattern is clearly visible.

7.2 Buck Converters with Internal Ferrite Core Inductors

7.2.1 General Noise Performance with Converters

Powering with L type PCBs (S type on 6.1) causes a slight increase of the module noise. Figure 7.9 shows the raw noise of the four modules in the set-up. Both in peak and deconvolution mode the converter PCBs increase the overall level of the noise by approximately 5% to 20%.

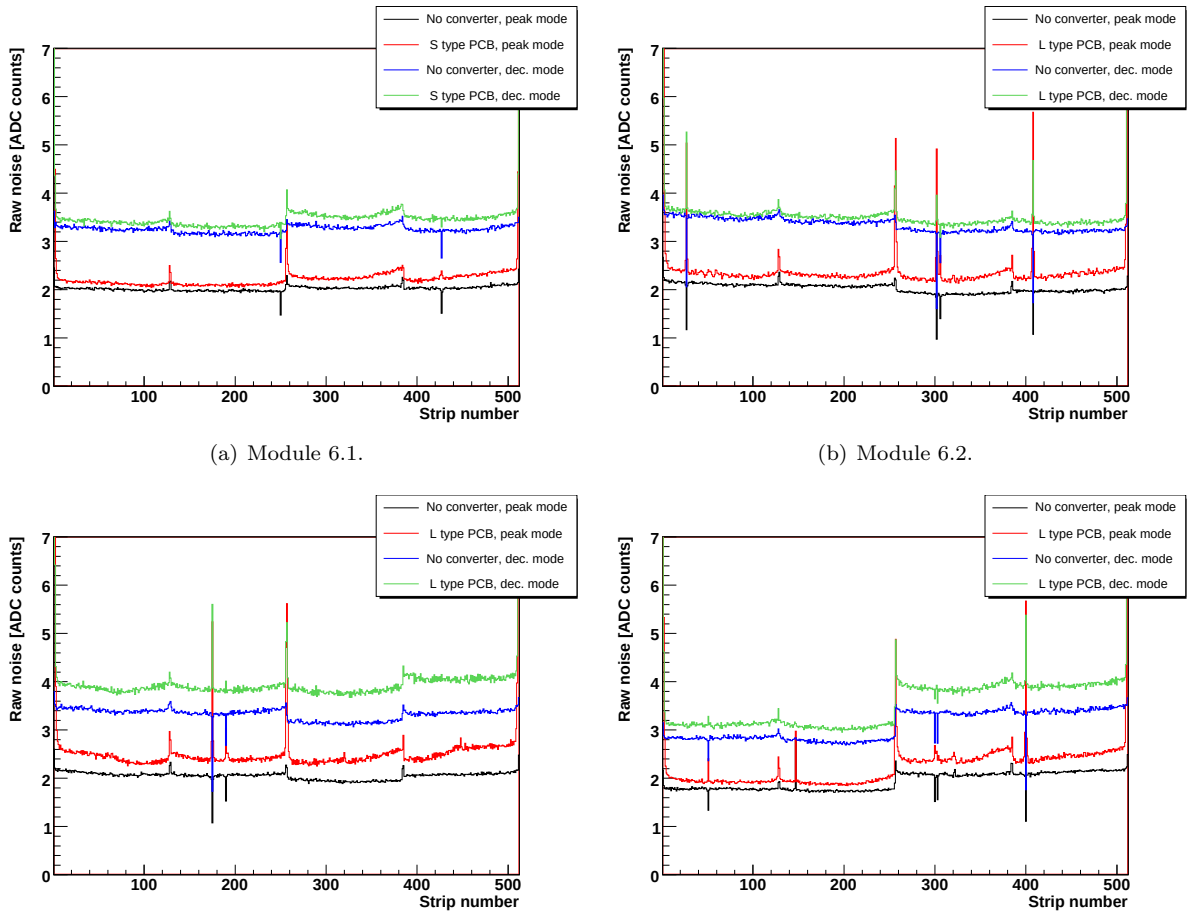

(a) Module 6.1.

(b) Module 6.2.

(c) Module 6.3.

(d) Module 6.4.

Figure 7.9: Raw noise of all four modules: noise without converter recorded in peak (black) and deconvolution mode (blue), as well as the noise with converter in peak (red) and deconvolution mode (green). Channel 512 of module 6.1 is next to channel 1 of module 6.2 and so on.

The additional noise is dominated by common mode. This can be seen from the broader CM distribution in Fig. 7.10 and the correlation matrix in Fig. 7.11. Compared to Fig. 7.5, the correlations among channels of the module increase drastically and reach up to 40%.

Due to its common origin, the additional noise can be removed almost completely by the CM subtraction of the analysis software (Fig. 7.12). The best result is achieved if a linear relation between the CM and the channel numbers is assumed. It has to be pointed out that the CM subtraction requires an analogue read out, which is unlikely to be implemented in a future tracker.

7.2.2 Influence of the Front-End Electronics

The influence of the present front-end electronics has to be understood, to interpret the measurements with DC-DC converters correctly. Only then meaningful conclusions concerning a future system can be drawn.

According to Fig. 7.9 the noise with converter is not increased uniformly. Instead it increases drastically on the edge strips of the module, as well as on adjacent strips on the border between the inner APVs. Figure 7.13 shows that the noise of the module edge strips is increased by a factor of more than 10. On

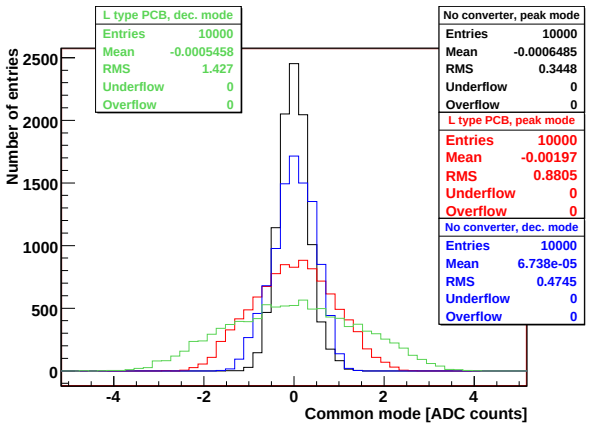

Figure 7.10: CM distribution of the second APV of module 6.4. A broader distribution corresponds to a higher CM. The data recorded with conventional powering, in peak and deconvolution mode are shown as black and the blue histograms, respectively. In red and green are measurements are shown which have been recorded in peak and deconvolution, respectively. During both runs the module was powered with the L type PCB.

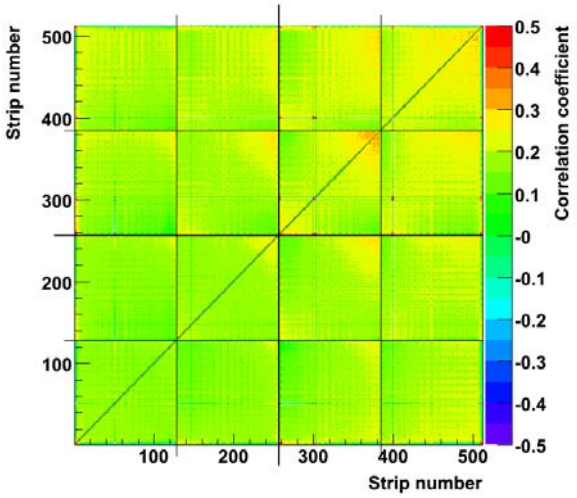

Figure 7.11: Correlation matrix of module 6.4, powered by an L type PCB (peak mode).

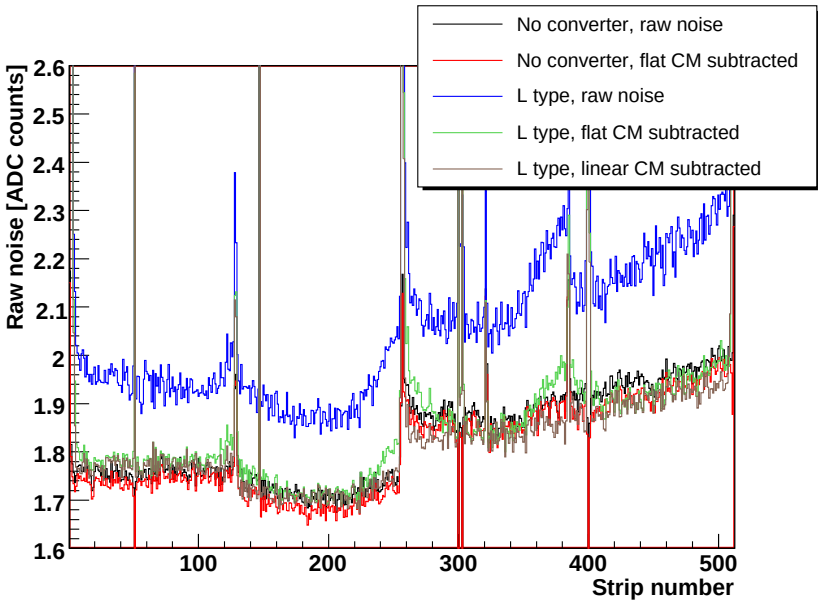

Figure 7.12: Raw and CM subtracted noise of module 6.4 recorded in peak mode. The raw noise is shown in black and blue for measurements powered conventionally and with the L board, respectively. The noise after the subtraction of a flat CM is shown in red and green for conventional powering and converter based-powering, respectively. The noise shown in brown corresponds to a measurement with L type, after subtracting a linear CM.

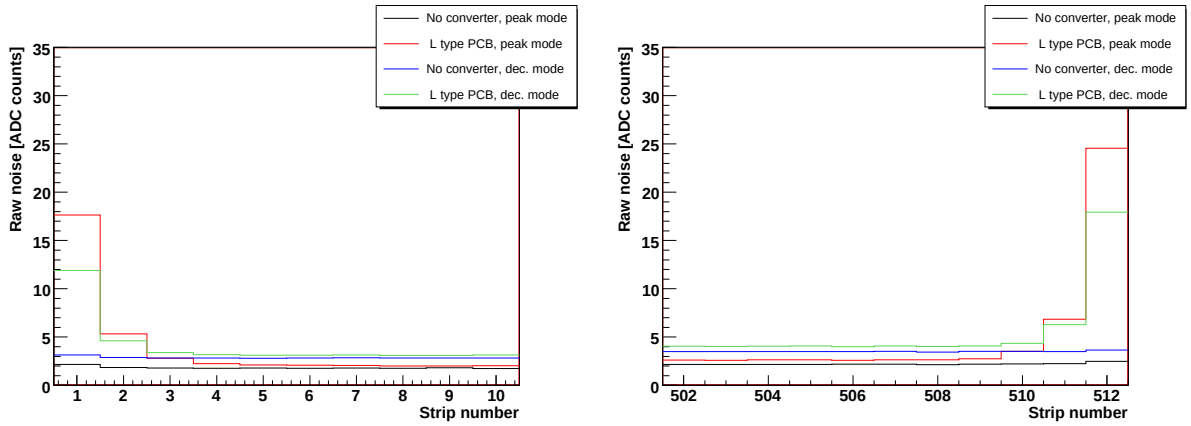

(a) First strips of the module.

(b) Last strips of the module.

Figure 7.13: Noise of the edge strips of module 6.4. Plotted is the noise without converter recorded in peak (black) and deconvolution (blue) mode, as well as the noise with converter in peak (red) and deconvolution (green) mode.

open channels the noise is not simply increased but turns from a low to a high value. An example for this is strip 400 in Fig. 7.9(d).

The correlations among module edge strips, open strips and adjacent strips of two neighbouring APVs are distinctive as well. Figures 7.14 and 7.15 show the corresponding sections of the correlation matrix and reveal the following facts, which are discussed subsequently:

- The correlation among the module edge strips rises from approximately 10% without converter to almost 100% if the L type PCB is used (Fig. 7.14(a)).
- Without converter, module edge strips and open strips show no conspicuous correlations. If the L type PCB is used, they tend to be anti-correlated, down to -85% (Fig. 7.14(b)).
- The converter correlates the open strips positively among each other (Fig. 7.14(c)).
- Between APV1 and APV2, as well as between APV3 and APV4, the anti-correlation is slightly decreased due to the converter (Fig. 7.15(a)).
- Between APV2 and APV3 the anti-correlation is increased (Fig. 7.15(b)).
- Using the L type leads either to a correlation or to an anti-correlation between the module edge strips and the strips between two adjacent APVs (Fig. 7.15(c)).

Noise of APV Edge Channels

A dedicated test was performed to determine the reason for the increased noise of the APV edge channels. The intention was to check if the noise originates from the front-end electronics, or if it is caused by a capacitive coupling between the silicon strips. The latter was suspected to cause a current flow between the affected preamplifiers, initiated e.g. by fluctuations of the reference voltage of the APVs.

Therefore, the last but one silicon strip (127) of the first APV was connected to the last channel of the this APV (128) and vice versa. The same procedure was repeated with the first two channels and strips of the second APV, corresponding to channel 129 and 130. The result of this test can be seen in Fig. 7.16. The increased noise is not related to the APV channel, which is adjacent to the next APV, but to the corresponding silicon strip. This confirms the theory based on capacitive coupling.

After presenting this result to M. Raymond, he proposed that fluctuations of 1.25 V between the different APVs could be responsible for the effect. The schematic in Fig. 7.17 shows a simplified model of the sensor capacitance network connected to the charge preamplifier inputs in the boundary region between two read-out chips. Only four channels of each chip are shown; the bottom four (1-4) of chip 1, and the top four (125-128) of chip 2. The capacitors C_{BP} represent the sensor strip capacitance to the sensor back plane V_{BIAS}, which is irrelevant for the effect to be described here.

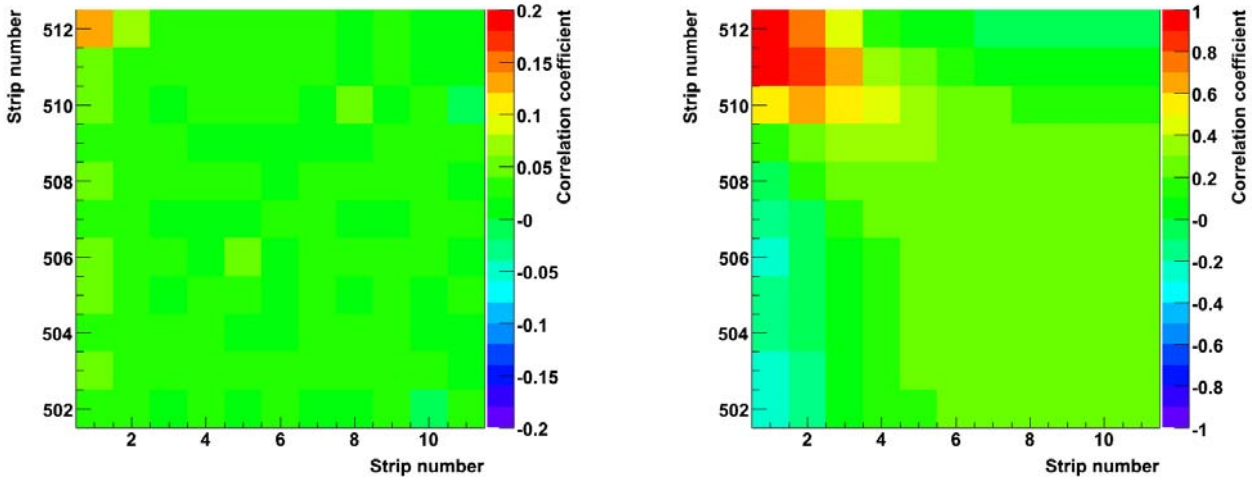

(a) Correlations among the module edge strips (1 and 512).

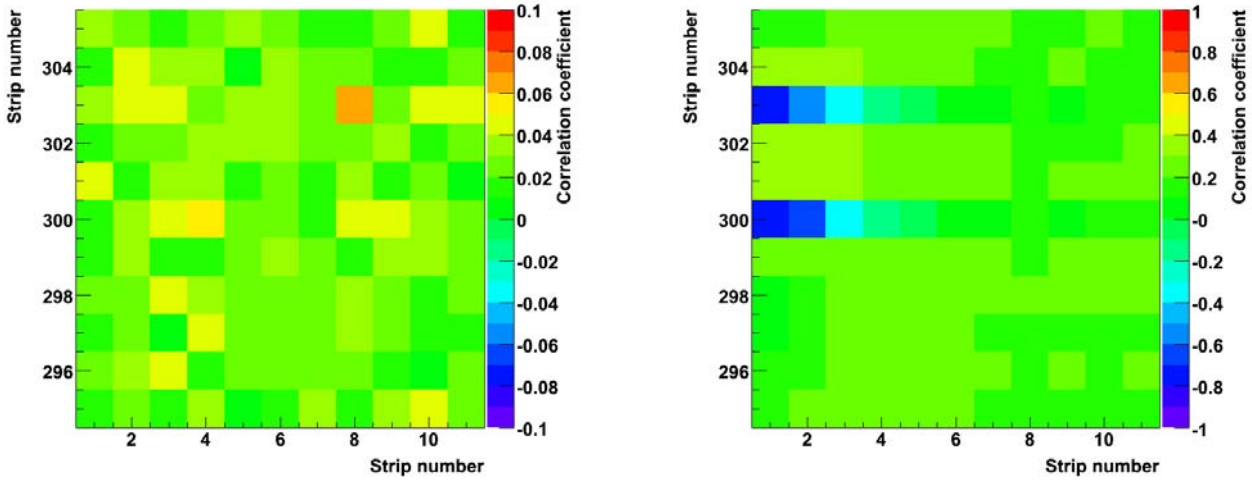

(b) Correlations between the first strip of the module and two open strips (300, 302).

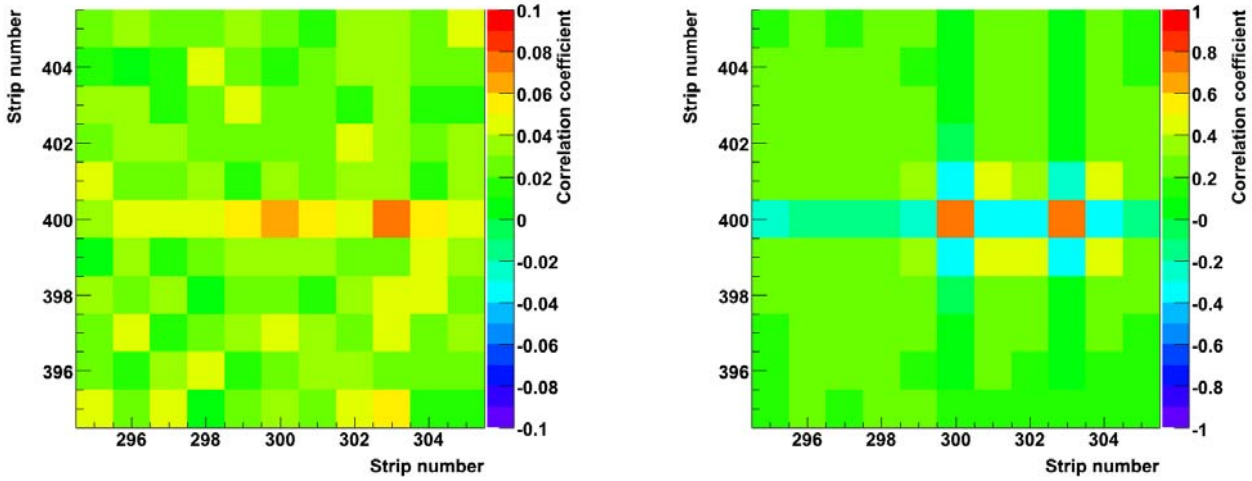

(c) Correlations among three open strips (300, 302 and 400).

Figure 7.14: Correlations of edge and open strips. The plots on the left side correspond to a measurement without converter. The plots on the right side show the results obtained with the L type PCB. Note the different colour scalings.

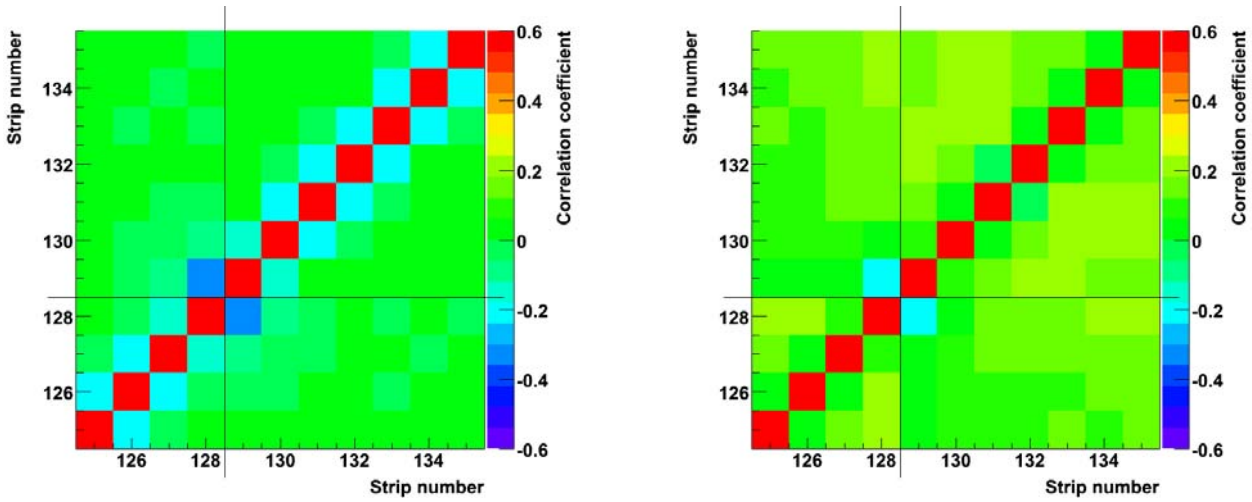

(a) Correlations of the strips (128, 129) on the boarder between APV1 and APV2.

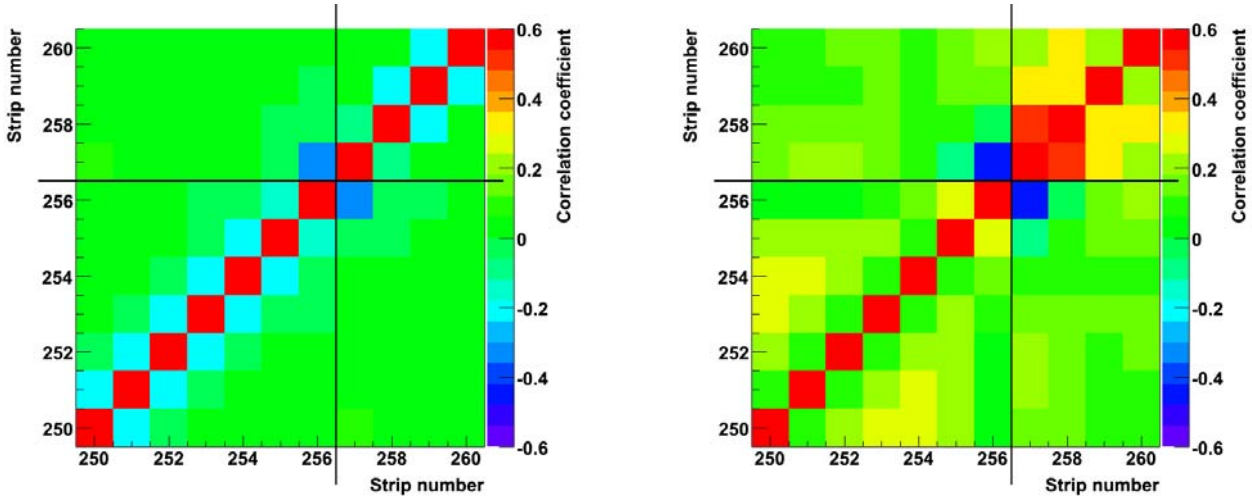

(b) Correlations of the strips (256, 257) on the boarder between APV2 and APV3.

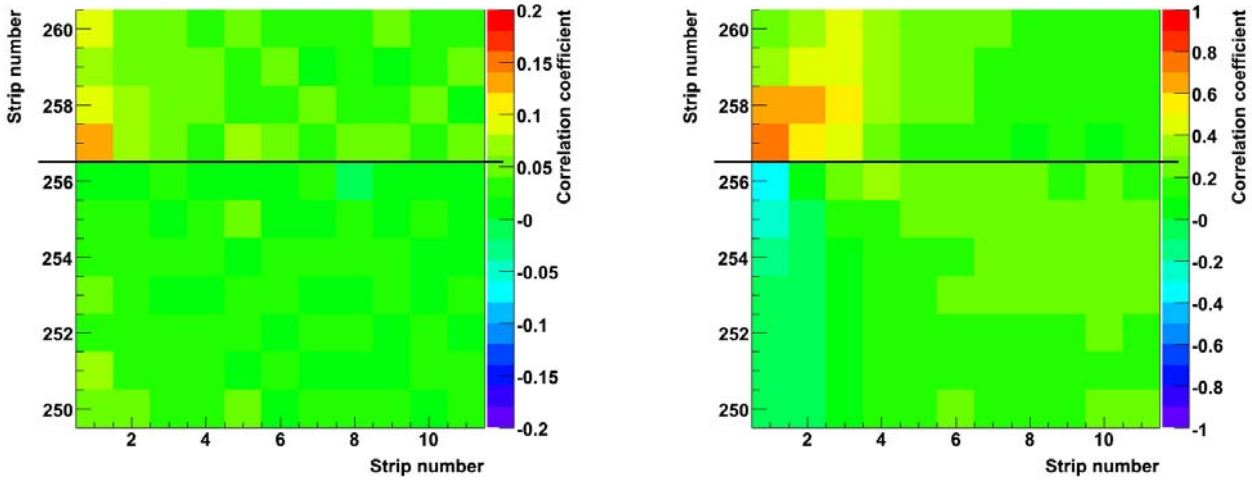

(c) Correlations between the first strip of the module (1) and the strips between APV2 and APV3 (256, 257).

Figure 7.15: Correlations of the module edge strips and adjacent strips of neighbouring APVs. The plots on the left side correspond to a measurement without converter. The plots on the right side show the results obtained with the L type PCB. Note the different colour scalings.

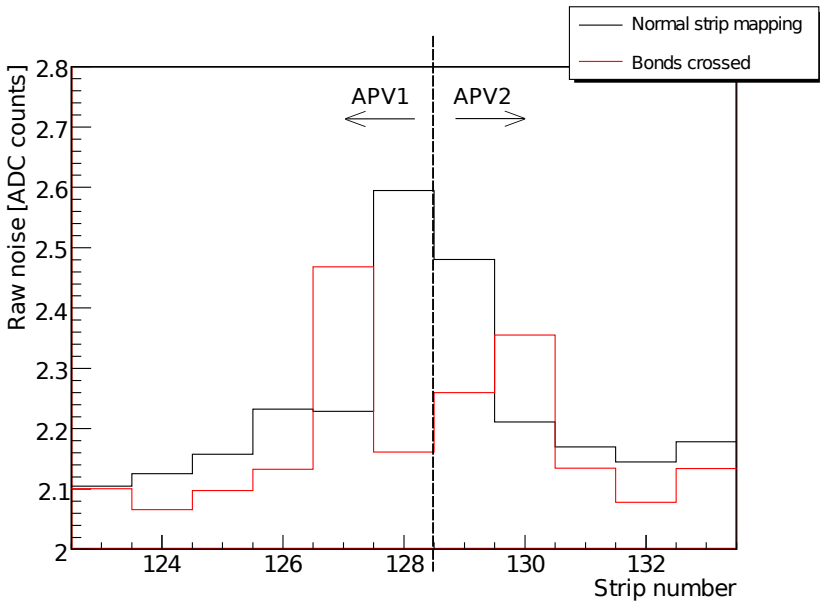

Figure 7.16: Noise of the strips on the border between the first two APVs (module 6.2). In black a reference measurement is shown. For the measurement shown in red, the bonds connecting the pitch adapter and the APV channels 127, 128 and 129, 130 have been crossed, respectively.

The preamplifiers of each chip are shown referenced to a supply reference on the chip, gnd_1 for chip 1, gnd_2 for chip 2. For the APV gnd_1 and gnd_2 correspond to the 1.25 V seen by the respective chip (Fig 7.18). In an ideal system these two voltages would be identical, but if for example gnd_1 were to change by a voltage ΔV, then all the preamplifier input and output quiescent voltages would change by the same amount. The green waveforms in the schematic show the effect of a step change in gnd_1 on the input and outputs of the preamplifiers in chip 1, which will all show the same step change. For all the channels, with the exception of the edge channels, this is a common mode effect which is removed within the chips.

For the edge channels of the chip the effect is different, but only if the preamplifier reference voltage of the neighbouring chip does not see the same disturbance. If gnd_2 remains unchanged then the preamplifier input voltages V_{IN128}, V_{IN127}, V_{IN126}, ... are also unchanged. This leads to a transient current, represented by the red arrows in the figure, through the interstrip capacitance C_{1-128} that couples the edge channels between the two chips.

For the polarity of the voltage step on gnd_1, the current will flow out of chip 1/channel 1 into chip 2/channel 128 and the outputs of the preamplifiers connected to those channel will show the anti-correlated step responses shown in blue; positive for chip 1, negative for chip 2. (Note that V_{O1} would also have a small contribution from the original disturbance on gnd_1, which is present on all the other channels on chip 1.)

This effect could only happen for edge channels of the chips. For channels within a chip the input voltages on either side of the interstrip capacitance change by the same amount (in response to a change in the preamplifier's reference voltage), so there is no current flow.

A typical value for the interstrip capacitance of a strip tracker module is $\sim$ 15 pF. Hence a step voltage disturbance of 1 mV on gnd_1 with respect to gnd_2 would cause a positive charge injection of 15 fC into channel 128 of chip 2, and a correlated negative charge injection of -15 fC into channel 1 of chip 1 (for the APV a minimum ionising particles corresponds to 4 fC [3]). Even though a difference of as much as 1 mV is unlikely because gnd_1 and gnd_2 are connected together on the 1.25 V plane on the hybrid, these huge signals indicate that the magnitudes of the voltage differences need only to be small to give rise to significant disturbances in these edge channels. This is due to the relatively large interstrip capacitances. Another important aspect is the design of the 1.25 V hybrid layer, shown in Fig. 7.19. The locations of the bond pads, which are used to connect the APVs to this layer are indicated by red dots. Apparently the worst direct connection is established between APV2 and APV3. This would explain the sensitivity of the corresponding channels to the noise of the DC-DC converters. Judging from the recorded noise, the connections between the remaining APVs seem to be good enough to suppress the influence of the converter.

Their anti-correlations are even slightly compensated by the higher global CM introduced by the converters.

Noise of Module Edge Channels
The high noise of the module edge channels and their correlation seem to be related to a capacitive coupling between the edge strips and the bias ring (Fig. 3.3). The capacitance C between the edge strips and the bias ring is in the order of 10 pF [5]. The switching frequency f of the used DC-DC converters is 4 MHz. This leads to an impedance of:

$$|Z| = \left| \frac{1}{2i\pi fC} \right| \sim 10^4 \Omega, \tag{7.1}$$

which is two order of magnitudes smaller than the 1.5 MΩ ohmic resistance between the bias ring and each strip. The bias ring is AC-coupled via 100 nF to the ground potential of the hybrid, while the preamplifiers are referenced to 1.25 V (Fig 7.18). Hence alternating currents can flow from the capacitance between the edge strip and the bias ring into the preamplifier of the edge channel, and vice versa. To determine if the high and positively correlated noise of the edge channels is really caused by this phenomenon, the bias ring of module 6.2 has been AC-coupled to 1.25 V instead of the ground potential. This was intended to cause the bias ring and the preamplifiers' references to move together and thus cancel out the edge noise. Figure 7.20 shows the connection of the bias ring before and during the test. The result shown in Fig. 7.21 confirms the described idea. After the manipulation of the bias ring, the last channel behaves like a channel in the middle of the APV. The noise on the first channel is reduced by a factor of 3. As expected, the noise of the other channels is not affected.

Behaviour of Open Strips
An explanation why the noise of open strips turns from low to high could be the on-chip CM subtraction of the APV (Sec. 3.2.3). It subtracts the CM noise from all channels including open strips, even if the CM does not affect them as much as it affects normal channels. As a result, the open strips do not show their normal noise, but the part of the subtracted CM which originally did not affect them. An indication for this theory is the anti-correlation between edge and open strips (Fig. 7.14). If an event is recorded while the CM is rather high, the signal of the edge strips is also increased. At the same time, a higher value is subtracted from the signals of the open strips resulting in a lower value. Hence the open strips are correlated among each other and anti-correlated with the edge strips.

7.2.3 Supplying 1.25 V and 2.5 V Separately

Two L type PCBs have been modified to supply either the 1.25 V or the 2.5 V while the respective second voltage was provided directly by the Agilent power supply. The intention was to cross check the theories described in the last section and to gain a better understanding of the individual influences of the two supplied voltages. However, it is not possible to decouple 1.25 V and 2.5 V completely since they share their ground potential.

Figure 7.22(a) shows the noise of module 6.4, powered with these modified L type boards. If the converter PCB supplies only 1.25 V, the total amount of noise is clearly reduced compared to powering both voltages by the converter. This could mean that the APV's CM subtraction removes most of the noise generated due to the 1.25 V. Noise generated by 2.5 V seems to be injected behind the on-chip CM subtraction. Both would be consistent with the layout of the APV's analogue chain, where 1.25 V affects the signal mainly within the preamplifier, while 2.5 V are used throughout the chain [60]. This would also explain why the difference in the noise of open strips is less distinct if the L type supplies only 2.5 V. Since in this case the 1.25 V causes less CM, the values subtracted by the APV are smaller and the open channels move less.

The noise of the module edge channels is shown in Fig. 7.23. As expected from the results shown above (Fig. 7.21), these channels are more sensitive to fluctuations of the 1.25 V.

Channels at the APV borders are also more sensitive to fluctuations of 1.25 V (Fig 7.22(b)). This agrees with the mechanism described in Sect. 7.2.2.

According to Fig. 7.24 the anti-correlation among the adjacent channels is caused by fluctuations of 1.25 V. The common mode generated by 2.5 V even reduces the anti-correlations slightly.

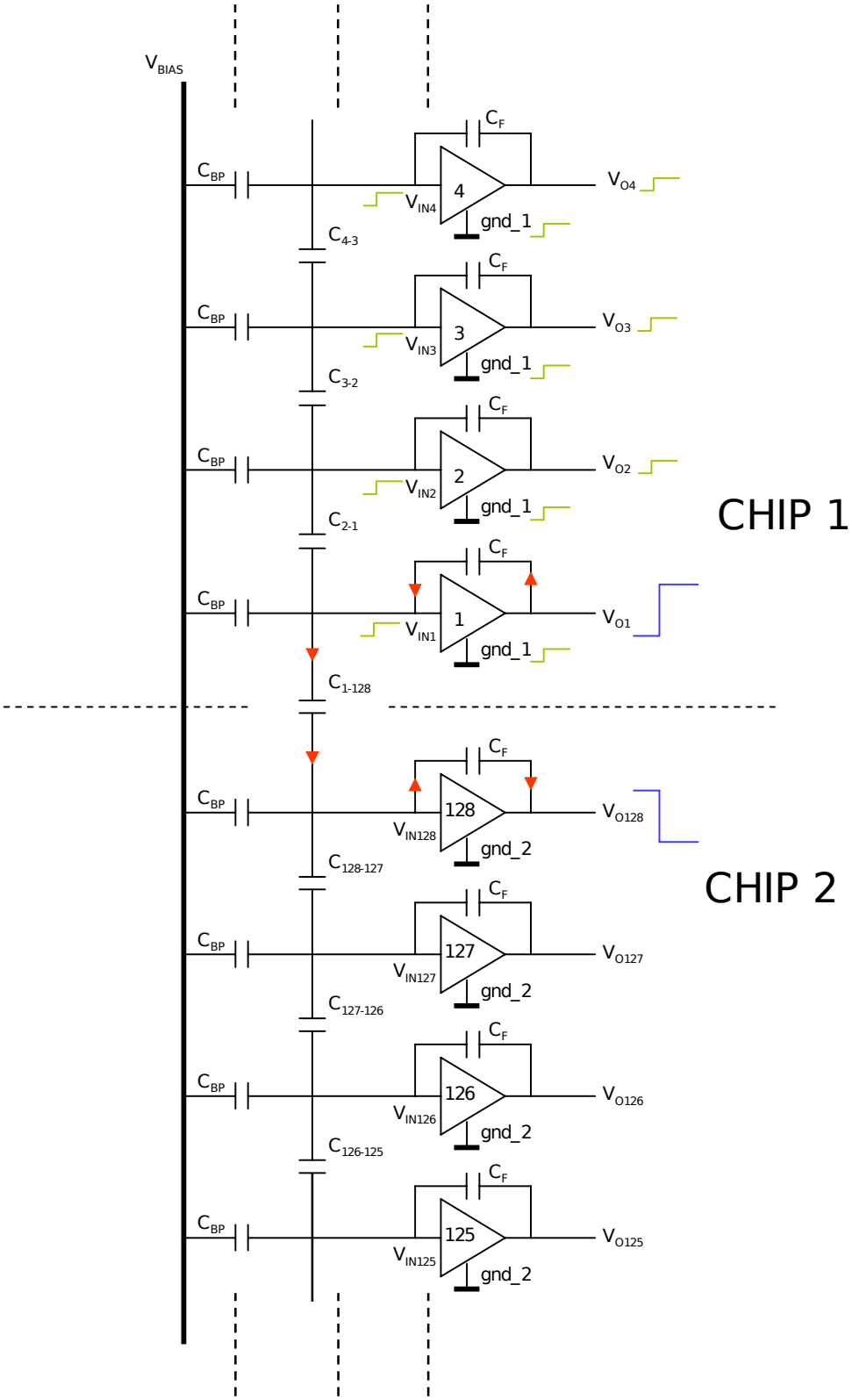

Figure 7.17: Schematic model of the connection between the sensor capacitance network and the charge preamplifier inputs in the boundary region between two chips [58]; gnd_1 and gnd_2 are connected to 1.25 V.

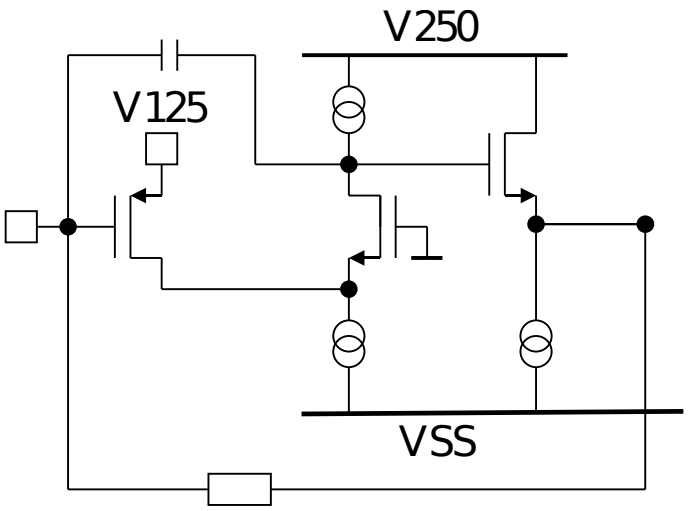

Figure 7.18: Schematic of the preamplifier of the APV. [20].

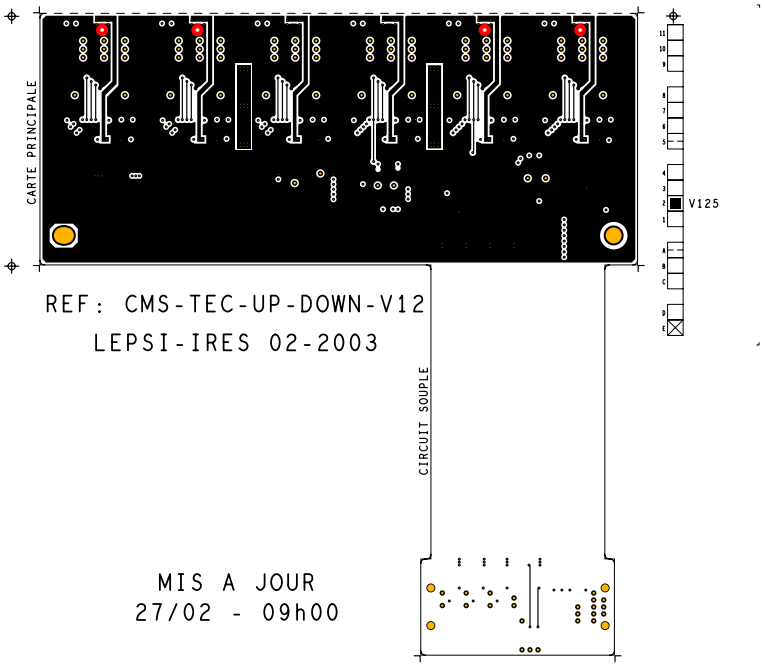

Figure 7.19: Layout of the 1.25 V layer of the front-end hybrid. The black part provides 1.25 V. The APVs are connected to this layer at the positions indicated by the red dots [59].

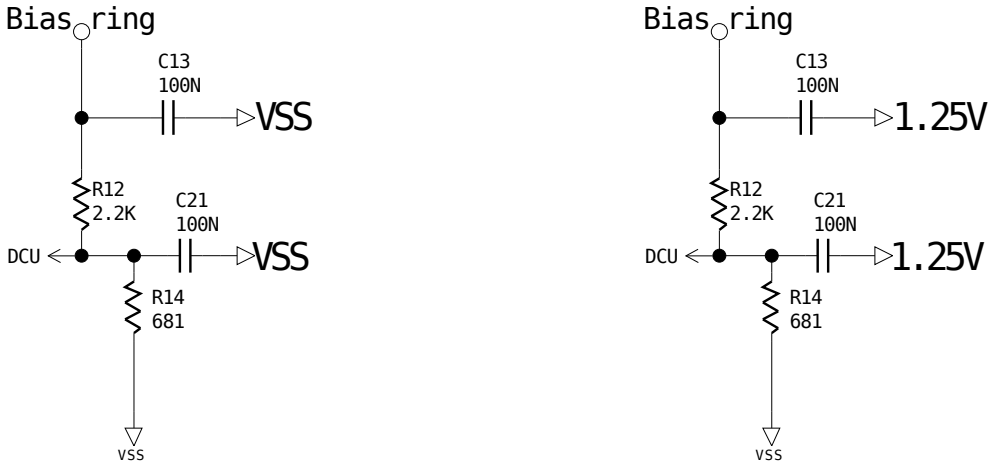

Figure 7.20: In the left figure, the bias ring is AC-coupled to the ground potential of the hybrid. In the right figure the bias ring is AC-coupled to 1.25 V [59].

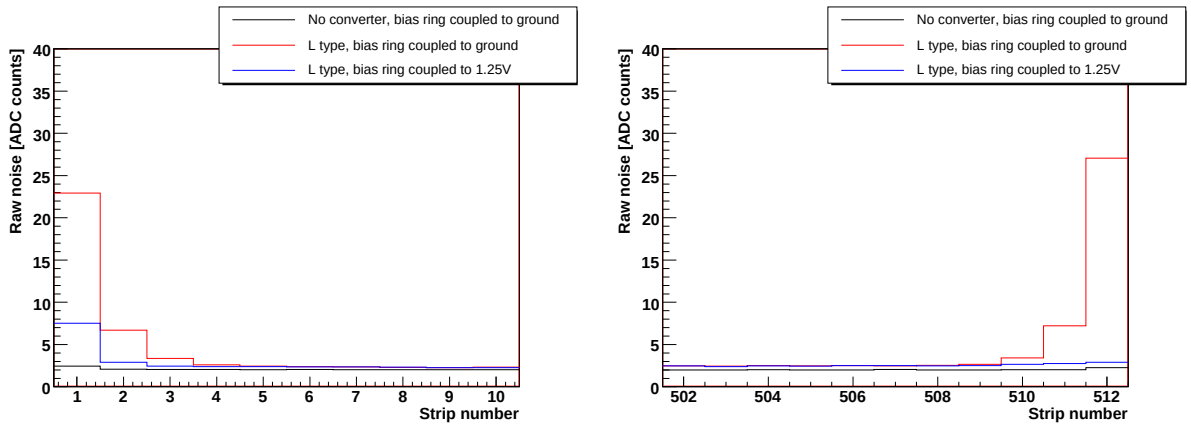

(a) First strip of the module (1).

(b) Last strip of the module (512).

Figure 7.21: Noise of the edge strips of module 6.2. The bias ring was connected to the hybrid ground during the measurements shown in black and red. They have been recorded without and with converter, respectively. During the measurement represented by the blue line, the module was powered by the L type PCB and the bias ring was connected to 1.25 V.

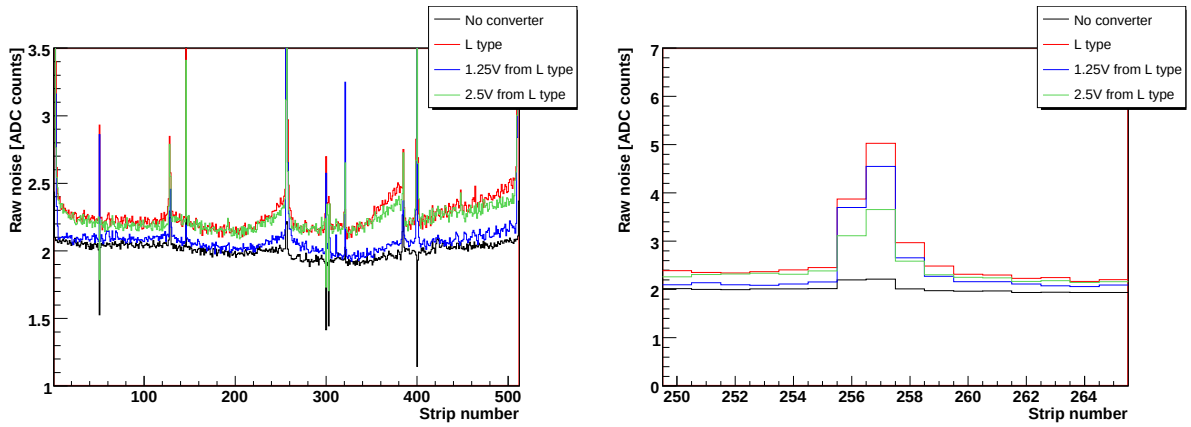

(a) All 512 channels of module 6.4.

(b) The border between APV2 and APV3.

Figure 7.22: Noise of module 6.4. In black a measurement without converter is shown. The noise with the L type PCB is shown in red, while the measurements where the PCB supplies only 1.25 V or 2.5 V are shown in blue and green, respectively.

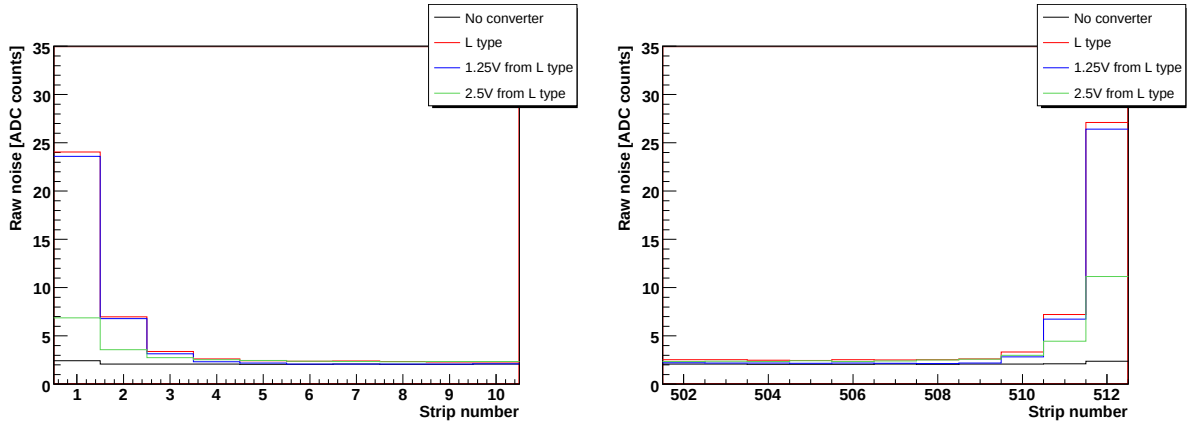

(a) The first channel (1). (b) The last channel (512).

Figure 7.23: Noise of the first and the last channel of module 6.4. In black a measurement without converter is shown. The noise with the L type PCB is shown in red, while the measurements where the PCB supplies only 1.25 V or 2.5 V are shown in blue and green, respectively.

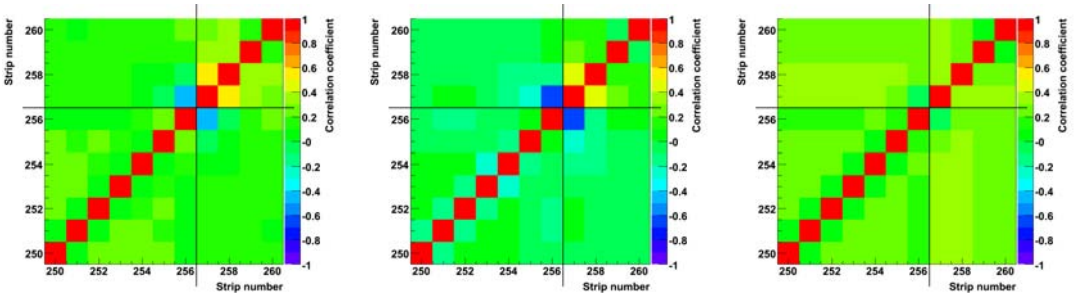

(a) L type supplies both voltages. (b) L type supplies only 1.25 V. (c) L type supplies only 2.5 V

Figure 7.24: Correlations among the adjacent channels of APV2 and APV3. The source of the individual voltages is varied.

7.2.4 Influence of the Converter Input Voltage

To evaluate how the input voltage or rather the conversion ratio r of the converters affects the noise of the module, the L type PCB has been operated at different input voltages. According to Equations 5.6 and 5.9 the converter output noise δ_{out}/V_{out} is proportional to:

$$\frac{\delta_{out}}{V_{out}} \propto 1 - \frac{V_{out}}{V_{in}} = 1 - r. \tag{7.2}$$

Thus a decrease of the conversion ratio should lead to a linear increase of the converter's output noise.

Figure 7.25 shows the noise for input voltages of 3.0 V, 5.5 V and 7.0 V. In Fig. 7.26 the average noise of module 6.4 is shown as a function of the converter's input voltage. The noise of the module is averaged over the channels in two steps. In the first one all channels are used to calculate a temporary mean value and its standard deviation. In the second step this calculation is repeated and strips that differ by more than 5 standard deviations from the first mean value are ignored. As expected from the converter noise, the module noise increases linear for decreasing conversion ratios.

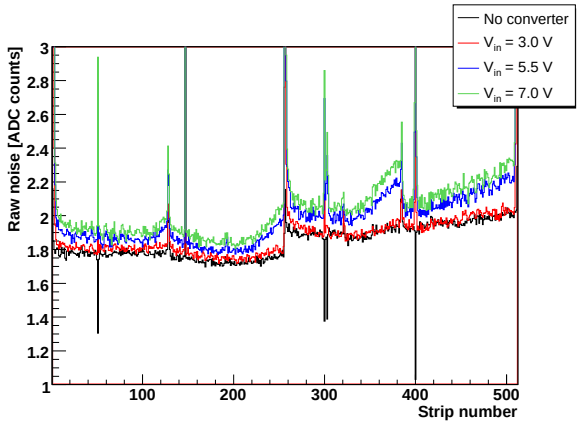

Figure 7.25: Noise of module 6.4 powered by the L type PCB. In black the result without converter is shown. The noise shown in red, blue and green corresponds to measurements with the L type PCB, operated with input voltages of 3.0 V, 5.5 V and 7.0 V, respectively.

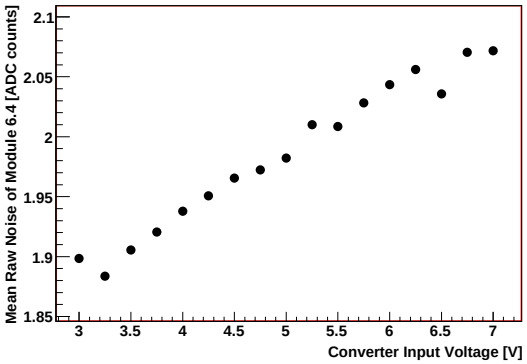

Figure 7.26: Average noise of module 6.4 as a function of the converters' input voltage.

7.2.5 Crosstalk

One concern related to the use of DC-DC converters was the generation of crosstalk between the modules. To investigate this, a measurement in which all four modules were powered by converter PCBs (Fig. 7.27(c), has been compared with a run in which only module 6.4 was powered by a converter PCB, and with a run in which the modules were powered conventionally. The related correlations between the modules are shown in Fig. 7.27. The decreased correlation of the second two APVs of module 6.1 is caused by a faulty laser. Since this is not related to the DC-DC converters, it appears in all matrices. The correlations of module 6.3 seem to be slightly enhanced in Fig. 7.27(b), compared to Fig. 7.27(a). Subtracting the correlations of the modules 6.1-6.3 measured without converters from the ones recorded with a converter PCB on position 6.4 leads to the distribution shown in Fig. 7.27(d). If module 6.4 is neglected, the average difference between the two correlation matrices still remains about 0.5 σ from zero. This is not a catastrophic result, in particular because the noise of module 6.3, shown in Fig. 7.28 is not increased if a L type PCB is used to power the neighbouring module 6.4. However, the effect is not completely negligible and should be kept in mind with regard to tests with larger systems.

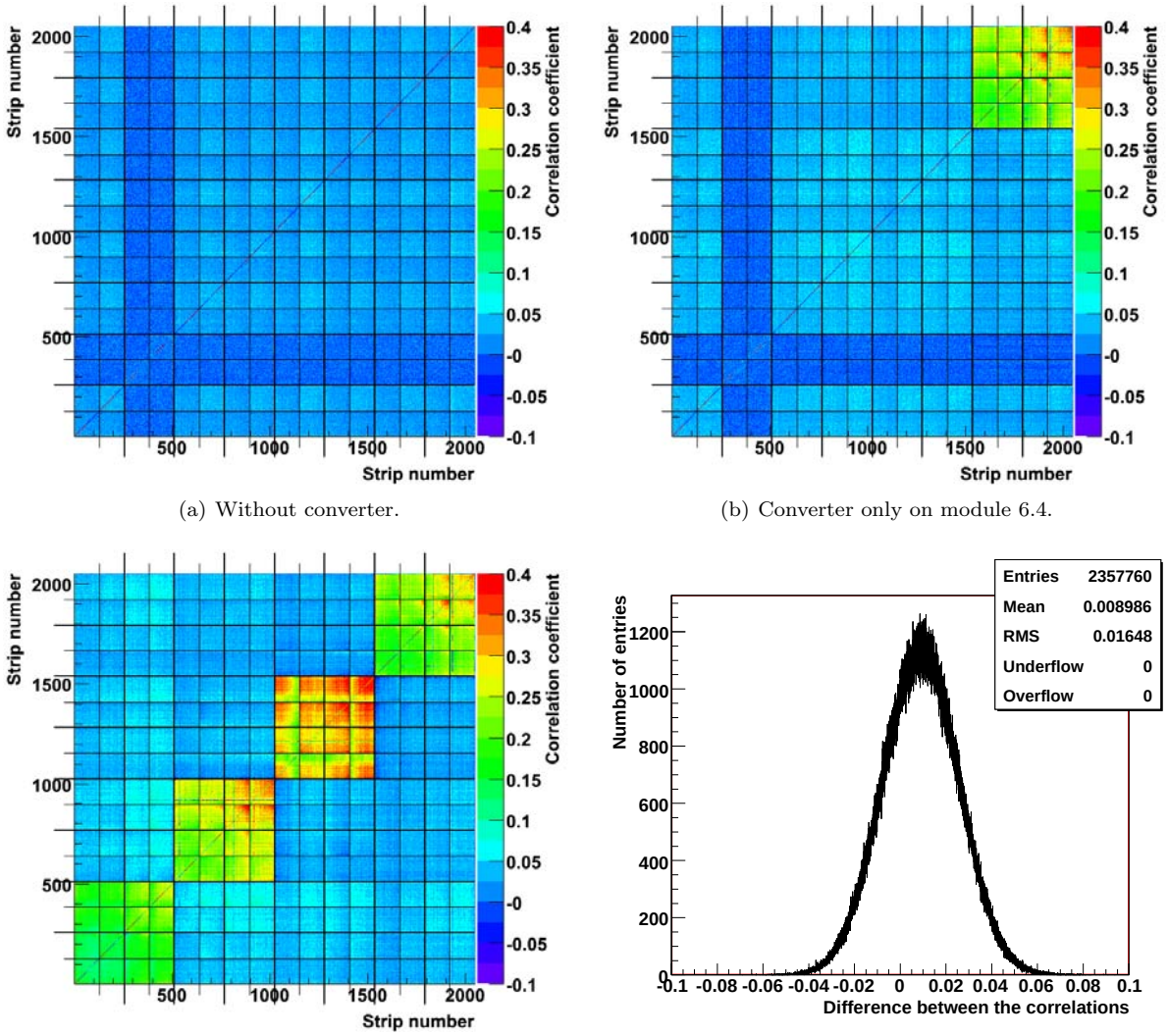

(a) Without converter.

(b) Converter only on module 6.4.

(c) Converters on all modules.

(d) Distribution of the correlation differences.

Figure 7.27: Correlations of all four modules in different converter configurations. Blocks of 512 strips correspond to one module. In (d) the correlations without converter have been subtracted from the values of the measurement with only one converter. The values of module 6.4 and the main diagonal have not been considered for this, because they are certainly dominated by the converter or perfectly correlated, respectively.

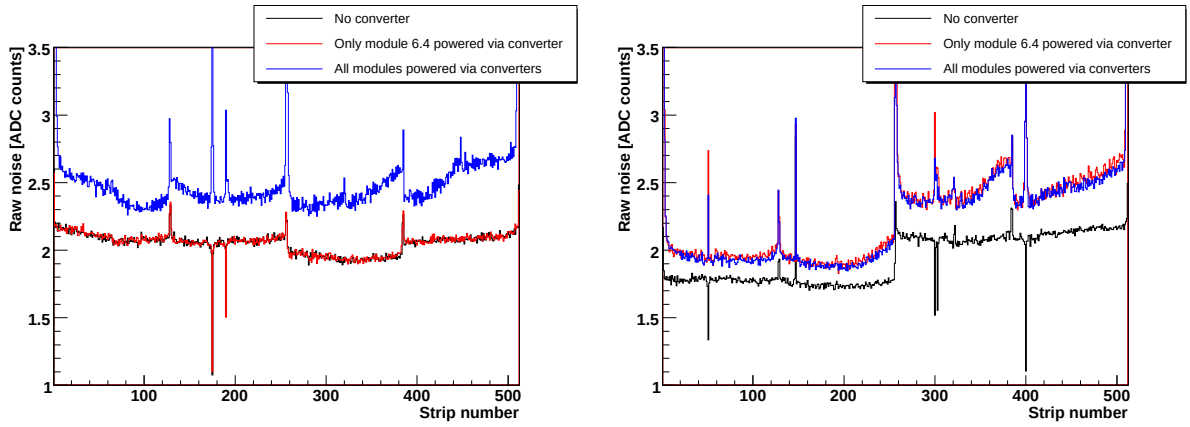

(a) Module 6.3.

(b) Module 6.4.

Figure 7.28: Noise of the modules 6.3 and 6.4. During the measurement shown in black, all modules were powered conventionally. The data shown in red correspond to a measurement in which only module 6.4 was powered by the L type PCB. During the run shown in blue, all modules were powered by L type PCB, except for module 6.1 which was powered by a S type board.

7.2.6 Effect of different PCB Layouts

The S Type PCB

A comparison between the S type and the L type PCB in terms of the module noise is shown in Fig. 7.29. To determine if the difference is related to the PCB layout or caused by statistical spread, all available converter PCBs have been tested. In total 11 S type and 14 L type boards have been operated with module 6.4. Figure 7.30 shows the distribution of the average noise of module 6.4. The S type is slightly but significantly better.

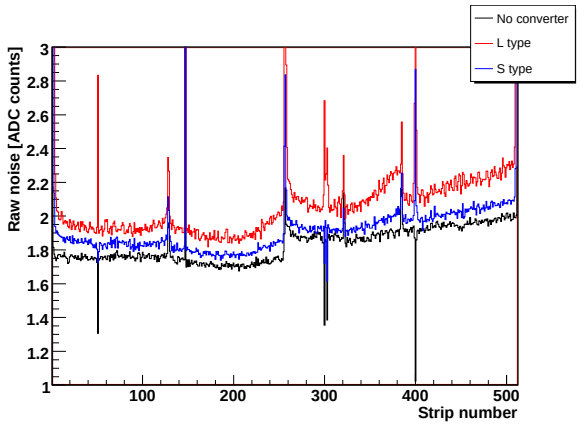

Figure 7.29: Comparison of the noise of module 6.4, powered in the standard way (black), by the L type (red) and the S type PCB (blue).

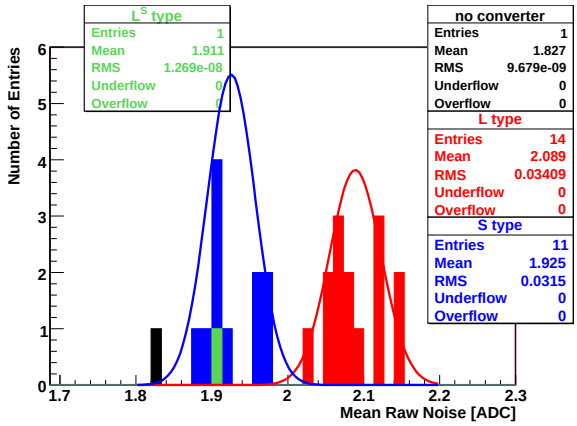

Figure 7.30: Distribution of the average noise of module 6.4, powered in the standard way (black), by the L type (red) and the S type PCB (blue). The green entry represents the L^S type.

To understand the reason for this difference, a L type and a S type board haven been merged to a so-called L^S PCB, which is basically a L type operated on the connector bridge of the S type. A photograph is shown in Appendix A.2. All three PCBs, S, L and L^S are compared in Fig. 7.30. The noise generated by the L^S board fits perfectly into the distribution of the S type. Hence the bridge connection of the S PCB should be responsible for the better noise performance of this type.

Further studies were performed to investigate if the improvement of the noise performance is caused by the increased distance between the converter PCB and the module or if the connector bridge works as some kind of noise filter. Module 6.4 was powered with the S type PCB while the position of the PCB was varied. This was possible after connecting it to its bridge via a cable measuring 10 cm in length and mounting it

on a plastic bar (Fig. 7.31). Due to the bar the cover of the petal box was removed, which did not affect the noise of the modules. The recorded measurements are summarised in Fig. 7.32. The noise of module 6.4 is not affected by the distance between the converter PCB and the module if the PCB is placed at the standard position of the L type board, or further away. Hence the connector bridge of the S type seems to work as a noise filter. The cable added between the S type and the bridge increases the filtering effect.

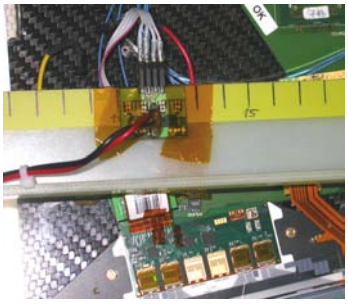

Figure 7.31: Photograph of the S type PCB mounted on a plastic bar and connected to its bridge via a cable measuring 10 cm in length.

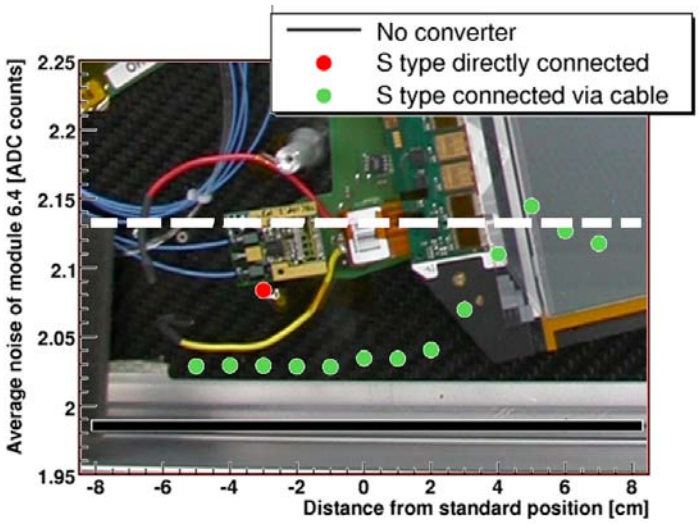

Figure 7.32: Average noise of module 6.4 as a function of the distance from the standard position of the L type PCB. The reference noise level recorded without converter is represented by a black line. The measurement recorded with the S type PCB directly connected to its bridge is shown in red. In green the measurements are shown in which the S type was connected via a 10 cm long cable. The photograph in the background shows an extract of the set-up. The scaling has been adjusted to match the x-axis. The white dashed line indicates the y-position of the converter PCB.

Operating the S type PCB above the module/hybrid increases the noise. This indicates that the converter PCB emits radiative noise. According to the relation between the increase of the noise and the position of the converter, it seems as if the radiated noise couples into the pitch adapter. In Fig. 7.33 corresponding noise distributions are shown. The potentially induced noise generates a wing structure in the module's noise. The edge channels of the APV which shows the increased noise are anti-correlated among each other (Fig. 7.34). A possible explanation for this is given in Sect. 7.3.2. Figure 7.35 shows the converter position that caused the highest noise. Judging from this, it is also possible that the APV could be affected by noise radiated from the connector between the cable and the S type PCB.

To improve the noise performance of the L type PCB, additional capacitors haven been installed on the converters' outputs. A single board was instrumented consecutively with 10 µF, 22 µF and 100 µF. As can be seen in Fig. 7.36 the capacitors did not provide any benefits. The noise level remains virtually constant during all measurements. Further studies aiming at the noise reduction achieved with the S type bridge are necessary.

7.2.7 Effect of a Low DropOut Regulator

In another attempt to reduce the noise of the converters, a L type PCB has been equipped with LTC3026 Low DropOut Regulators (LDO) from Linear Technology [61]. The schematics and a photograph of the PCB are shown in Appendix A.3. The LTC3026 was chosen for its low dropout voltage (in this application 50 mV or 100 mV) and its wide rejection spectrum. The latter can be seen in Fig. 7.37. A comparison of converters with and without LDO is shown in Fig. 7.38. The LDO reduces the effect of the converters on the noise significantly and establishes a noise level almost as good as without converters. Increasing the dropout voltage from 50 mV to 100 mV has no effect on the module's noise. Hence 50 mV is sufficient, which

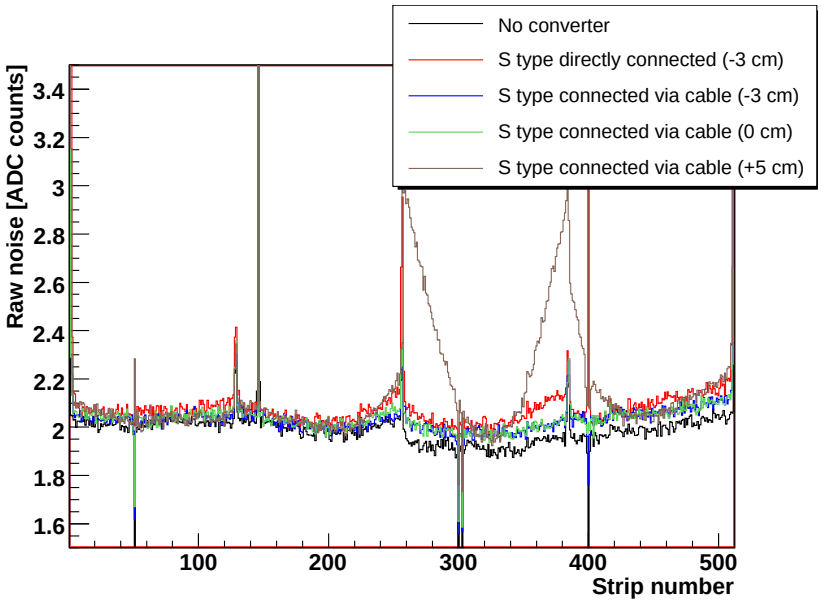

Figure 7.33: Noise of module 6.4. In black a measurement without converter PCB is shown. The noise shown in red was recorded with the S type PCB directly connected to its bridge, powering the module. During the run shown in blue the PCB was placed above its original position on a plastic bar. The connection to the bridge PCB was established via a cable measuring 10 cm in length. For the data shown in green the S type PCB was moved above the normal position of the L type board. The measurement in brown shows the noise recorded while the PCB was placed above the module.

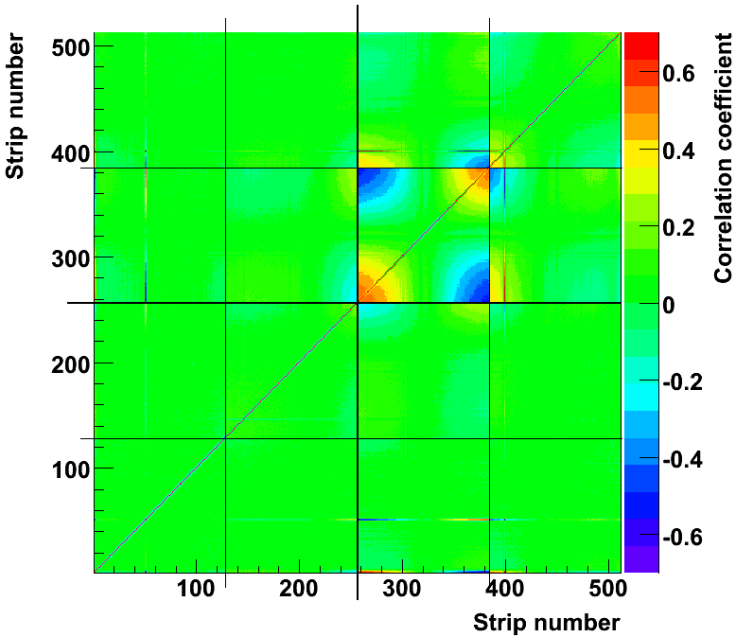

Figure 7.34: Correlations of module 6.4, powered by the S type PCB. The PCB was placed above the module, 5 cm ahead of the standard position of the L type or rather 8 cm ahead of the standard S type position.

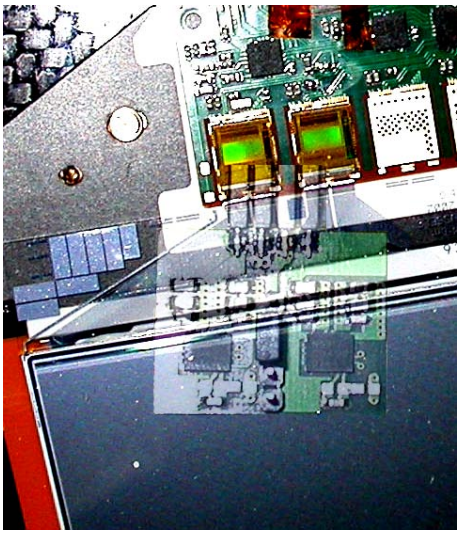

Figure 7.35: Photograph of a part of module 6.4. A semi-transparent photograph of the S type PCB has been inserted at the spot corresponding to the measurement shown in brown in Fig. 7.33.

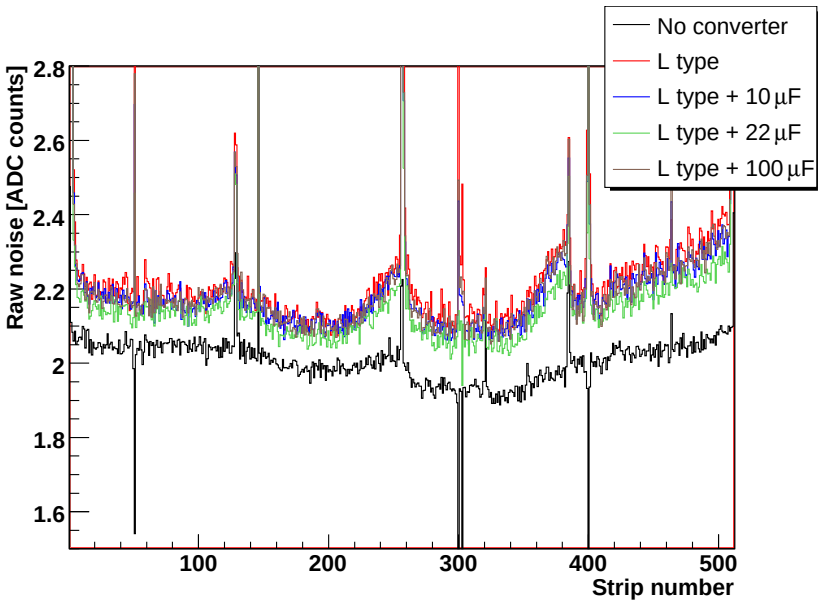

Figure 7.36: Noise of module 6.4. The module was powered conventionally without converters (black) and by a L type board (red). The L type was consecutively instrumented with an additional capacitance of 10 µF (blue), 22 µF (green) or 100 µF (brown).

is good with regard to efficiency. The noise of the edge strips, shown in Fig. 7.39, is also reduced due to the LDO. It has to be noted that the LDO reduces the efficiency of the converter, since already the 50 mV dropout voltage corresponds to 4% of 1.25 V. A radiation hard LDO has yet to be developed.

7.2.8 Supplying the Converters with Power via the ICB

To achieve more realistic test conditions, the converters have also been powered via the ICB. In this case, the Agilent power supply was connected to the 1.25 V layer of the ICB and provided 5.5 V. The according measurements showed slightly reduced noise and correlations compared to measurements in which the converters were powered via external cables. Figure 7.40 shows the module noise for both cases. In Fig. 7.41 the corresponding correlation matrices are compared. If the converters are powered via cables, noise and correlations of modules 6.2 and 6.3 are slightly increased. This could be caused by radiative emissions off the cables.

7.2.9 Noise Performance of a different Converter

To estimate the effect of the converter's switching frequency on module noise, another commercial converter chip, the MIC3385 [40], has been tested. This device operates at about 8 MHz. A PCB similar to the L type, but carrying two Micrel chips has been designed to integrate the converters. A photograph of this Micrel PCB and its schematics can be found in Appendix A.4.

According to noise susceptibility tests by M. Raymond [62] the APV is most sensitive to fluctuations in the frequency range around 2.5 MHz. This corresponds approximately to $1/(2\pi\tau)$, where τ is the APV's shaping time of 50 ns.

F. Arteche and C. Rivetta showed in a similar test that a complete petal is most sensitive to frequencies around 8.5 MHz and 28.5 MHz [63].

In Fig. 7.42 the noise of module 6.4 powered by the Micrel PCB is compared with the noise measured with the Enpirion L type. On average the noise with the Micrel PCB is approximately 0.5 ADC counts higher than with the L type PCB. The noise on the module edge strips, shown in Fig. 7.43, is about 25% smaller if the power is provided by the Micrel PCB. This is no contradiction since the noise of the edge strips is suspected to be generated within the preamplifiers (Sect. 7.2.2), while the CM which is not removed by the inverter of the APV should be injected behind this stage.

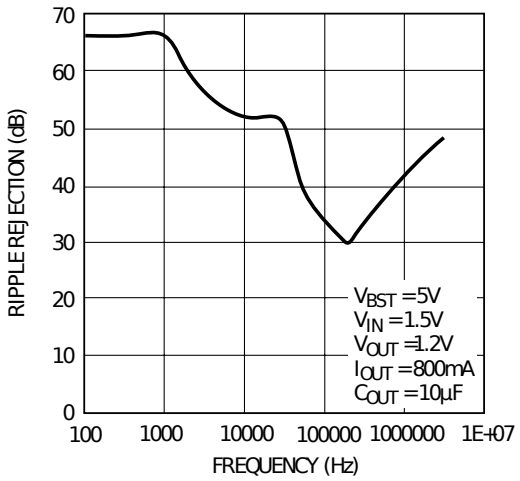

Figure 7.37: Ripple rejection of the LTC3026 LDO as a function of the ripple frequency [61].

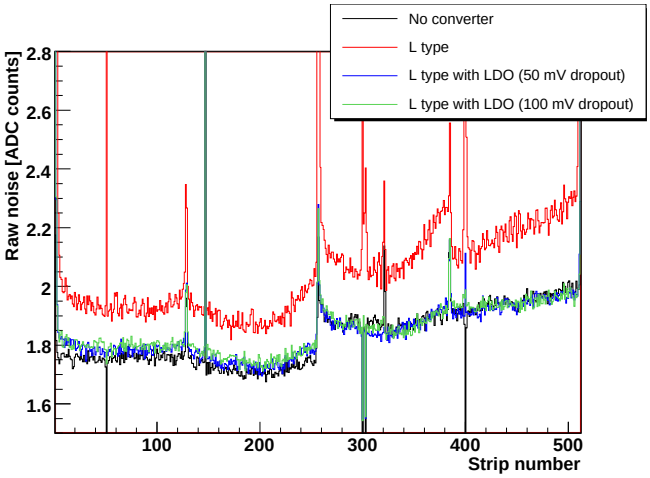

Figure 7.38: Noise of module 6.4. The module was powered conventionally without converters (black), by a standard L type board (red) and by two L type PCBs instrumented with LDOs. The results obtained with the LDOs are shown in blue and green, corresponding to dropout voltages of 50 mV and 100 mV, respectively.

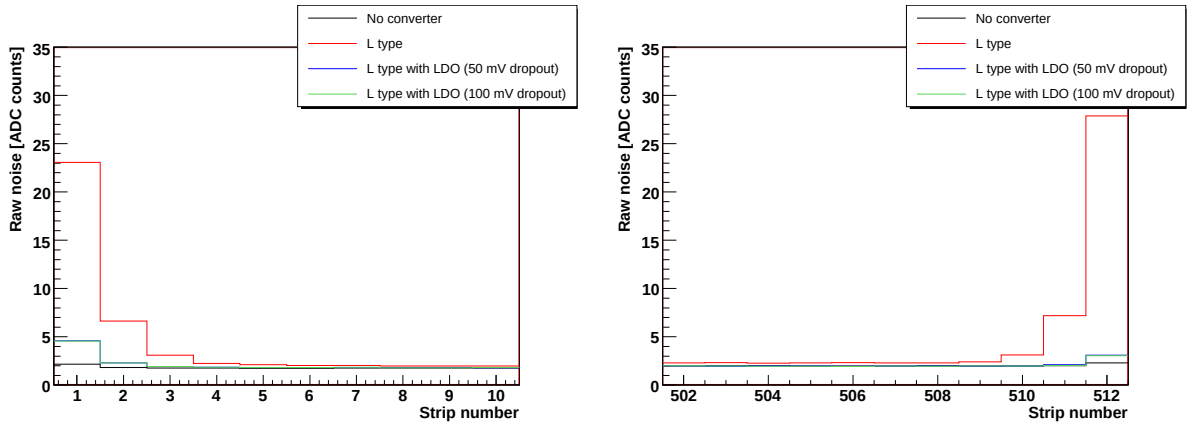

(a) First channel (1).

(b) Last channel (512).

Figure 7.39: Noise of edge strips of module 6.4. The module was powered conventionally without converters (black), by a standard L type board (red) and by two L type PCBs instrumented with LDOs. The results obtained with the LDOs are shown in blue and green corresponding to dropout voltages of 50 mV and 100 mV, respectively.

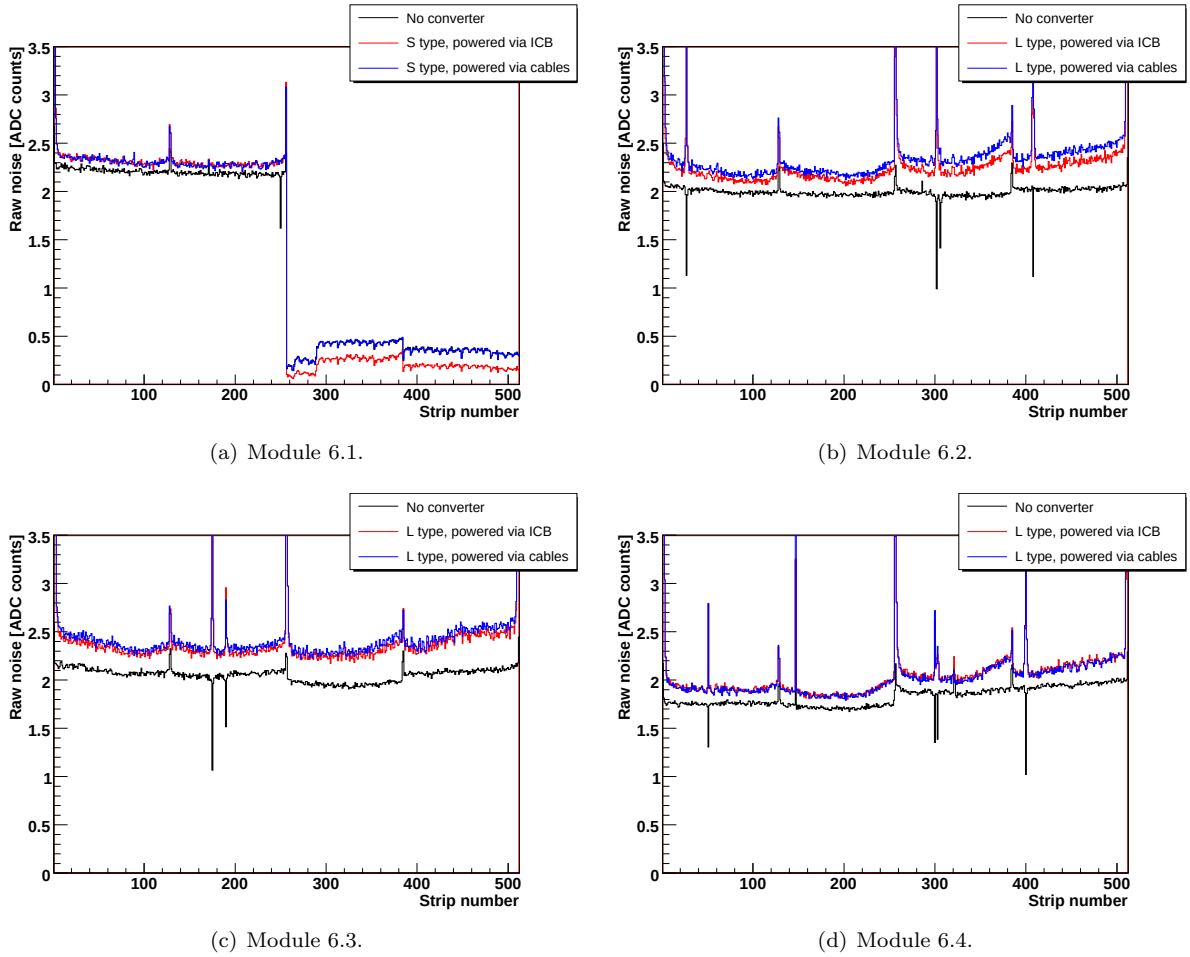

(a) Module 6.1.

(b) Module 6.2.

(c) Module 6.3.

(d) Module 6.4.

Figure 7.40: Noise of all four modules. A reference measurement without converters is shown in black. In addition, two measurements are shown in which a S type board powers module 6.1 and the remaining modules are powered by L type PCBs. The converters were powered via the ICB, as well as via external cables. This is shown in red and blue, respectively. The low noise of the second half of module 6.1 is related to a problem with a laser in the read-out chain.

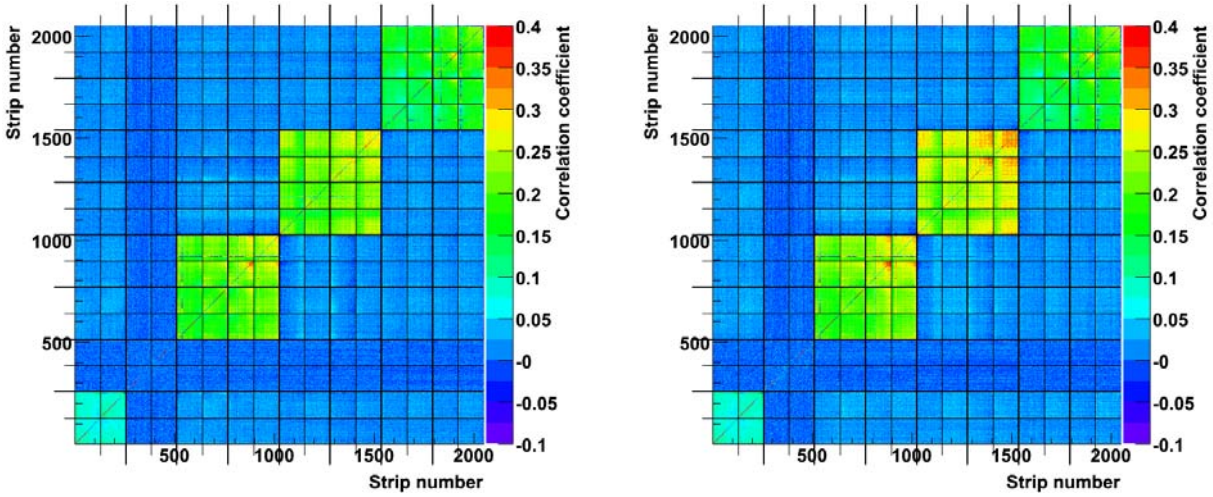

Figure 7.41: Correlations between all four modules, powered by converter PCBs. In the left plot, the converters are powered via the ICB. In the right plot the converters are powered via external cables. The exceptional correlations of the second half of module 6.1 are related to a problem with a laser in the read-out chain.

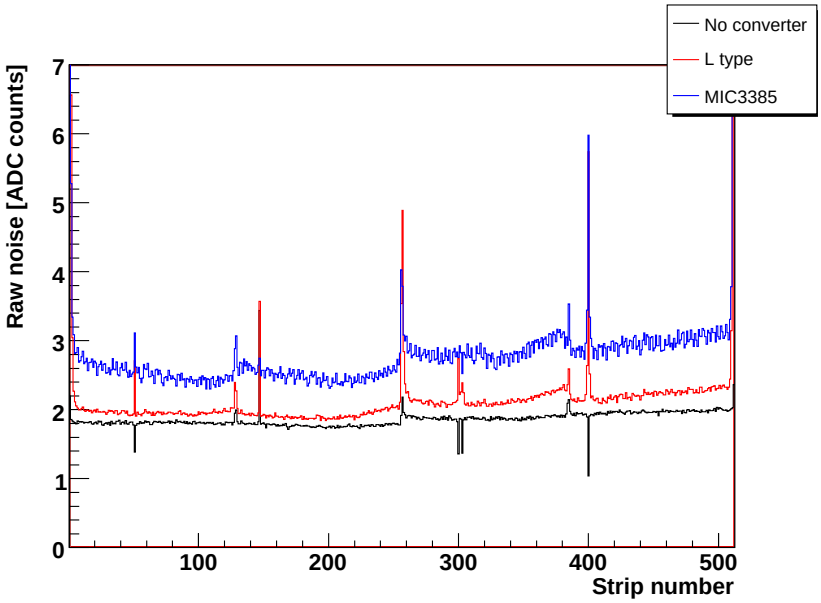

Figure 7.42: Noise of module 6.4. The module was powered conventionally without converters (black), by a standard L type board (red) and by a Micrel PCB (blue).

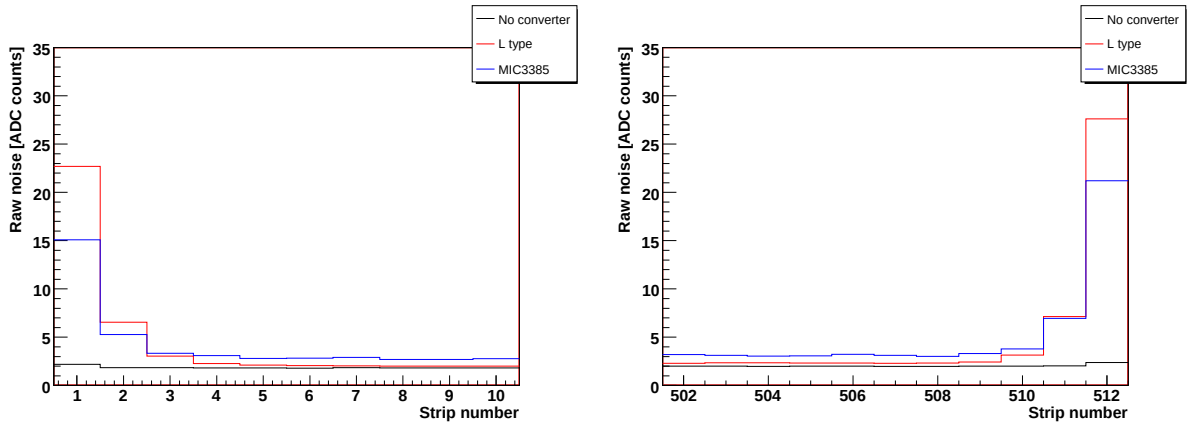

(a) First channel (1).

(b) Last channel (512).

Figure 7.43: Noise of edge strips of module 6.4. The module was powered conventionally without converters (black), by a standard L type board (red) and by a Micrel PCB (blue).

7.3 Buck Converters with External Inductors

The use of air-core inductors is mandatory to operate inductor-based converters in the 4 T magnetic field of the CMS detector. The required inductance of several hundred nH leads to macroscopic inductors which occupy a volume in the order of a cubic centimetre (Fig. 5.8). Hence they cannot be integrated into the converter chip but must be assembled as discrete elements.

The following measurement has been recorded with a re-designed L Type converter PCB, equipped with two EQ5382D [39] converter chips (Sect. 5.1.2), each operated with a 538 nH air-core inductor (132-20SM_L) from Coilcraft. This PCB, the so-called L_AirCore, is shown in Fig. 7.44. Its schematic can be found in App. A.5.

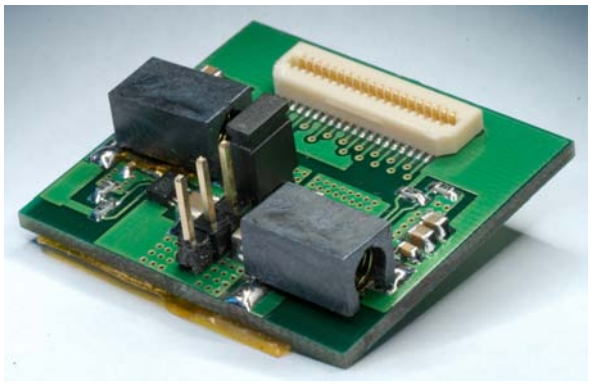

Figure 7.44: Photograph of the L_AirCore converter PCB with external air-core inductors.

Figures 7.45(a) and 7.45(b) show the noise of the modules 6.3 and 6.4, respectively. During the measurement shown in red, module 6.4 was powered by the L_AirCore PCB. The converter increases the noise of this module dramatically. The additional noise is shaped like wings peaking at the APV borders. Supperimposed is a periodic structure which is dominant at the centre of the APVs. The wings are most pronounced on the inner APVs. As can be seen in Fig. 7.45(a), the L_AirCore PCB powering 6.4 does also affect the noise of module 6.3, which was powered in the conventional way. Note that the position of the converter was physically closer to the channels on the right side of the plot. The noise on the edge strips of the module which is powered by the converter PCB reaches up to 85 ADC counts. This is shown for module 6.2 in Fig. 7.46 with the module bias ring coupled to the hybrid's ground potential, as well as to 1.25 V. The latter reduces the edge strip noise significantly. This was expected from the measurements with the standard L type (Sect. 7.2.2).

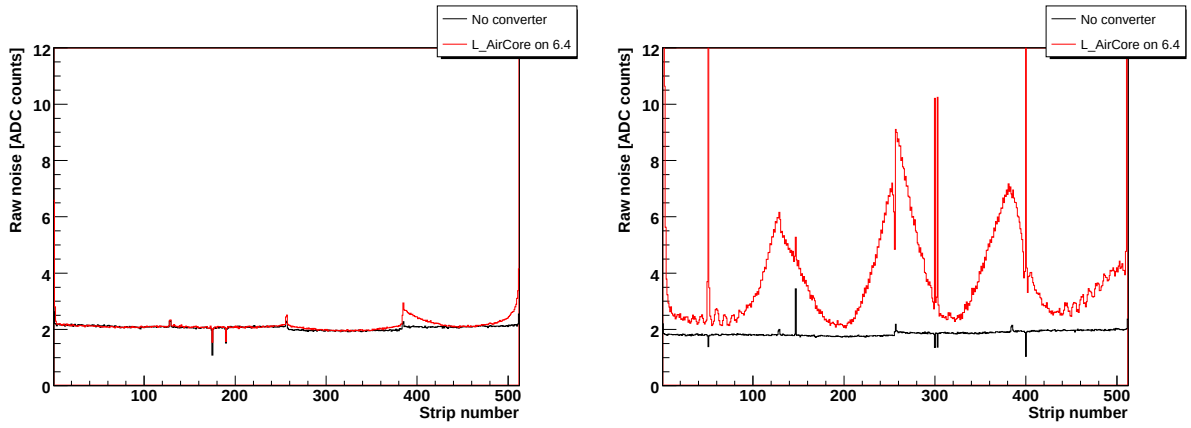

(a) Module 6.3.

(b) Module 6.4.

Figure 7.45: Noise of modules 6.3 and 6.4. In black a measurement with conventional powering is shown. During the measurement shown in red, module 6.4 was powered by the L_AirCore converter PCB while module 6.3 was powered conventionally.

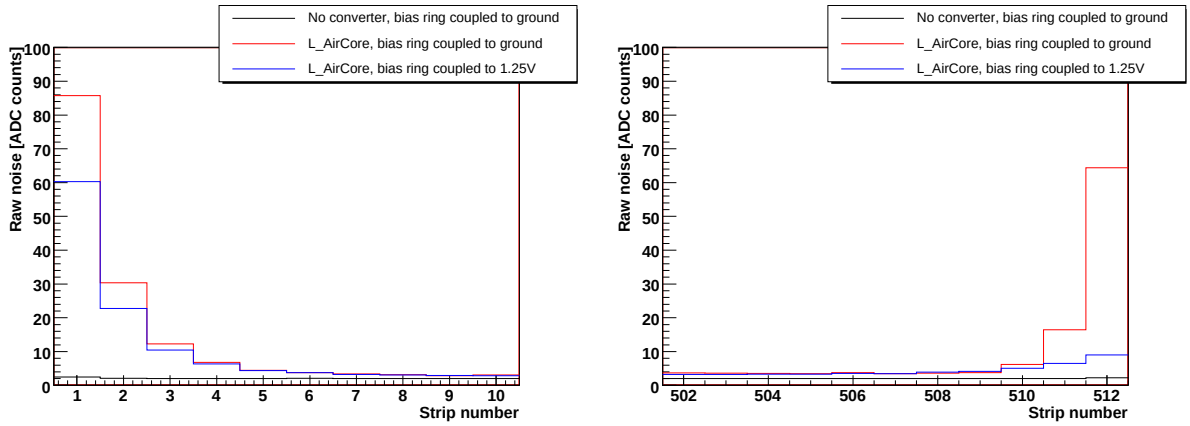

(a) First channel (1).

(b) Last channel (512).

Figure 7.46: Noise of the edge channels of module 6.2. In black a measurement with conventional powering is shown. During the measurement shown in red and blue the module was powered by the L_AirCore converter PCB while the module's bias ring was connected to the ground on the hybrid and to 1.25 V, respectively.

To estimate the influence of the fact that the used inductors are discrete components, another PCB has been equipped with EQ5382D chips in combination with external ferrite-core inductors (LQH32CN1R0M23) from muRata. Within this document this PCB is labelled L_FerriteCore (see A.7). In Figure 7.47 the noise of module 6.4 powered by the L_FerriteCore PCB is compared with measurements recorded with the L type and the L_AirCore board. The L_FerriteCore PCB is nearly as good as the L type. The only differences between their noise distributions are small wings on APV3 and APV4 (which are closest to the converter).

Installing a LDO on the L_AirCore board does not yield great improvements. A photograph and the schematic of the according PCB can be found in App. A.6. A comparison between a measurement with this PCB and the standard L_AirCore is shown in Fig. 7.48.

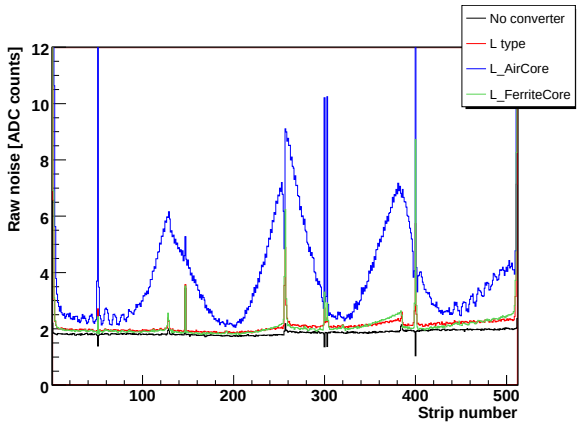

Figure 7.47: Noise of module 6.4. Measurements without converter (black), with the L type (red), with the L_AirCore (blue) and with the L_FerriteCore PCB (green) are compared.

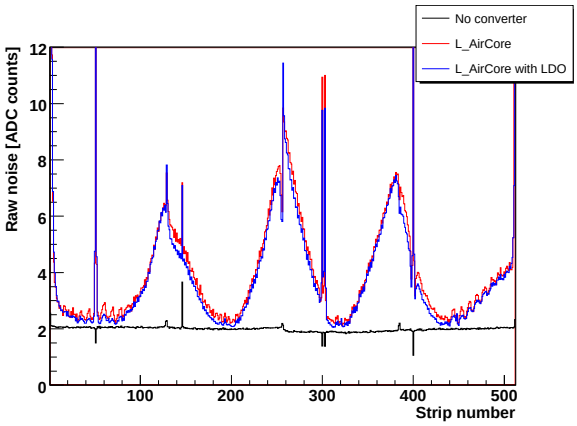

Figure 7.48: Noise of module 6.4. The noise without converter is shown in black. In red and blue the noise recorded with the L_AirCore PCB without and with LDO is shown, respectively.

Figures 7.49 and 7.50 show the noise of module 6.4, powered by the L_AirCore and the L_AirCore PCB with LDO, respectively. In addition, both plots show the module's noise after subtraction of a linear CM. The latter improves the wing structure substantially, in particular in combination with the LDO. Still, the noise of single noisy channels and on the edge channels cannot be removed by the CM subtraction.

Since it is possible to reduce the wing noise distribution, generated by the L_AirCore PCB, by subtracting a linear CM, one would expect an anti-correlation between the first and the second half of the APV (see-saw noise). Figure 7.51 shows the correlations of all four modules when only module 6.4 is powered through the

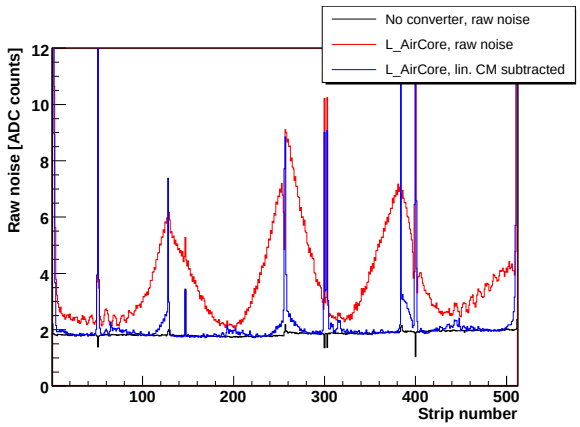

Figure 7.49: Noise of module 6.4. The raw noise without converter is shown in black. Raw noise and CM subtracted noise of the L_AirCore is shown in red and blue, respectively.

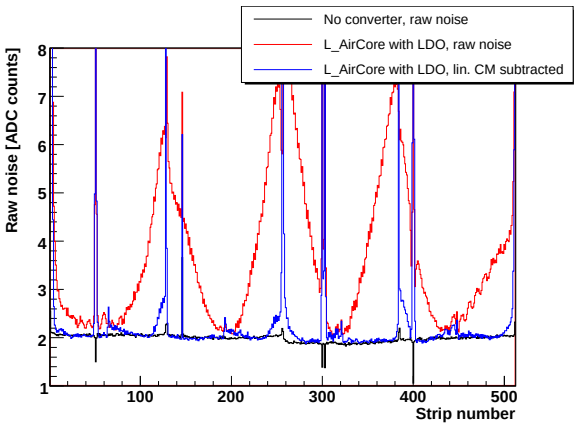

Figure 7.50: Noise of module 6.4. The raw noise without converter is shown in black. Raw noise and CM subtracted noise of the L_AirCore with LDO is shown in red and blue, respectively.

L_AirCore board. The correlation matrix of module 6.4 is magnified in Fig.7.52. Almost all strips of this module are either very strongly correlated or anti-correlated. Furthermore, the expected 64 strip structure is visible and divides each APV into two correlation zones. The first 64 channels of APV1 are relatively weekly correlated among each other and with the rest of the module. The second 64 channels of all four APV are strongly correlated among each other and anti-correlated with the first 64 channels of APV2, APV3 and APV4. Like the noise, the correlations are most intense in the middle of the module. The fact that the converter on module 6.4 affects module 6.3 is also reflected in the correlations of module 6.3 (Fig. 7.53).

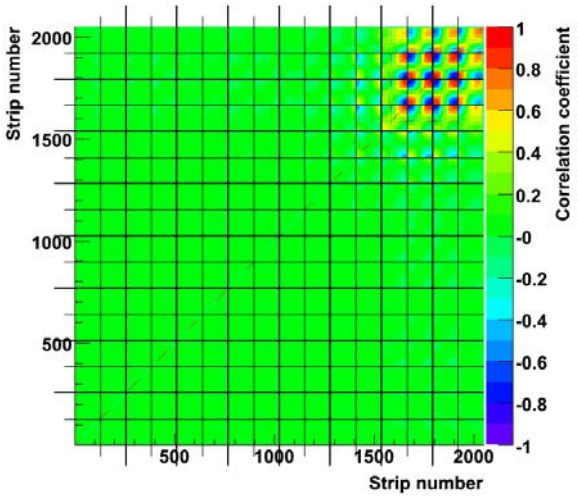

Figure 7.51: Correlation matrix of all four modules. Module 6.4 is powered by the L_AirCore PCB. A bock of 512 strips correspond to one module, starting with strip 1 of module 6.1.

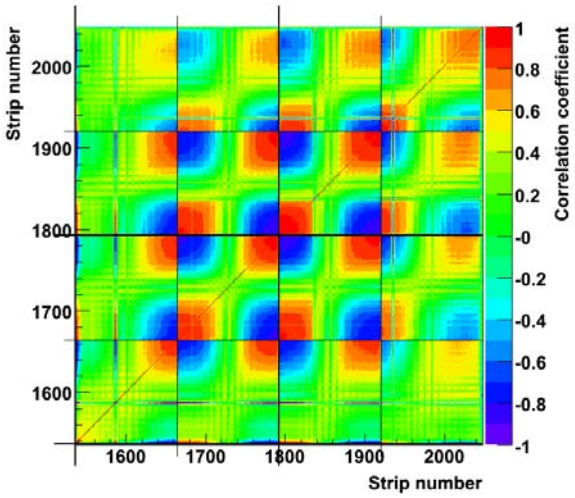

Figure 7.52: Correlations between the channels of module 6.4, powered by the L_AirCore PCB. The first channel of the module corresponds to 1537, the last to 2048.

7.3.1 Origin of the Noise

From the comparisons between the L_FerriteCore and the L_AirCore PCB with and without LDO, it seems likely that the origin of the main fraction of the additional module noise is radiative. This would mean that the electromagnetic field, radiated by the inductors on the L_AirCore board, is responsible. To confirm this the system was powered conventionally while the L_AirCore PCB was placed between module 6.3 and module 6.4. The measurement has been performed with the converter PCB attached to a constant load (approximately 0.5 A per converter) as well as without any load. Figure 7.54 shows the position of the detached converter in the set-up. The corresponding noise of module 6.3 and module 6.4 is shown in Fig. 7.55. Since there is no electrical connection between the converter PCB and the modules, the increase

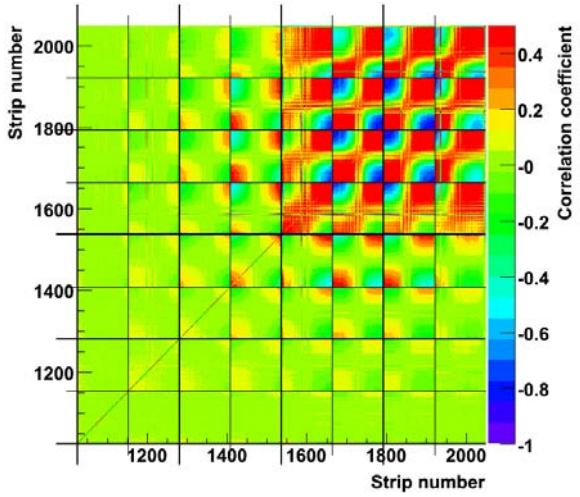

Figure 7.53: Correlations of the modules 6.3 and 6.4. Only 6.4 is powered by the L_AirCore PCB. The strips 1025-1536 belong to module 6.3. Module 6.4 is represented by the strips 1537-2048.

of the noise is caused by the electromagnetic fields of the air-core inductors. The load of the converter does not influence the noise of the modules.

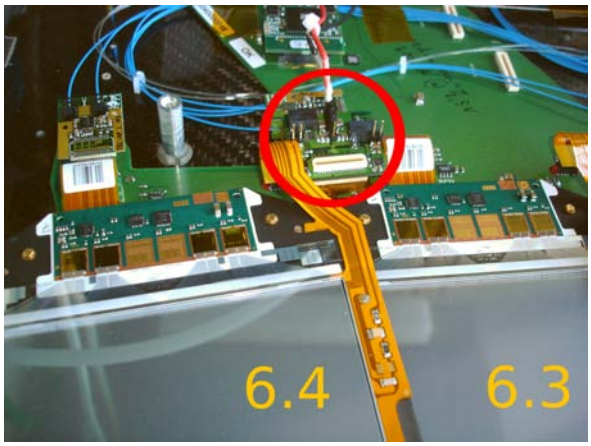

Figure 7.54: Photograph of the L_AirCore PCB placed between module 6.4 and module 6.3.

The measurement with the detached L_AirCore PCB was repeated with a hybrid without pitch adapter and silicon strips. The result of this test is shown in Fig. 7.56. The noise is not increased. Even the edge strips remain silent (Fig. 7.56(b)). Hence the pick-up is only possible if the sensor strips are connected to the hybrid. However this does not imply that the radiation couples into the sensor strips, as will be motivated later.

In a similar measurement the hybrid (without sensor) was powered by the L_AirCore PCB. The result can be seen in Fig. 7.57. The measured noise reaches its maximum in the middle of the APVs. The edge strips are not increased. Since the sensor is not attached to the hybrid, the radiated fields should not affect the hybrid and hence the observed noise has to be conductive. If the L_AirCore PCB is replaced by a L_AirCore board with LDOs, the overall noise level is reduced and the noise distribution is slightly flattened. If the hybrid is powered by the standard L type, the effect on the noise is much smaller. This indicates that the electromagnetic fields of the inductors affect their own PCB as well. Still it is not clear why the noise of a module without sensor differs so much from the noise of a complete module.

If the hybrid is replaced by a hybrid with pitch adapter, the noise generated by the L_AirCore PCB is reduced (Fig. 7.58). When no converter or the standard L type board is used to power the hybrid, the noise remains on the same level as without pitch adapter.

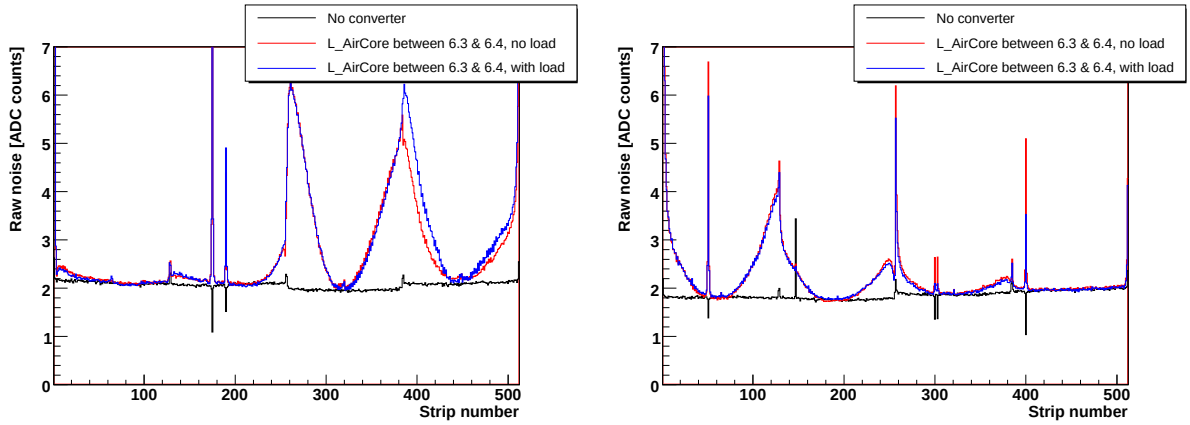

(a) Module 6.3.

(b) Module 6.4.

Figure 7.55: Noise of the modules 6.3 and 6.4 powered conventionally. For the measurements shown in blue and red a L_AirCore was placed between the modules' hybrids, with and without load, respectively. In black the noise is shown without any converters in the set-up.

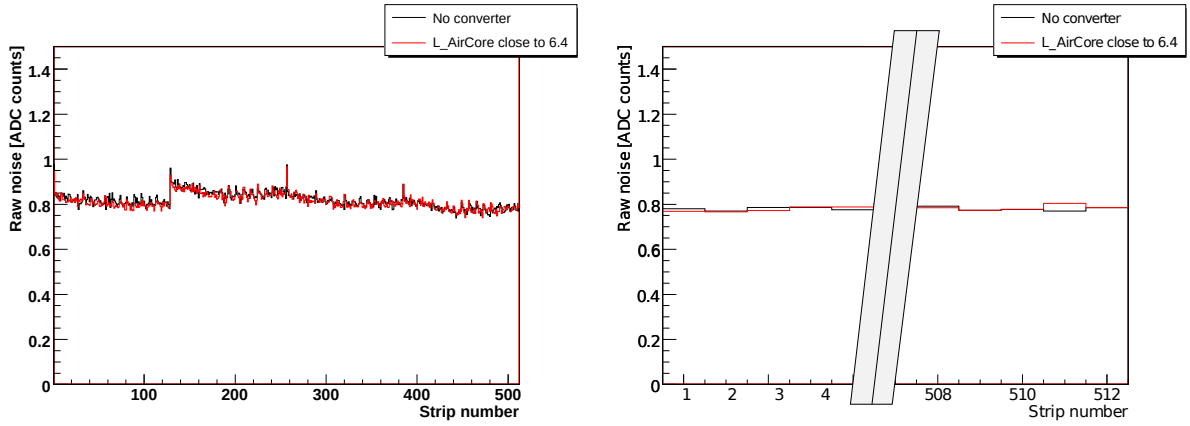

(a) All channels.

(b) The first (1) and the last (512) channel.

Figure 7.56: Noise of a hybrid on position 6.4, powered conventionally. A reference run without a converter in the set-up is shown in black. For the measurement shown in red, a L_AirCore PCB was put close to the hybrid.

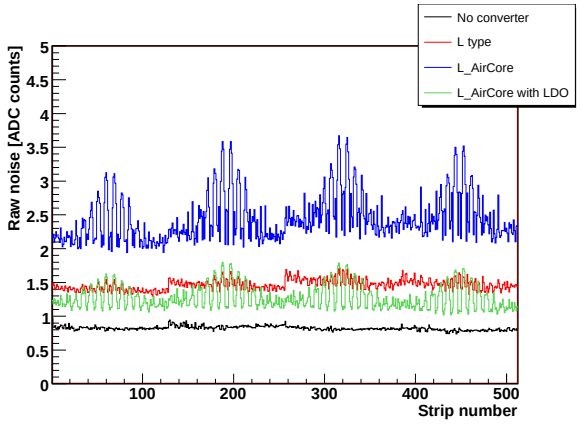

Figure 7.57: Noise of a hybrid on position 6.4. The hybrid was powered conventionally (black), by the standard L type PCB (red), by the L_AirCore PCB (blue) and by the L_AirCore PCB with LDO (green).

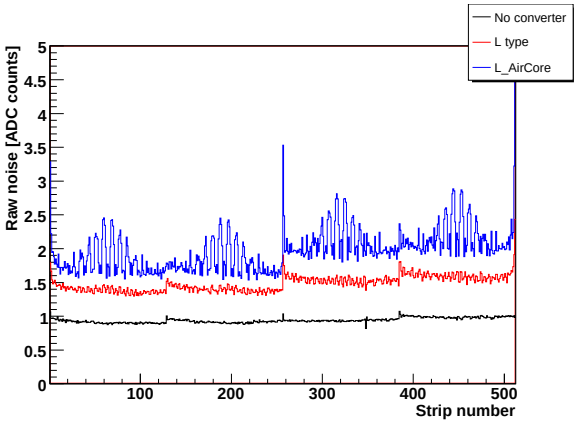

Figure 7.58: Noise of a hybrid with pitch adapter on position 6.4. The hybrid was powered conventionally (black), by the standard L type PCB (red) and by the L_AirCore PCB (blue)

7.3.2 Effect of the Converter Position

To determine which part of the modules are most sensitive with regard to radiative noise, another series of measurements with the L_AirCore PCB was performed. The converter board itself was powered but not electrically connected to the modules. It was placed on a plastic bar, mounted above the modules. This allowed to place the PCB at different well-defined positions (Fig. 7.59). Due to the bar the cover of the petal box was removed. However, this did not affect the modules' noise. The influence of the L_AirCore PCB is summarised in Fig. 7.60. The colour of the rectangles indicates the average noise level of module 6.4. The rectangle position represents the position of the converter. The cable used to power the converter had to be routed across the set-up. This raised the concern that the cable could radiate noise and affect the modules as well, but since measurements in which the converter was placed at high y positions and the cable crossed the largest part of the set-up show the lowest noise, close to the reference noise without converter, an eventual influence of the cable can be neglected.

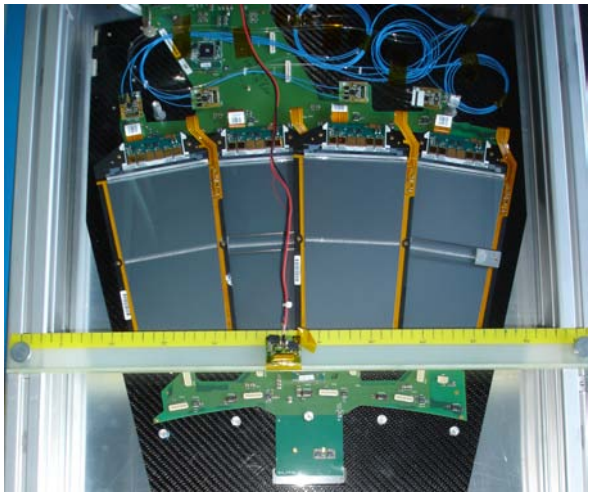

Figure 7.59: Photograph of the set-up to evaluate the influence of the converter's position.

Concluding from this, the most sensitive part of the module concerning radiation is the area containing the hybrid and the pitch adapter. The radiation is not picked up by the sensor. This is consistent with the measurement with the S type PCB, shown in Fig. 7.32. Furthermore it is plausible because electromagnetic radiation oscillating with 4 MHz, propagates with an extreme long wavelength of about 75 m, compared to the sensor length of several centimetres.

Since the radiated noise has no impact on a module without sensor, it seems likely that the radiated noise couples into the front-end electronics or the pitch adapter, but requires the capacitive coupling between the sensor strips to affect the module noise.

A theory which motivates both, the sensitivity of the front-end region as well as the anti-correlated wing noise, is shown in Fig. 7.61. The pitch adapter is connected to the sensor strips and thus AC-coupled to the sensor backplane. This creates loops which are closed by the 1.25 V reference of the preamplifiers. The fields of the converter inductors couple into the pitch adapter and induce alternating currents. The size of these currents depend linearly on the area of the loops. Per APV, each preamplifier contributes to 127 loops of different sizes. The flow direction of the induced current of a specific strip is different for loops to the "right" and to the "left" of the strips. Thus the currents in the outer strips are larger. The amount of the resulting currents depends linearly on the channel number. In a simple approach, the current I_i through preamplifier i can be calculated from the current I_0 of a single loop between two adjacent strips:

$$I_i = \left(\frac{(C-1)\,C}{2} - (i-1)C \right) I_0, \tag{7.3}$$

where $C = 128$ is the number of channels per APV.

Further studies are needed to test this theory and to understand how exactly the radiated noise couples into the modules.

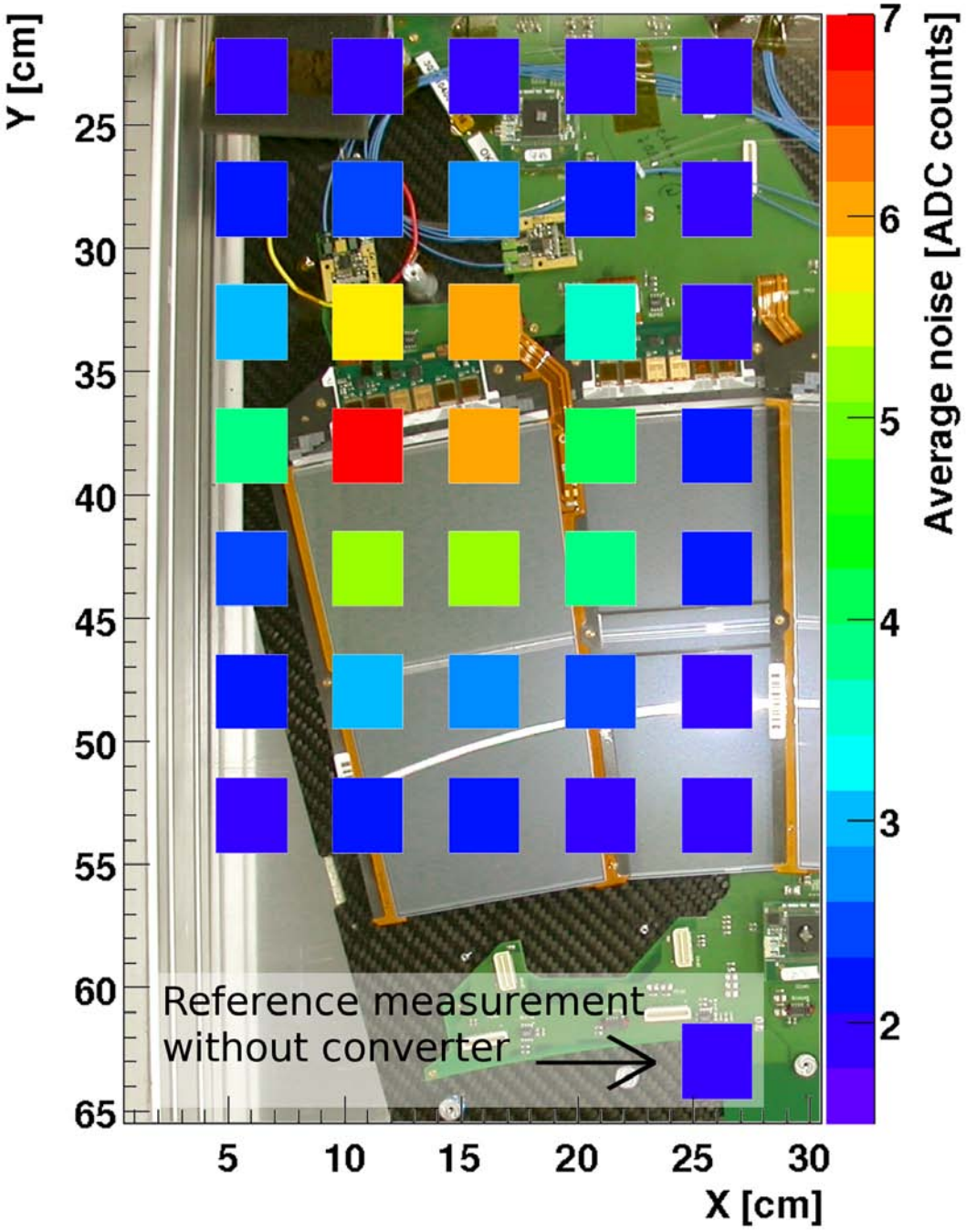

Figure 7.60: Average noise of module 6.4. The module is powered conventionally while a L_AirCore PCB is placed at different locations above it. The colour of the rectangles indicate the average noise level of module 6.4. The rectangle position represents the position of the converter. The photograph in the background has been adjusted to the scalings of the x- and y-axis.

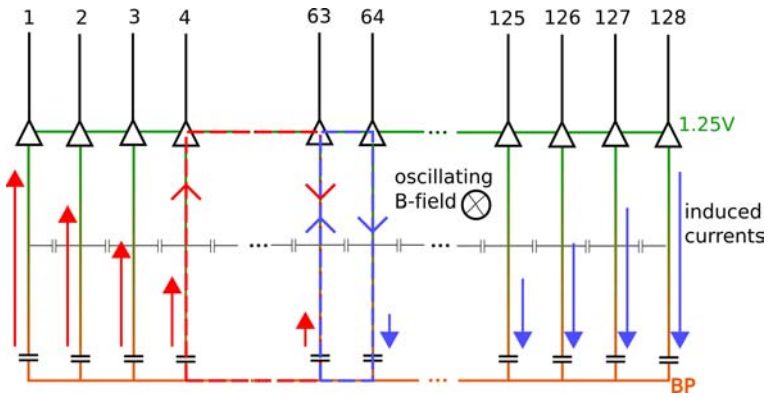

Figure 7.61: Sketch of the connection between the preamplifiers of an APV and the sensor strips. The preamplifiers are AC coupled to the back plane of the sensor. The arrows in red and blue represent the currents which are induced by an alternating field, in a fixed moment in time. The arrow length corresponds to the amount of current. Two loops to which strip 63 contributes are indicated. Note that the inner two arrows are not to scale.

7.3.3 Potential Countermeasures

Several potential countermeasures have been tested to reduce the amount of noise injected by the converters with air-core inductors.

Toroidal Inductors
The magnetic flux of toroids is more confined to the core than for solenoids. Hence it was hoped to reduce the electromagnetic fields emitted from the converter PCBs by replacing the solenoid inductors with toroidal ones. Two different toroids (shown in Fig. 7.62) have been fabricated and tested on the L_AirCore PCB. The first toroid is made of wire, which has been wound around a plastic core. For the second one a strip was used. The latter was supposed to improve the containment of the electromagnetic field. The characteristics of the toroidal inductors are summarised in Tab. 7.1. The noise of module 6.4 corresponding to measurements with the different inductors is shown in Fig. 7.63. The differences between the measurements with the solenoids and the strip toroids are rather small, but the wire toroids reduce the noise by a factor of about 3.

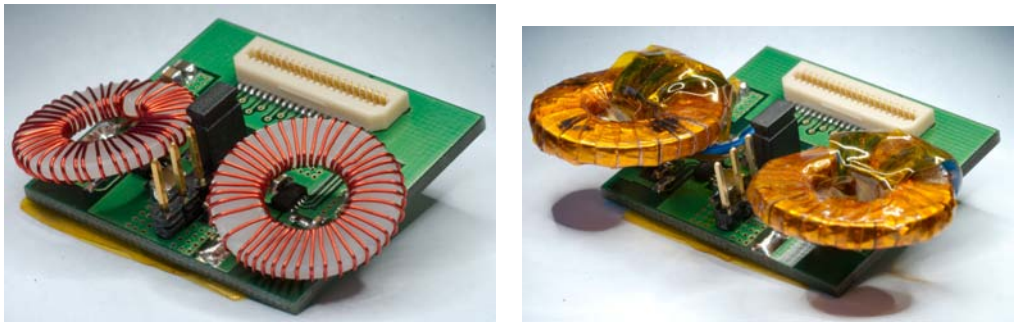

(a) PCB with wire toroids.

(b) PCB with strip toroids.

Figure 7.62: L_AirCore PCB with self-fabricated toroidal inductors.

	Wire toroid	Strip toroid
External diameter [mm]	17	20
Internal diameter [mm]	8.5	10
Height [mm]	1.75	2
Number of turns	43	35
Inductance [nH]	620	530
Ohmic Resistance [Ω]	0.3	0.3

Table 7.1: Parameters of the toroidal inductors used for this work.

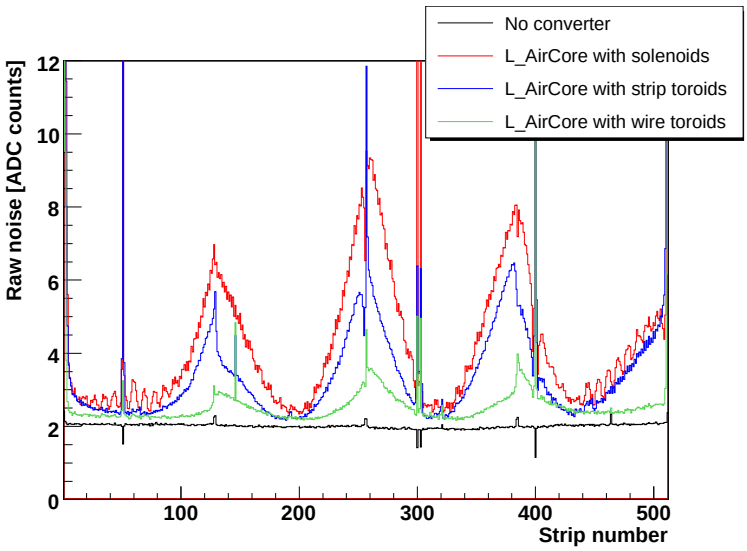

Figure 7.63: Noise of module 6.4. In black a reference run without converter is shown. In addition the module's noise is shown while it was powered by the L_AirCore PCB with solenoidal inductors (red), as well as strip (blue) and wire (green) toroids.

Shielding the Converters

Another possibility to cope with the emissions of an inductor is to shield [64] it with conductive materials like copper or aluminium. If the inductor is encased in such material its electromagnetic field induces eddy currents in the conductor. These currents induce an electromagnetic field which compensates the original one due to Lenz's law. In addition, the skin effect causes the currents to flow close to the surface of the shield. The depth in which the current density is reduced to $1/e$ of its original value depends on the frequency f and is referred to as the skin depth δ. This parameter is a good indicator for the screening attenuation of a material since it depends furthermore on the electric conductivity σ and the permeability $\mu = \mu_0\mu_r$ of the shield:

$$\delta = \sqrt{\frac{1}{\pi\mu\sigma f}}. \tag{7.4}$$

Assuming a frequency of 4 MHz, the skin depth of copper is 33 µm while the skin depth of aluminium equals about 42 µm. Besides the material, the screening attenuation depends furthermore on the geometry of the shield and on the distance between source and shield. Except for some elementary geometries, the screening attenuation cannot be calculated analytically. However some useful aspects are universally valid:

- The screening attenuation increases with the frequency.
- The screening attenuation increases with the distance between source and shield. This effect is less relevant for higher frequencies.
- The screening attenuation increases with the electrical conductivity and thickness of the shield.
- Frequencies in the order of MHz can be shielded with very thin layers.
- The influence of leaks on the screening attenuation is increased for higher frequencies.

To evaluate the effect of different shield materials and their thickness, a L_AirCore PCB, electrically not connected to the modules, was placed above the APVs of module 6.4 and shielded in several copper and aluminium boxes of different thicknesses. A set of boxes can be seen in Fig. 7.64. The corresponding noise of module 6.4 is shown in Fig. 7.65. According to this test the radiated noise can be shielded completely by less than 60 µm of aluminium. Is has to be noted that the used aluminium was more flexible than the copper. This likely explains the decreased performance of the 35µm copper shield since the aluminium feedthroughs were easier to implement. Also shown in Fig. 7.65 are several measurements in which the metal boxes were connected to an external ground potential. This had no significant effect on the noise.

Figure 7.64: Selection of boxes used to shield a detached L_AirCore PCB.

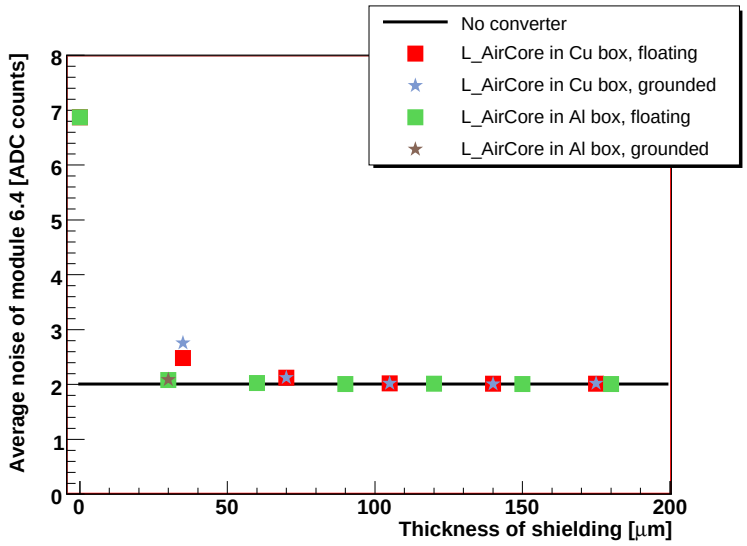

Figure 7.65: Noise of module 6.4 while irradiated by a L_AirCore PCB. The average noise is shown as a function of the shield thickness. The reference without converter is shown in black. The data shown in red and green correspond to a measurement with copper and aluminium boxes, respectively. The results shown in light blue and brown correspond to measurements with grounded copper and aluminium boxes, respectively.

To power module 6.4 with a shielded L_AirCore board, the converter PCB was encased in copper/aluminium with feedthroughs for the connection to the ICB, the module connector and to provide the converters with power. A photograph of a shielded PCB is shown in Fig. 7.66. The thickness of the shield was increased by adding more layers to it. The test was also performed with the L_AirCore with LDO. According to the results summarised in Fig. 7.67, a thin (30 µm) layer of aluminium reduces the noise of the module significantly. Increasing the shield thickness beyond 30 µm does not improve the noise performance. Hence it is possible that even a thinner shield would be sufficient. For the given thicknesses, a significant difference between the shielding efficiency of aluminium and copper was not observed.

Figure 7.66: Top and bottom sides of a L_AirCore PCB shielded with aluminium. The bottom side is isolated with Kapton tape.

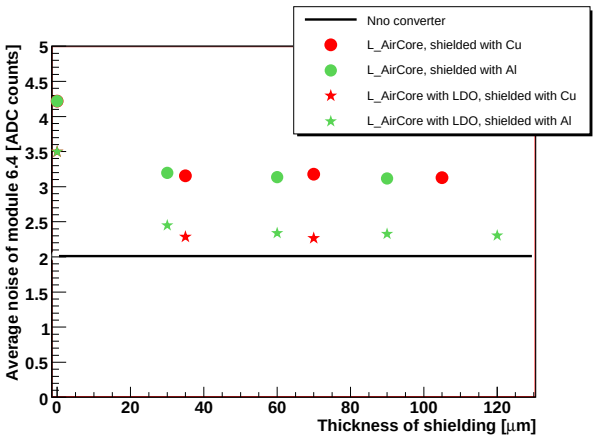

Figure 7.67: Noise of module 6.4. In black a reference run without converter is shown. The remaining data were recorded while the module was powered by the L_AirCore PCB or the L_AirCore PCB with LDO, indicated by cycles and stars, respectively. Data shown in red and green correspond to copper and aluminium, respectively.

To improve the shielding, the inductors have been dismantled, encased in aluminium and then reinstalled on the converter PCBs. This was intended to reduce the effect of the inductors on the converter PCB itself but did not succeed. According to Fig. 7.68 it is more efficient to shield the complete PCB. This is likely related to radiation emitted from the PCB.

A more successful attempt to reduce the effect of the converters on the module noise was based on the combination of the benefits obtained due to the LDO, the toroidal inductors and the shielding. Accordingly, an L_AirCore PCB with LDO has been equipped with wire toroids and shielded with 30 µm aluminium. This combination removes virtually all noise induced by the converters. Figure 7.69 shows no difference between the measurement with and without converter. Only the noise of the module edge channels is still slightly increased (Fig. 7.70) since the bias ring of this module was not coupled to the 1.25 V, as described in Sect. 7.2.2.

To get an impression of the additional material that would be needed for shielding, one can conservatively assume one 30 µm thick aluminium box of 3 cm×3 cm×1 cm per module. This would lead to 0.5 kg of additional aluminium per TEC or 2.2 kg for the complete strip tracker.

Increasing the Distance between the Converter and the Module

The measurements described in Sect. 7.3.1 show a strong dependence between the module's noise and the position of the converter. Hence it was tested how the module behaves if it is powered by the L_AirCore PCB from a greater distance. This is possible due to a PCB which has been modified into a L^S_AirCore board (Fig. 7.71(a)). Like the L^S PCB with internal inductors, this new board is connected to the ICB via the bridge plug of the S type PCB. In this constellation the air-core inductors are about 3 cm further away from the module. In addition, a long cable (40 cm in this case) can be added between the converter PCB and the plug, allowing to change the PCB's position. Figure 7.71(b) shows how the L^S_AirCore board is operated 7 cm away from the standard position of the L_AirCore board. The results of this test are summarised in Fig. 7.72. The majority of the noise is removed over the first two centimetres and due to the filtering function of the S bridge. If the converter PCB is placed 7 cm away from the module, its effect on

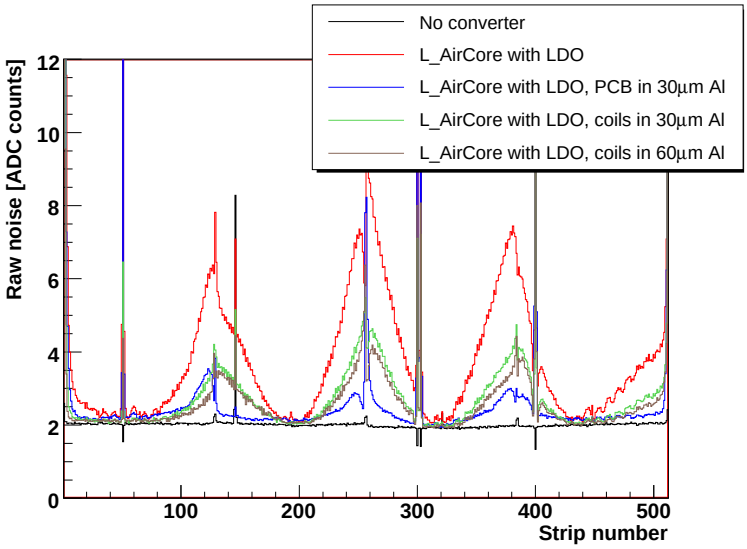

Figure 7.68: Noise of module 6.4. A measurement without converter is shown in black. The remaining data were recorded while the module was powered by a L_AirCore PCB with LDO. The complete PCB was shielded with 30 µm aluminium (red). The data plotted in green and brown corresponds to measurements in which only the solenoidal inductors were shielded with 30 µm 60 µm of aluminium, respectively.

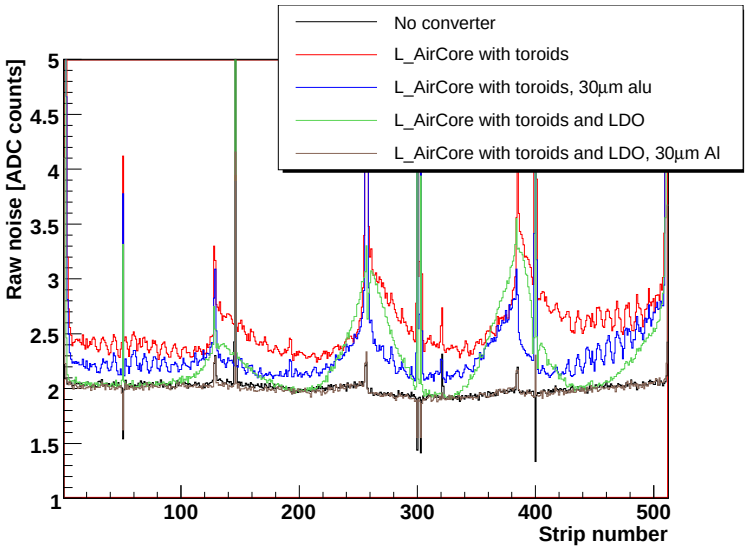

Figure 7.69: Noise of module 6.4. A reference run without converter is shown in black. During the runs plotted in red and blue, shielded and not shielded L_AirCore PCBs with toroidal inductors powered the module, respectively. Under the same conditions, the runs shown in green and brown were recorded, but the converter PCBs were additionally equipped with LDOs.

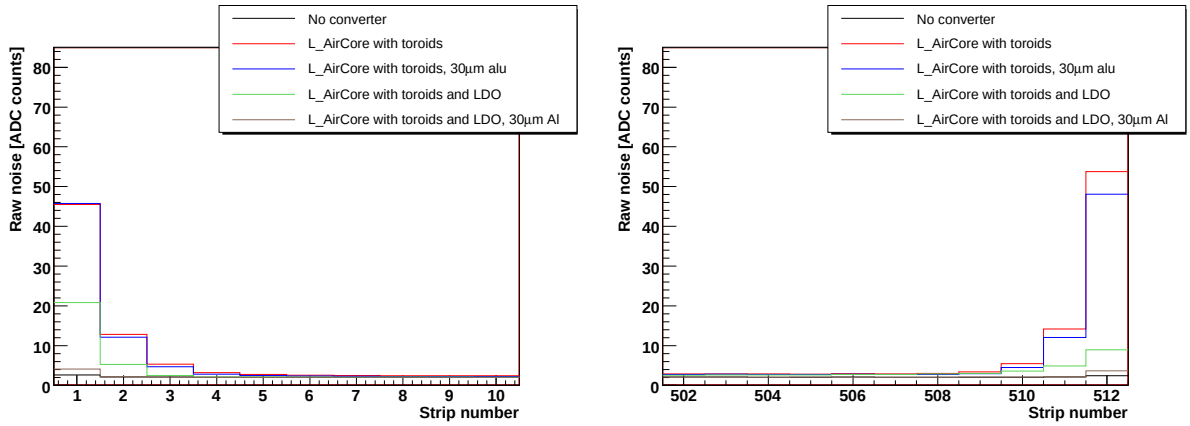

(a) First channel (1).

(b) Last channel (512).

Figure 7.70: Noise of the edge channels of module 6.4. A reference run without converter is shown in black. During the runs plotted in red and blue, shielded and not shielded L_AirCore PCBs with toroidal powered the module, respectively. Under the same conditions, the runs shown in green and brown were recorded respectively, but the converter PCBs were additionally equipped with LDOs.

the noise is almost completely abolished (Fig 7.73). Due to the cable plugged onto the converter and the connector bridge it was impossible to place the converter PCB at the exact same spot as if it was directly plugged onto the bridge. This explains the slight difference between the noise values measured at 3 cm.

(a) Directly connected to the ICB via a bridge connector.

(b) Connected via a cable, approximately 7 cm away from its standard position.

Figure 7.71: Photograph of the L^S_AirCore converter PCB powering module 6.4.

To ensure that the noise is only reduced due to the distance between the converter and the module and not due to the additional cable, the cable length was varied while the position of the converter PCB did not change. According to Fig. 7.74 the cable length has virtually no influence on the noise.

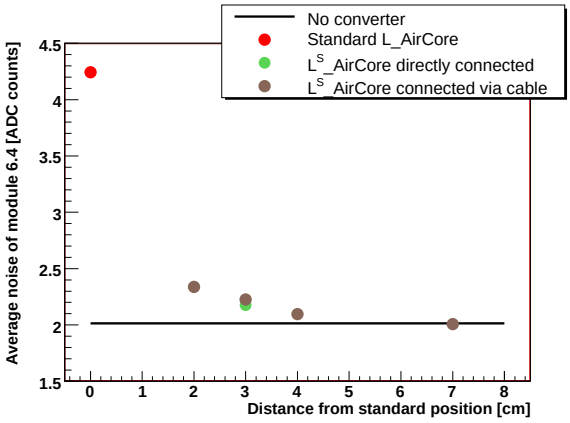

Figure 7.72: Average noise of module 6.4 as a function of the distance between converter PCB and module. The black line indicates the noise level without converters. The red point shows the noise measured with the L_AirCore PCB. The green and brown cycles represent measurements with the L^S_AirCore PCB powering the module directly connected to the ICB or via a cable, respectively.

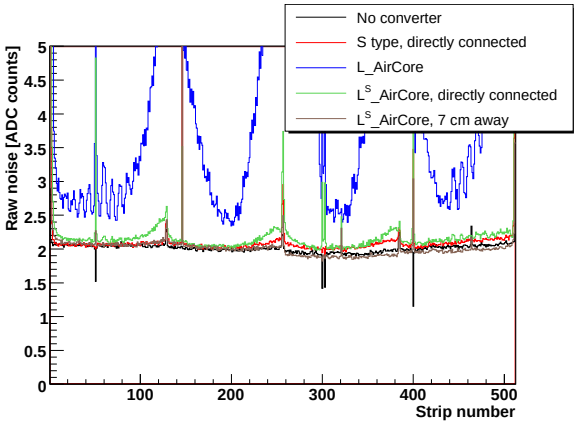

Figure 7.73: Noise of module 6.4. In black the noise without converter PCB is shown. In red, blue and green measurements with the S type, the L_AirCore and the L^S_AirCore PCB placed at their default position are shown, respectively. The data shown in brown correspond to a measurement in which the L^S_AirCore PCB was placed 7 cm away from the module.

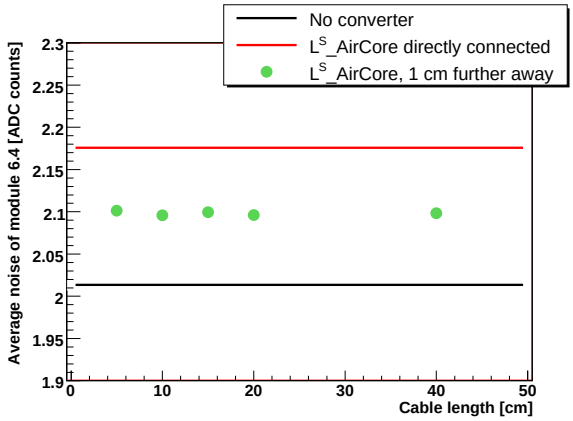

Figure 7.74: Average noise of module 6.4 as a function of the cable length between the converter PCB and the ICB for a fixed location of the converter PCB. The green points represent the measured noise with the L^S_AirCore PCB connected to the ICB via cables of different length. The black line indicates the noise level without converters. The red line shows the noise recorded while the L_AirCore PCB was directly connected to the ICB.

Chapter 8

Summary and Outlook

A front petal of the CMS tracker end caps, instrumented with four ring-6 modules, has been operated. To provide the modules with power, commercial DC-DC buck converters with internal and external ferrite-core inductors, as well as external air-core inductors have been used. The converters have been implemented via pluggable PCBs, supplied with 5.5 V. They provided the front-end electronics with 1.25 V and 2.5 V.

During measurements with ferrite-core inductors an increase of the module noise of about 10%-20% has been observed. It was possible to remove the additional noise by subtracting a common mode that was assumed to depend linearly on the channel number of the readout chip. However, it has to be noted that the latter is only possible for analogue readout.

Furthermore, the noise generated by the DC-DC converters with ferrite-core inductors could be suppressed either by the usage of a 50 mV low dropout regulator or by connecting the converter via a cable measuring several centimetres in length. Further studies are needed to understand and reproduce the latter using passive components.

It has been shown that converters with ferrite-core inductors cause only a slight increase of the crosstalk between the modules. So far this led to no increase of the noise.

A linear dependency of the module noise on the conversion ratio of the converters could be verified. For example, doubling the input voltage from 3.5 V to 7.0 V caused 10% more noise.

Powering the modules with DC-DC converters led to a drastic increase of the noise on the module edge strips. The capacitive coupling between the edge strips and the bias ring was identified as the reason for this noise. It was possible to reduce the edge noise drastically by coupling the bias ring to the reference voltage of the APV's pre-amplifiers (1.25 V).

Open channels, which had a low noise without converters, became noisy when the modules were powered with converters. This behaviour could be explained by the on-chip CM subtraction of the APV readout chip, which subtracts the CM per event from all channels. This leads to an overcompensation on the open strips.

On adjacent strips of neighbouring APVs an increased and anti-correlated noise has been observered. This phenomenon also occurred when the modules where powered conventionally, but it was amplified by the converters among the APVs in the centre of the module. A dedicated test was performed and confirmed a theory in which this effect is caused due to different reference voltages of the preamplifiers of two different APVs; even though the chips are mounted on the same hybrid.

Buck converters with air-core inductors led to an extreme increase of the module's noise. It could be shown that the majority of this noise is caused by the electromagnetic fields radiated by the air-core inductors. The hybrids of the modules could be identified as being most sensitive to this radiation. The effect of the radiated noise was only visible when the sensor strips were connected to the hybrid. The distribution of the observed noise reached its maximum on the channels at the APV borders and was superimposed by a periodic structure with a maximum in the centre of the chip. The origin of this periodic structure was identified to be of conductive nature. The radiated noise caused a correlation among the 64 channels of each half of an APV. At the same time the two opposite sides of the APVs became anti-correlated. The recorded measurements indicate that the radiated noise couples into the pitch adapter and requires the coupling to

the sensor backplane to affect the module. However, further studies are needed to test this theory and to understand how exactly the radiated noise couples into the modules.

To handle the radiated emissions of the air-core inductors several countermeasures have been tested. Improvements were achieved by replacing the solenoidal inductors with toroidal ones, by shielding the converter PCBs with aluminium/copper and by increasing the distance between the module and the converter PCBs. A noise level almost as good as without converter was achieved by placing a converter PCB with unshielded solenoidal inductors and a LDO approximately 7 cm away from the module. The distance should decrease for toroidal inductors. The usage of toroidal inductors on a converter PCB which was shielded with 30 μm aluminium and equipped with a LDO reduced the amount of noise down to the level of conventional powering. If the tested shielding would be applied for all converters of a TEC, it would add about 0.5 kg aluminium to the material budget of the TEC. Increasing the shield thickness further than 30 μm of aluminium did not provide additional benefits.

A conclusion which can be drawn from the performed measurements is that it is in principal possible to build a tracker system which copes with the noise caused by DC-DC converters. However it is not yet possible to predict if this will be worthwhile with regard to the material budget, since this depends on the conversion ratio and the efficiency, achievable with a radiation-hard converter. Furthermore it will be important to minimise the amount of required countermeasures to handle the converter noise. Open questions concerning the this issue are:

- Is it possible to suppress the conductive converter noise with passive components?
- How exactly and where precisely does the noise radiated by the inductors affect the modules?
- How can the noise susceptibility of the front-end electronics be reduced?

Future measurements could also aim at the optimisation of the presented countermeasures and their ideal combination. On a midterm scale this should lead to a converter-based powering concept that can be compared with the present system as well as with alternative schemes like serial powering. This process could also involve studies concerning the integration of different converter types, like the charge pump. An example would be a powering scheme based on two converter stages. The first stage could be implemented using buck converters while the second one, closer to the modules, could be inductorless charge pumps.

Last but not least it will be important to test radiation-hard custom converters when available and to provide feedback to the groups developing them.

Appendix A

PCB Layouts

A.1 The S Type PCB

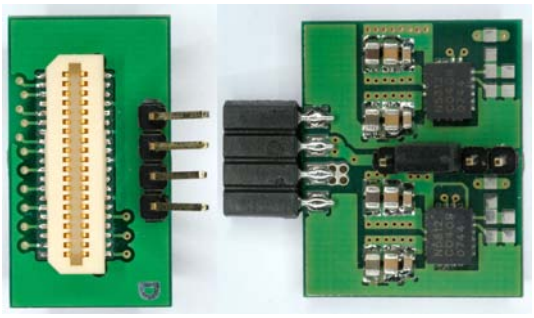

Figure A.1: Photograph of the S type PCB.

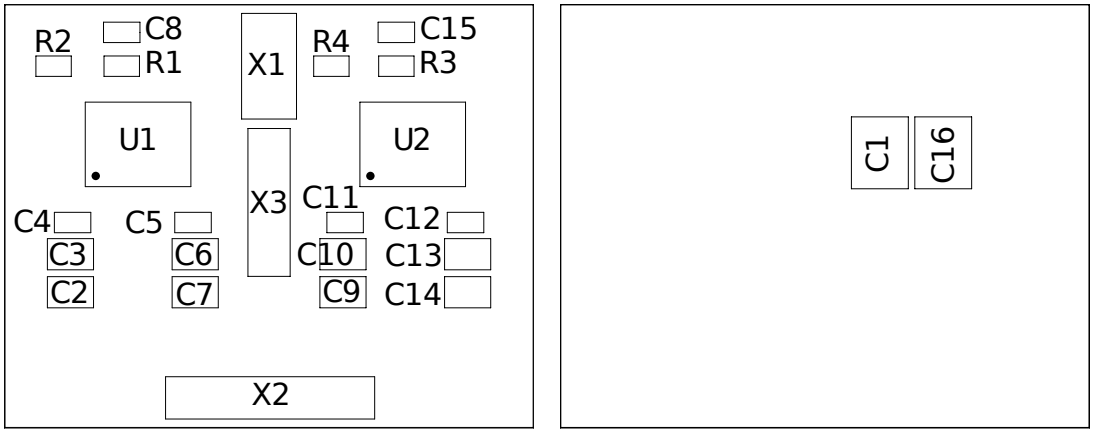

(a) Top.

(b) Bottom.

Figure A.2: Layout of the S type PCB.

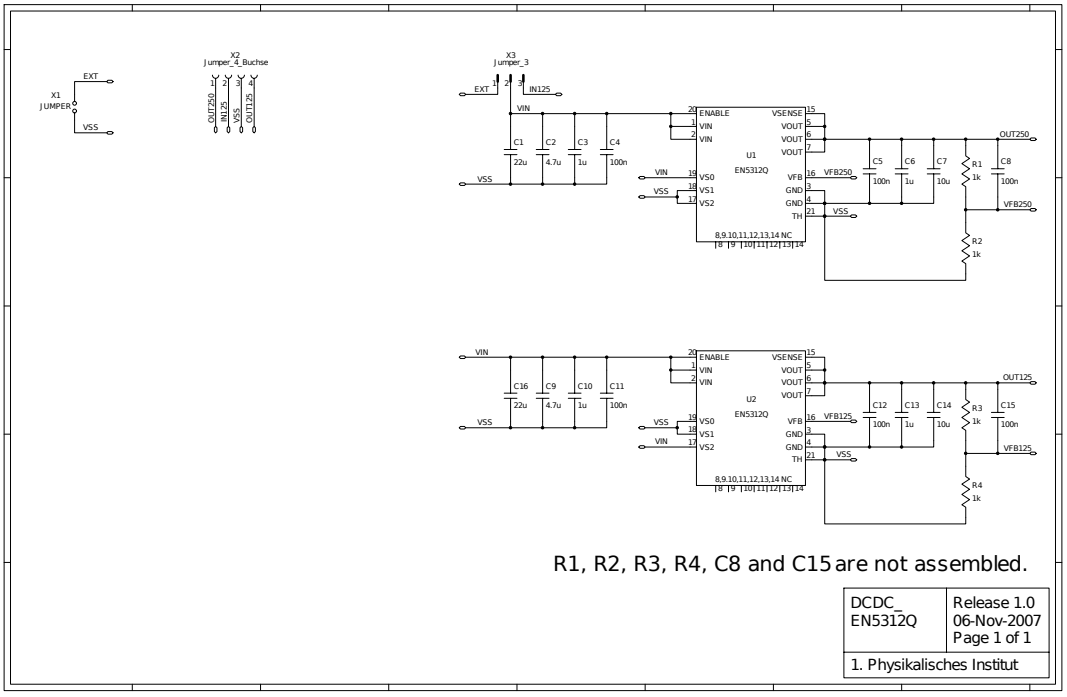

Figure A.3: Schematic of the S type PCB.

A.2 The L^S type PCB

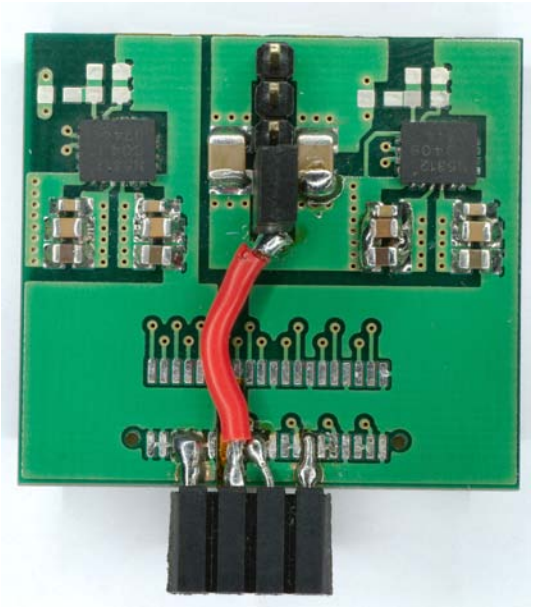

Figure A.4: Photograph of the L^S type PCB.

A.3 The L Type with LDO

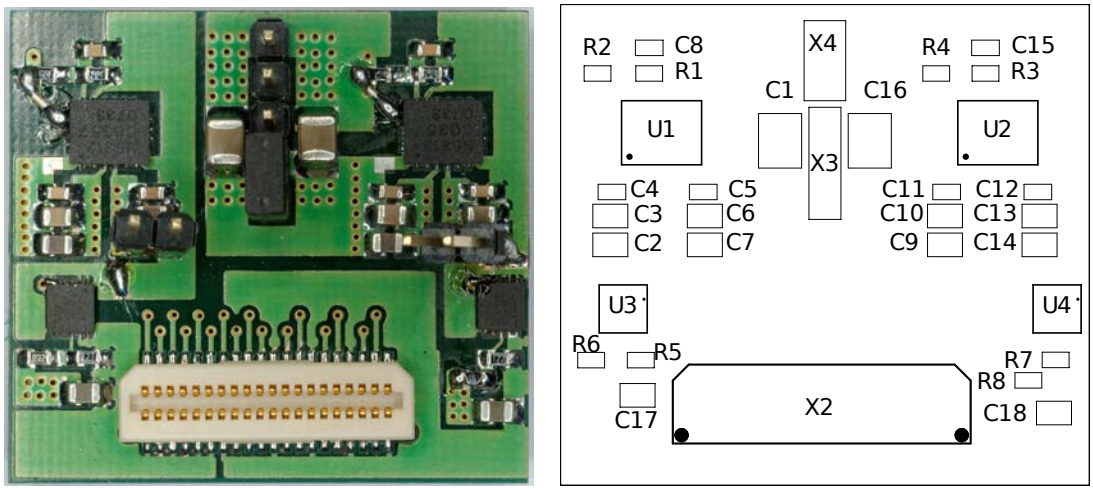

(a) Photograph. (b) Layout.

Figure A.5: The L type PCB with additional LDO.

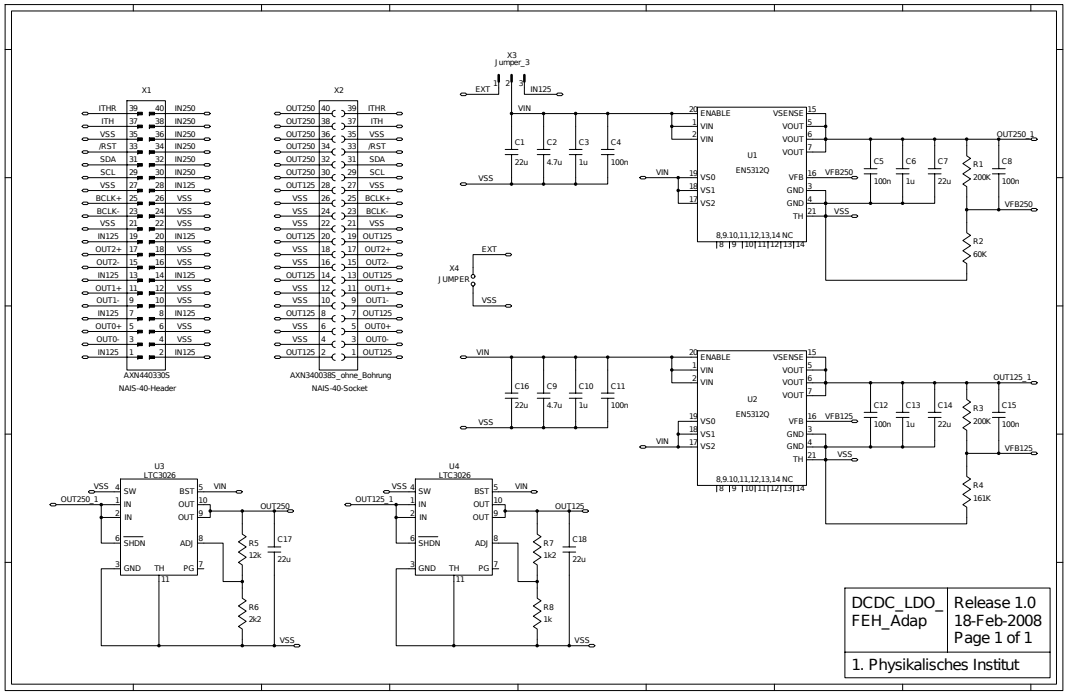

Figure A.6: Schematic of the L type PCB, additionally equipped with LDOs.

A.4 The MIC3385 PCB

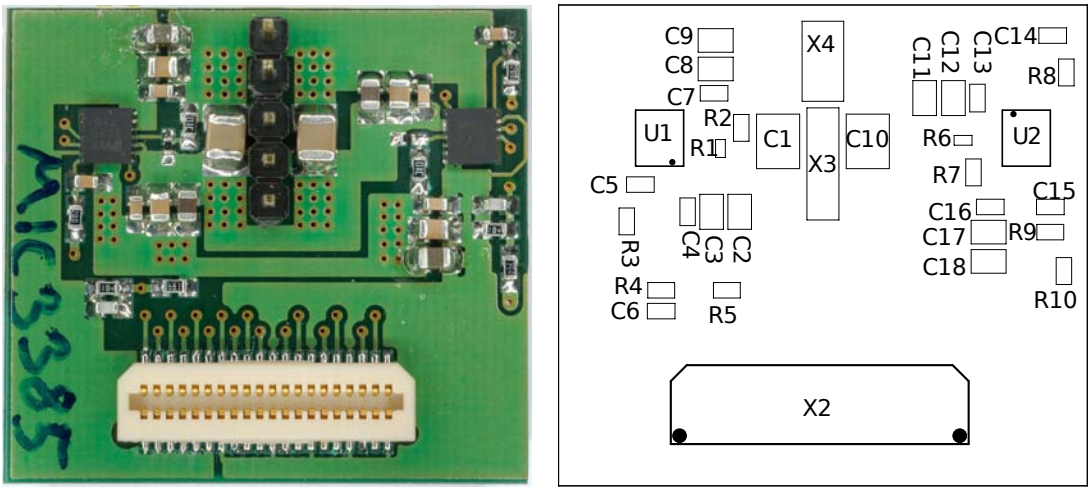

(a) Photograph. (b) Layout.

Figure A.7: The MIC3385 converter PCB.

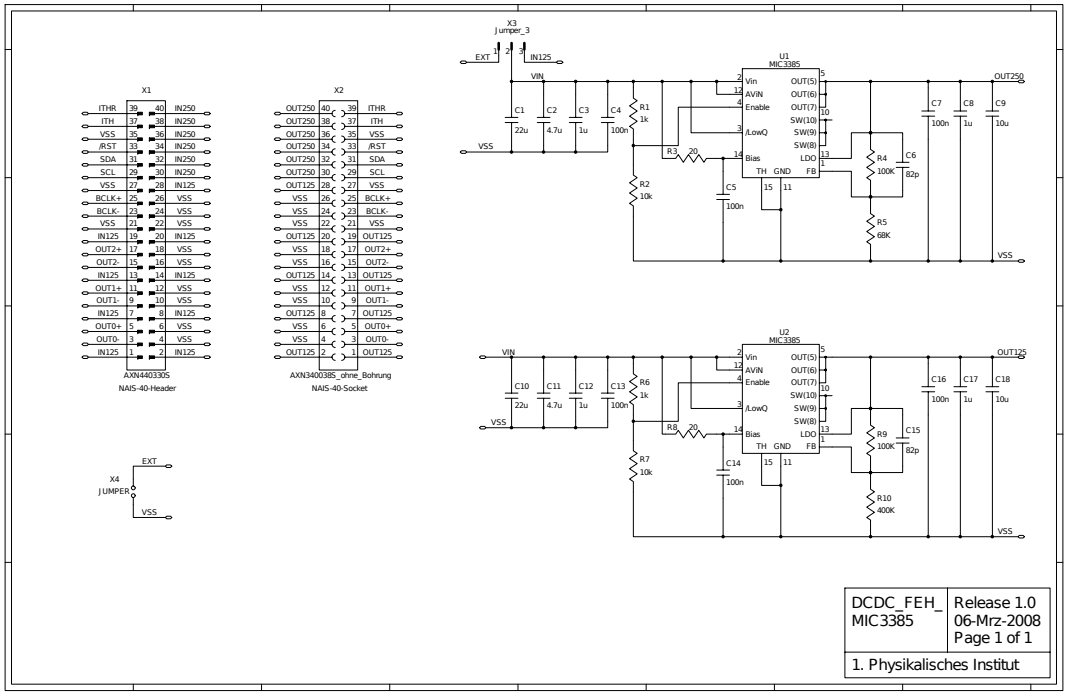

Figure A.8: Schematic of the MIC3385 PCB.

A.5 The L_AirCore PCB

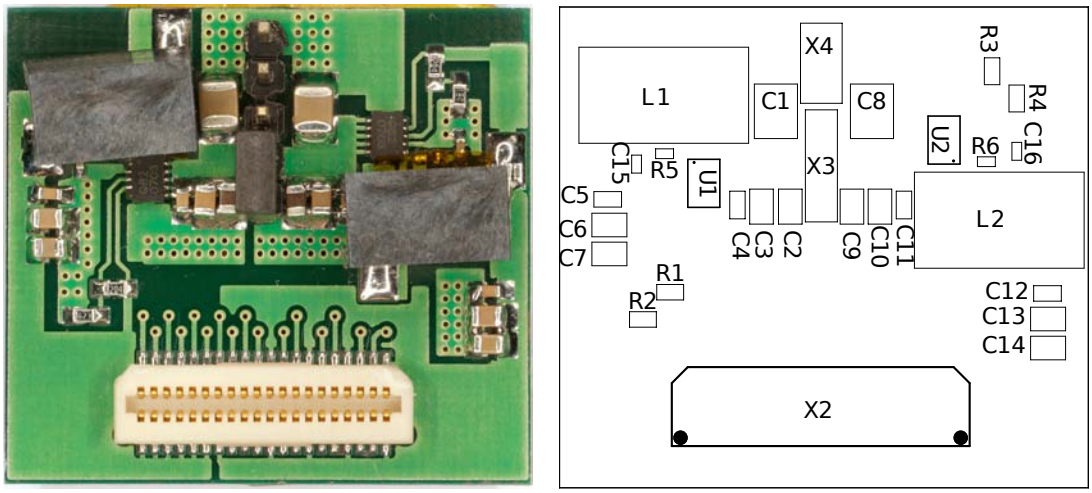

(a) Photograph. (b) Layout.

Figure A.9: The L_AirCore converter PCB.

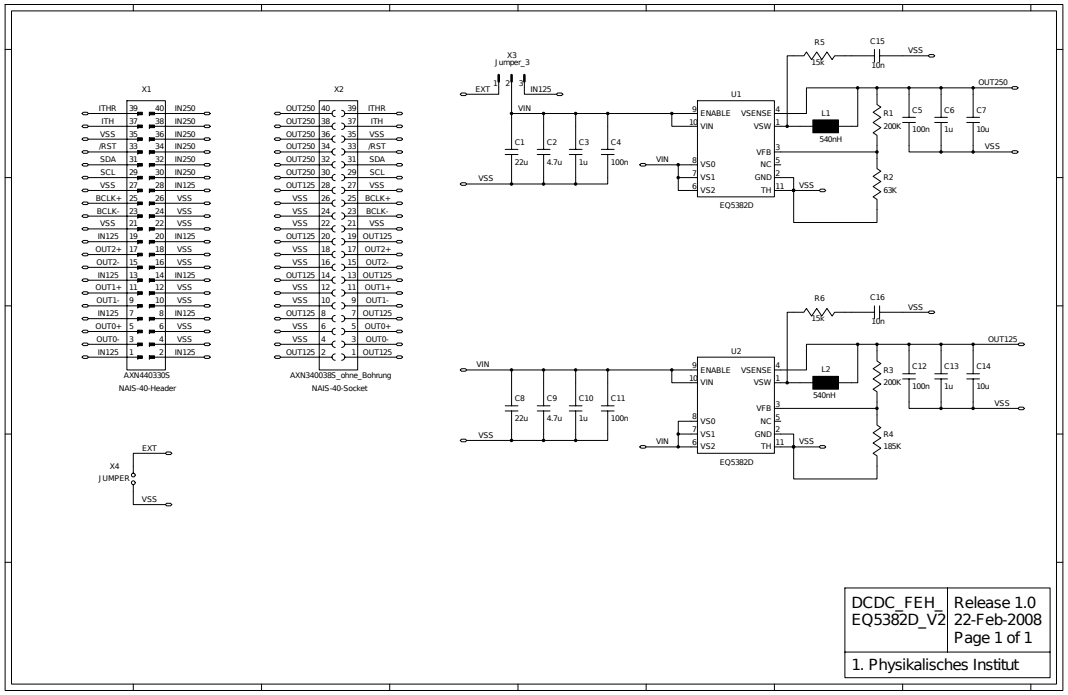

Figure A.10: Schematic of the L_AirCore PCB.

A.6 The L_AirCore with LDO

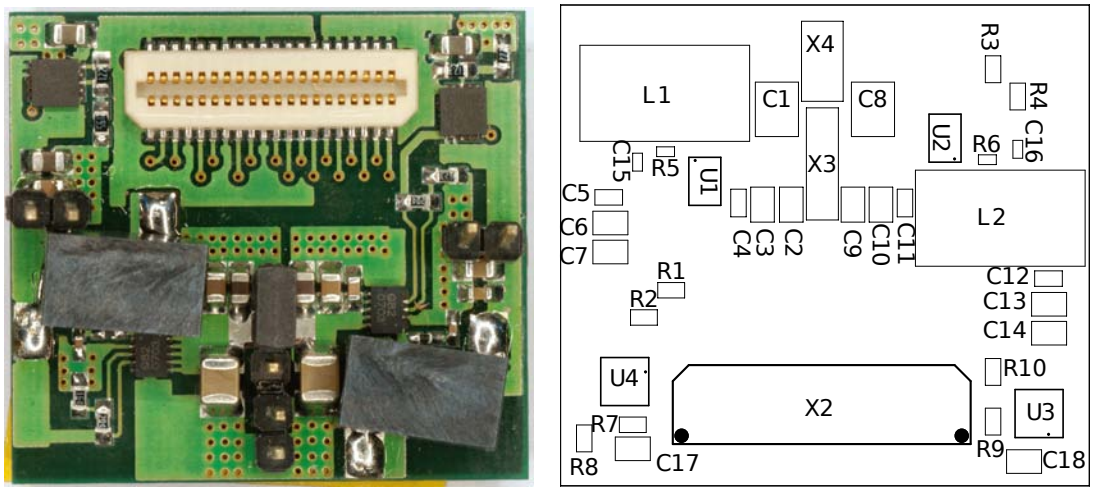

(a) Photograph. (b) Layout.

Figure A.11: The L_AirCore converter PCB with LDO.

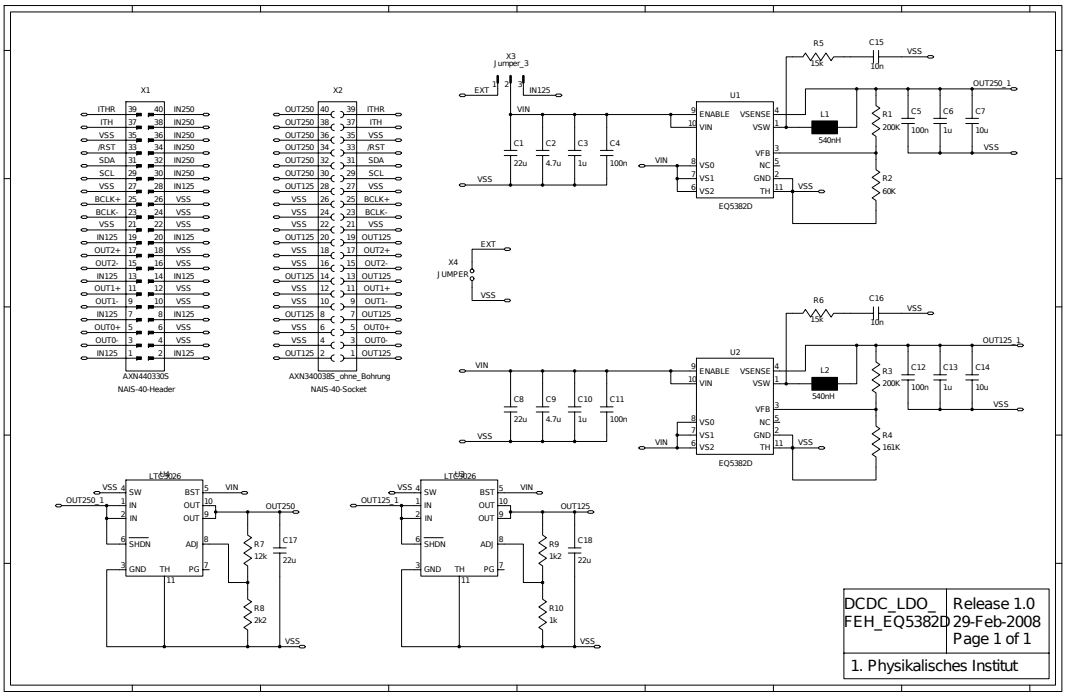

Figure A.12: Schematic of the L_AirCore converter PCB with LDO.

A.7 The L_FerriteCore PCB

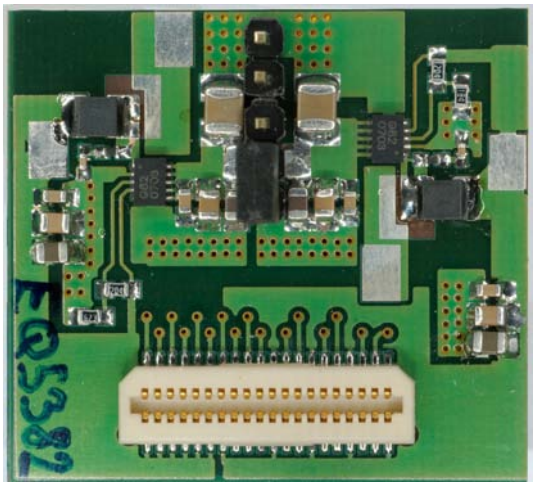

Figure A.13: The L_FerriteCore converter PCB.

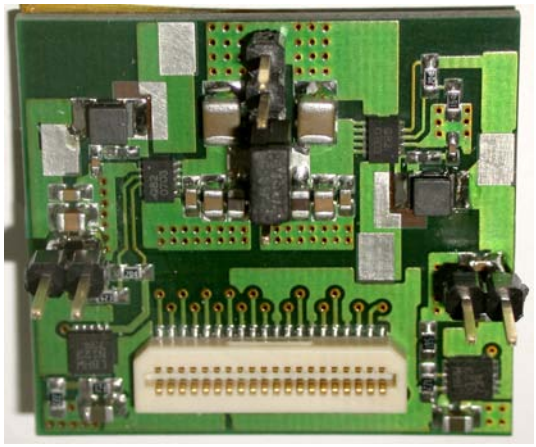

Figure A.14: The L_FerriteCore converter PCB with LDO.

Bibliography

[1] V. Frigo, *LHC map in 3D*, CERN Document Server (1997).

[2] C. Vanoli, *The CERN accelerator complex*, CERN Document Server (2006).

[3] The CMS Collaboration, S. Chatrchyan et al., *The CMS experiment at the CERN LHC*, JINST **3** S08004 (2008).

[4] D. Barney, *Transverse slice through CMS* (2004) http://cmsinfo.cern.ch/outreach/index.html.

[5] L. Borrello, A. Messineo, E. Focardi and A. Macchiolo, *Sensor Design for the CMS Silicon Strip Tracker*, CMS NOTE-2003/020 (2003).

[6] R. Brauer, *Integration of the End Cap TEC+ of the CMS Silicon Strip Tracker*, PhD thesis, RWTH Aachen University, CMS TS-2008/012 (2008).

[7] J. Troska et al., IEEE Trans. Nucl. Sci. **50** (2003) 1067.

[8] K. Gill et al., *Progress on the CMS Tracker Control System*, 11^{th} Workshop on Electronics for LHC and Future Experiments, Heidelberg, Germany (2005).

[9] C. Paillard, C. Ljuslin and A. Marchioro, *The CCU25: a network oriented communication and control unit integrated circuit in a 0.25 μm CMOS technology*, 8^{th} Workshop on Electronics for LHC Experiments, Colmar, France (2002) 174.

[10] Philips Semiconductors, *The I^2C-Bus Specification*, Version 2.1 (2000) Document order number: 9398 393 40011.

[11] P. Placidi et al.,*CMS Tracker PLL Reference Manual Version 2.1*, CERN - EP/MIC (2001).

[12] U. Goerlach, *Front-end hybrids for the CMS silicon tracker*, 8^{th} Workshop on Electronics for LHC Experiments, Strasbourg, France (2002) 170.

[13] G. Magazzù, A. Marchioro and P. Moreira, IEEE Trans. Nucl. Sci. **51** (2004) 1333.

[14] M. Raymond et al., *The CMS tracker APV25 0.25μm CMOS readout chip*, IEEE Nucl. Sci. Symposium and Medical Imaging Conference, Lyon, France (2000).

[15] L. Jones, *APV25-S1 User Guide, Version 2.2*, Rutherford Appleton Laboratory (2001).

[16] P. Murray, *APVMUX User Guide, Version 1.0* (2000).

[17] J. A. Coughlan et al., *The CMS Tracker Front-End Driver*, 9^{th} Workshop on Electronics for LHC Experiments, Amsterdam, Netherlands (2003).

[18] M. Friedl, *The CMS Silicon Strip Tracker and its Electronic Readout*, Austrian Academy of Sciences, available at http://cern.ch/friedl (2001).

[19] S. Gadomski et al., *The deconvolution method of fast pulse shaping at hadron colliders.*, NIM **A 320** (1992) 217.

[20] M. Raymond, *Module studies at IC, including on-chip CM subtraction explanation* (2001) http://icva.hep.ph.ic.ac.uk/∼dmray/pptfiles/CMStracker31_10_01.ppt.

[21] R. Brauer, K. Klein et al., *Design and Test Beam Performance of Substructures of the CMS Tracker End Caps*, CMS Note 2005/025 (2005).

[22] S. Paoletti et al., *The Powering Scheme of the CMS Silicon Strip Tracker*, 10^{th} Workshop on Electronics for LHC and Future Experiments, Boston, USA (2004) 194.

[23] S. Paoletti, *The Implementation of the power supply system of the CMS Silicon Strip Tracker*, Topical Workshop on Electronics for Particle Physics, Prague, Czech Republic (2007) 377.

[24] S. Paoletti, *Low Impedance Cable for LV & HV power sense for TOB & TEC*, CERN EP/CME, EDMS Id 734028 (2006).

[25] G. Lutz, *Semiconductor radiation detectors*, Springer, ISBN 3-540-64859-3 (1999).

[26] J. David, *Low-noise pre-amplifier* (1998) http://www.nikhef.nl/∼jds/vlsi/index.html.

[27] F. Gianotti, L. M. Mangano and T. Virdee, *Physics potential and experimental challenges of the LHC luminosity upgrade*, Eur. Phys. J. **C 39**, CERN-TH-2002-078 (2002) 293.

[28] T. Virdee, A. Ball and A. Petrilli, *CMS Expression of Interest in the SLHC*, CERN, Geneva, Switzerland, CERN-LHCC-2007-014 (2007).

[29] W. Scandale and F. Zimmermann, *Scenarios for sLHC and vLHC*, Nucl. Phys. **B 177-178** (2007) 207.

[30] J. Nash, *Overview of SLHC experiment upgrades*, SLHC-PP kick-off meeting, April (2008) http://indico.cern.ch/conferenceDisplay.py?confId=29254.

[31] P. Raimondi, D.N. Shatilov and M. Zobov, *Beam-Beam Issues for Colliding Schemes with Large Piwinski Angle and Crabbed Waist*, Naz. Lab., Frascati, Italy, LNF-07-003-(IR) (2007).

[32] J.P Koutchouk and G. Sterbini, *An Early Beam Separation Scheme for the LHC Luminosity Upgrade*, 10^{th} European Particle Accelerator Conference, Edinburgh, UK, LHC-PROJECT-Report-972 (2006) 2134.

[33] R. Ranieri, *The Simulation of the CMS Silicon Tracker*, Nuclear Science Symposium and Medical Imaging Conference, Honolulu, USA, CMS CR 2008/007 (2007).

[34] U. Schlienz, *Schaltnetzteile und ihre Peripherie*, Vieweg, ISBN 978-3-8348-0239-2 (2007).

[35] U. Tietze and Ch. Schenk, *Halbleiter-Schaltungstechnik*, Springer, ISBN 3-540-42849-6 (2002).

[36] Maxim Integrated Products, *Input and Output Noise in Buck Converters Explained*, Application Note 986, Sunnyvale, CA, USA (2002) http://www.maxim-ic.com/appnotes.cfm/an_pk/986.

[37] G. Darbo, Ph. Farthouat and A. Grillo, *Readout architecture of the ATLAS upgraded tracker*, TWEPP 2008, Naxos, Greece (2008).

[38] Enpirion, *EN5312QI - 1A Synchronous Buck Regulator With Integrated Inductor*, Bridgewater, NJ, USA (2007) http://www.enpirion.com/pdfdocuments/EN5312Q%20Rev%2011.pdf.

[39] Enpirion, *EQ5382D - Voltage Mode Synchronous Buck PWM DC-DC Converter*, Bridgewater, NJ, USA (2006).

[40] Micrel Inc.,*MIC3385: 8 MHz Inductorless Buck Regulator with LDO Standbye Mode*, San Jose, CA, USA (2008) http://www.micrel.com/page.do?page=/product-info/products/mic3385.jsp.

[41] muRata, *Chip Coils for Choke Wire Wound Type - LQH32C_23/LQH32C_33 Series (1210 Size)*, Nagaokakyo-shi, Kyoto, Japan (2007) http://www.murata.com/catalog/o05e.pdf.

[42] Coilcraft, *Maxi Spring^{TM} Air Core Inductors*, Cary, Illonis, USA (2007) http://www.coilcraft.com/pdfs/maxi.pdf.

[43] R. Ely and M. Garcia-Sciveres, *DC to DC Power Conversion*, 12^{th} Workshop on Electronics For LHC and Future Experiments, Valencia, Spain (2007) 89.

[44] M. Weber, M. Lammentausta and G. Villani, *Serial Powering for Silicon Strip Detectors at SLHC*, 11^{th} Workshop on Electronics for LHC and Future Experiments, Heidelberg, Germany (2005) 214.

[45] D. B. Ta et al., *Serial powering: Proof of principle demonstration of a scheme for the operation of large pixel detector at the LHC*, Nucl. Instrum. Methods Phys. **A557** (2006) 445.

[46] Peter Huber, Kältemaschinenbau GmbH, Offenburg, Germany, http://www.huber-online.com.

[47] iseg Spezialelektronik GmbH, Radeberg/Rossendorf, Germany.

[48] Robert Bosch GmBH, *Controller Area Network CAN*, Gerlingen-Schillerhöhe, Germany, http://www.can.bosch.com.

[49] Institut de Physique Nucl'aire de Lyon, *CMS Trigger Sequencer Card User Manual Version 4.0*, http://lyoinfo.in2p3.fr/cms/cmstraces/tscweb/tsc.html http://lyoinfo.in2p3.fr/cms/cmstraces/tscweb/doc/tsc04.pdf.

[50] Kvaser AB, *The Kvaser PCIcan series of CAN bus controller cards*, Mölndal, Sweden (2004) http://www.kvaser.com/global/pdfdocs/products/pcican.pdf.

[51] W. Karpinski, private communication.

[52] Agilent Technologies, *Agilent E363xA Series, Programmable DC Power Supplies*, Santa Clara, CA, USA (2007) http://www.alliedelec.com/Images/Products/Datasheets/BM/AGILENT_TECH_TEST/835-0061.PDF.

[53] L. Mirabito, *Tracker Data Acquisition user guide* (2003) http://cmsdoc.cern.ch/cms/cmt/System_aspects/Daq/tkdaq.pdf.

[54] V. Brigljevic et al.,*Using XDAQ in Application Scenarios of the CMS Experiment*, CMS CR 2003/007, CERN, Geneva, Switzerland (2003).

[55] R. Arcidiacono et al., *HyperDAQ – Where Data Acquisition Meets the Web*, 10^{th} Int. Conf. on Accelerator and Large Expt. Physics Control Systems, Geneva, Switzerland (2005).

[56] R. Bruns et al.,*ROOT – An Object-Oriented Data Analysis Framework*, http://root.cern.ch.

[57] C. Civinini, *Studies on Noisy Strips*, INFN Firence (2003) http://hep.fi.infn.it/CMS/moduletest/tkwgen03/carlo.pdf.

[58] M. Raymond, private communication.

[59] U. Goerlach and J. D. Berst, *Description of the FE hybrids: up-dated document for the EDR* (2000). https://edms.cern.ch/file/113156/1.1/fe_hybrid_1.1.ps.

[60] M. Raymond, *Analog chain of the APV*, http://www.hep.ph.ic.ac.uk/∼dmray/pdffiles/APV_analog_chain_1.pdf, http://www.hep.ph.ic.ac.uk/∼dmray/pdffiles/APV_analog_chain_2.pdf.

[61] Linear Technology Corporation, *LTC3026 - 1.5A Low Input Voltage VLDO Linear Regulator*, Milpitas, CA, USA (2005) http://www.datasheetcatalog.org/datasheets2/20/206649_1.pdf.

[62] M. Raymond, *APV25 Power supply ripple sensitivity measurements* (2000) http://icva.hep.ph.ic.ac.uk/∼dmray/pdffiles/APV25psusens.pdf.

[63] F. Arteche and C. Rivetta, *EMC Diagnosis and Corrective Actions for Silicon Strip Tracker Detectors*, SLAC-PUB-11886, 7^{th} EMC Europe International Symposium on Electromagnetic Compatibility, Barcelona, Spain (2006).

[64] H. A. Wolfsperger, *Elektromagnetische Schirmung - Theorie und Praxisbeispiele*, Springer (2008).

Acknowledgement

I would like to express my sincere appreciation to my supervisor Prof. Dr. Lutz Feld for giving me the opportunity to write my diploma thesis as a part of an international experiment such as CMS. Right from the beginning he gave me the impression of being a full-fledged member of his team. I am very grateful to him for his guidance and support. His ideas and suggestions were an immense benefit for my work.

I thank Prof. Dr. Achim Stahl for giving the second expertise on this thesis.

I also want to thank Katja Klein for carfully proof-reading two complete versions of my thesis. Moreover, she explained to me the details of the CMS tracking system and was always a reliable source of honest advice. Her caring support throughout my work is invaluable.

For introducing me into his analysis software and teaching me the basics of C++ programing, I am indebted to Richard Brauer. I deeply appreciate that he always took the time to answer my questions. Best wishes go to him and his young family.

I thank all the members of our mechanics and electronics workshops, supervised by Waclaw Karpinski, Michael Wlochal and Gert Kirchhoff. Without the help and the converter PCBs designed by Waclaw Karpinski and Irfan Özem my studies would have been impossible.

I would also like to express my gratitude to Marc Raymond, who supported me with his knowledge about the APV.

It is fun to share an office with Katja Klein, Rüdiger Jussen and Jennifer Merz. I would like to thank them for establishing a pleasant and productive work environment. Moreover, I would like to thank Rüdiger for assembling the toroidal inductors and for his great photographs of the converter PCBs. Jennifer has started to become an expert on simulation software and could already provide some useful tips.

Thanks also to the other members of our working group. Demetrios Pandoulas, Martin Weber, Niklas Mohr, Daniel Sprenger, Matthias Edelhoff, Albert Bursche and Klaus Roth are great colleagues. Among other things, they provided me with constructive feedback during our working group meetings. I'm looking forward to rejoin the after-work soccer matches with Niklas and Klaus. I would be glad to help Daniel and Matthias to develop the next version of their "Hadronisation" game.

Last but not least I would like to thank my parents, friends and neighbours for their support and understanding throughout my studies. To appreaciate all their great and little deeds would go way beyond the present scope.

Erklärung

Hiermit erkläre ich, dass ich die vorliegende Diplomarbeit selbständig erarbeitet und ausschließlich die aufgeführten Referenzen verwendet habe. Alle Quellen und Zitate sind als solche kenntlich gemacht, und die Literaturangaben sind nach meinem besten Wissen und Gewissen korrekt und vollständig wiedergegeben.

Aachen, den 24.10 2008